Doctoral Dissertation

Fermi Surface Instability in $CeRh_2Si_2$ and CeNi Under Pressure

SHINGO ARAKI

Department of Physics, Graduate School of Science
Osaka University

January, 2001

Doctoral Dissertation

Fermi Surface Instability in $CeRh_2Si_2$ and CeNi Under Pressure

SHINGO ARAKI

Department of Physics, Graduate School of Science
Osaka University

January, 2001

Abstract

In antiferromagnetic cerium compounds, applying pressure causes a change of the electronic state from the antiferromagnetic ground state to a non-magnetic one. We have done the de Haas-van Alphen (dHvA) experiment under pressure to clarify the change of the Fermi surface properties such as the topology of the Fermi surface and the cyclotron effective mass. $CeRh_2Si_2$ is a usual $4f$-localized compound with a Néel temperature $T_N = 36$ K, while CeNi is a non-magnetic valence fluctuation compound. We succeeded in growing high-quality single crystals of $CeRh_2Si_2$ and CeNi.

In $CeRh_2Si_2$, we confirmed the pressure-induced superconductivity below about 0.38 K under 1.1 GPa, which had been reported for the polycrystal sample. We also measured dHvA oscillation at ambient pressure and under pressure. Some dHvA branches observed at ambient pressure are explained by the $4f$-localized electron model. The cyclotron effective mass is not large, ranging from 0.26 to $6.6m_0$. The dHvA frequency is found to be approximately unchanged up to $p_c \simeq 1.0$–1.1 GPa. Here, p_c corresponds to the quantum critical pressure where T_N becomes zero at $p \rightarrow p_c$. This means that the topology of the Fermi surface is unchanged. On the other hand, the cyclotron mass increases linearly with increasing pressure. Interesting is that the cyclotron mass of a main branch increases steeply above 0.9 GPa, reaching about $18m_0$. All the dHvA branches, which were observed below p_c, disappear above p_c and a new dHvA branch with a large mass of 22–$24m_0$ appears. This branch corresponds to an orbit of the band 25-hole Fermi surface in the $4f$-itinerant band model. This is the first dHvA experiment showing a change of the $4f$-electronic state from localized to itinerant, namely indicating a drastic change of the Fermi surface and cyclotron mass under pressure.

In CeNi, we measured dHvA oscillation at ambient pressure and under pressure. The topology of the Fermi surface at ambient pressure is explained by the $4f$-itinerant electron model. The cyclotron effective mass is relatively large, ranging from 3.0 to $27m_0$. We confirmed the first-order phase transition at $p_c \simeq 0.2$–0.4 GPa from the dHvA effect and specific heat experiments. The dHvA frequency is unchanged at the transition, indicating that the topology of the Fermi surface is unchanged. The cyclotron mass of some dHvA branches is reduced about quarter. Correspondingly, the specific heat coefficient $\gamma = 56$ mJ/K^2·mol at ambient pressure decreases steeply below 0.4 GPa, reaching 32 mJ/K^2·mol at 0.7 GPa. These results indicate an instability of the intermediate valence state with a critical pressure of 0.2–0.4 GPa.

Contents

1 Introduction

Magnetism in the rare earth compounds is based on the localized $4f$ electrons. The Ruderman-Kittel-Kasuya-Yosida (RKKY) interaction,[1-3] characterized by the temperature T_{RKKY}, causes a long-range magnetic order of $4f$ local moments, where the indirect f-f interaction is mediated by the conduction electrons with spins. On the other hand, the Kondo effect,[4] characterized by the temperature T_{K}, quenches the magnetic moments of the localized $4f$ electrons by the spin polarization of the conduction electrons. In the cerium compounds, both the RKKY interaction and the Kondo effect compete with each other.[5,6] In the non-magnetic Kondo-lattice ground state system, such as $CeCu_6$, an electronic specific heat coefficient γ becomes extremely large: $\gamma = 1600$ mJ/K^2·mol,[7] reflecting a large density of states at E_{F}. This γ value is by two to three orders of magnitude larger than those in usual s and p electron systems. This f electron system is called heavy fermions. In heavy fermion non-magnetic compounds, the $4f$ electrons are regarded as itinerant electrons.

Contrary to $CeCu_6$, most of the rare earth compounds, including the cerium compound, orders antiferromagnetically because the RKKY interaction overcomes the Kondo effect. An antiferromagnetic ground state is, however, altered with tuning the control parameter, such as pressure. In cerium antiferromagnetic compounds, applying pressure causes a change of the electron state from the antiferromagnetic ground state to a non-magnetic one. Around the quantum critical point, which corresponds to $T_{\mathrm{N}} \rightarrow 0$ at a critical pressure p_{c}, pressure induced superconductivity or non-Fermi liquid behavior are observed. These phenomena are one of the most important issues in the condensed matter physics.

To clarify the electronic state in the cerium compounds, we have done a de Haas-van Alphen (dHvA) measurement for $CeRh_2Si_2$ and CeNi under high pressure. The dHvA measurement is a very powerful method to determine the topology of the Fermi surface, the cyclotron effective mass and the scattering lifetime of the conduction electron. In this study, we grew high-quality single crystals of $CeRh_2Si_2$ and CeNi. The former compound $CeRh_2Si_2$ orders antiferromagnetically at 36 K. This compound is a usual $4f$-localized one. The latter compound CeNi is regarded as a non-magnetic heavy fermion compound, which was once called an intermediate valence compound or a valence fluctuation compound. The dHvA experiments at ambient pressure and under high pressure were done for both compounds. The electronic states of both compounds are found to be changed drastically under pressure.

In Chap. 2, we will give a review including more detail background of this study and the characteristic properties of the present compounds of $CeRh_2Si_2$ and CeNi. Next, we

will present the single crystal growth and experimental method in Chap. 3. In Chap. 4, we will give the experimental results and discuss the ground state property. Finally, we will summarize and conclude the present study in Chap. 5.

2 Review

2.1 General property of the f electron systems

2.1.1 RKKY interaction

The $4f$ electrons in the Ce atom are pushed into the interior of the closed $5s$ and $5p$ shells because of the strong centrifugal potential $l\,(l+1)/r^2$, where $l = 3$ holds for the f electrons. This is a reason why the $4f$ electrons possess an atomic-like character in the crystal.[8] On the other hand, the tail of their wave function spreads to the outside of the closed $5s$ and $5p$ shells, which is highly influenced by the potential energy, the relativistic effect and the distance between the Ce atoms. This results in the hybridization of the $4f$ electrons with the conduction electrons. These cause various phenomena such as valence fluctuations, Kondo lattice, heavy fermion, Kondo insulator and unconventional superconductivity.

The Coulomb repulsive force of the $4f$ electron at the same atomic site, U, is so strong, e.g., $U \simeq 5$ eV in the Ce compounds (see Fig. 2.1), that occupancy of a same site by two $4f$ electrons is usually prohibited. In the Ce compounds the tail of the $4f$

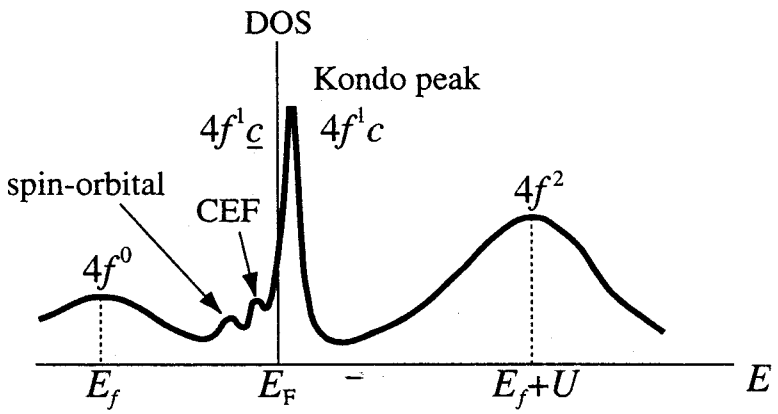

Fig. 2.1 Density of states (DOS) of the $4f$ electron in the Ce compound (Ce^{3+}).

partial density of states extends to the Fermi level even at room temperature, and thus the $4f$ level approaches the Fermi level in energy and the $4f$ electrons hybridize strongly with the conduction electrons. This $4f$-hybridization coupling constant is denoted by V_{cf}. When U is strong and V_{cf} is ignored, the freedom of the charge in the $4f$ electron is suppressed, while the freedom of the spin is retained, representing the $4f$-localized state. Naturally, the degree of localization depends on the level of the $4f$ electrons E_f,

where larger E_f helps to increase the localization. This situation is applied to most of the lanthanide compounds in which Ruderman-Kittel-Kasuya-Yosida (RKKY) interaction[1–3] play a predominant role in magnetism. The mutual magnetic interaction between the $4f$ electrons occupying different atomic sites cannot be of a direct type such as $3d$ metal magnetism, but should be indirect one, which occurs only through the conduction electrons.

In the RKKY interaction, a localized spin S_i interacts with a conduction electron with spin s, which leads to a spin polarization of the conduction electron. This polarization interacts with another spin S_j localized on an ion j and therefore creates an indirect interaction between the spins S_i and S_j. This indirect interaction extends to the far distance and damps with a sinusoidal $2k_F$ oscillation, where k_F is half of the caliper dimension of the Fermi surface. When the number of $4f$ electrons increases in such a way that the lanthanide element changes from Ce to Gd or reversely from Yb to Gd in the compound, the magnetic moment becomes larger and the RKKY interaction stronger, leading to the magnetic order. The ordering temperature roughly follows the de Gennes relation, $(g_J - 1)^2 J(J+1)$. Here g_J is the Landé g-factor and J is the total angular momentum.

2.1.2 Dense Kondo effect

Contrary to what happens at a large U, higher V_{cf} tends to enhance the hybridization of the $4f$ electrons with conduction electrons, thus accelerating the delocalization of the $4f$ electrons. The delocalization of the $4f$ electrons tends to make the $4f$ band wide. When $E_f > V_{cf}$, the $4f$ electrons are still better localized and the Kondo regime are expected in the Ce compounds.

The study of Kondo effect began when a low temperature resistance minimum was found for non-magnetic metals with ppm-order magnetic impurities. Kondo showed theoretically that the logarithmic resistivity increase at low temperatures as a result of the spin-flip scattering of the conduction electrons by the localized magnetic moments of impurities.[4] In the $3d$ based dilute alloys, the magnetic impurity Kondo effects can be observed only in the case of very low concentration $3d$ magnetic impurities. This is because the degeneracy of the localized spins is very important for the Kondo effect. When the concentration of $3d$ magnetic impurities is increased, the $3d$ elements would come near each other and thus the overlapping or interaction between $3d$ shells would occur, which would lift the degeneracy of the impurity spin and suppress the Kondo spin-flip process.

Since the observation of the $\rho(T) \sim \ln T$ dependence in $CeAl_2$ by Buschow *et al.*,[9]

many rare earth compounds, in particular, Ce compounds were found to show the anomalous behavior similar to the impurity Kondo effect. In these compounds, the $4f$ ions have very high concentration and can even form the crystalline lattice with the anions and thus it cannot be considered as the impurities. From the appearance of a Kondo-like behavior, this phenomenon is called the dense Kondo effect.

The property of the dense Kondo effect at high temperatures is the same as that of the dilute system, but at low temperatures it is quite different in behavior. For instance, we show the temperature dependence of the electrical resistivity in $Ce_xLa_{1-x}Cu_6$[10] in Fig. 2.2. This resistivity increases logarithmically with decreasing the temperature for all

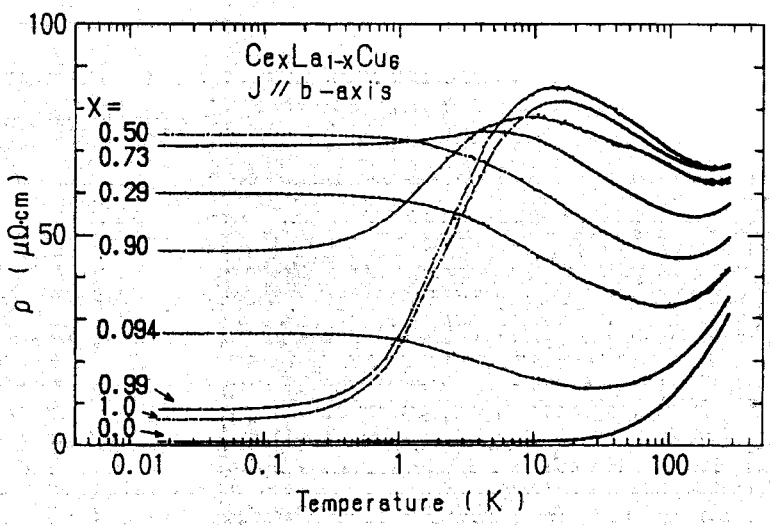

Fig. 2.2 Temperature dependence of the electrical resistivity in $Ce_xLa_{1-x}Cu_6$.[10]

range of concentration. The Kondo effect occurs independently at each Ce site, because the slope of the logarithmically curve is almost proportional to the concentration of Ce. In $CeCu_6$ the behavior is, however, very different from the dilute Kondo impurity system. The resistivity increases with decreasing the temperature, forms a maximum around 15 K and decrease rapidly at lower temperatures to a unitary limit value. This behavior is in contrast to the dilute system characterized by a resistivity minimum.

The many-body Kondo bound state is now understood as follows: For the simplest case of no orbital degeneracy, the localized spin $S(\uparrow)$ is coupled antiferromagnetically with the conduction electrons $s(\downarrow)$. Consequently the singlet state $\{S(\uparrow)\cdot s(\downarrow) \pm S(\downarrow)\cdot s(\uparrow)\}$ is formed with the binding energy $k_B T_K$. Here the Kondo temperature T_K is the single energy scale. In other words, disappearance of the localized moment is thought to be due to the formation of a spin-compensating cloud of the electrons around the impurity moment.

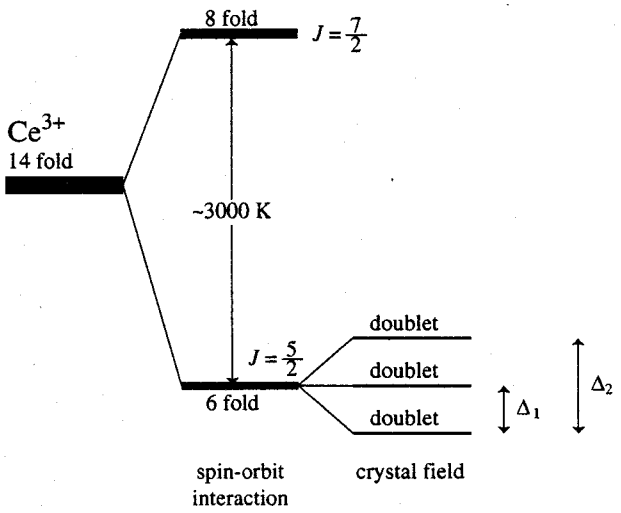

Fig. 2.3 Level scheme of the $4f$ electron in Ce^{3+}.

The Kondo temperature in the Ce compounds is large compared to the magnetic ordering temperature based on the RKKY interaction. For example, the Ce ion is trivalent ($J = \frac{5}{2}$) and the $4f$ energy level is split into the three doublets by the crystalline electric field, namely possessing the splitting energy of Δ_1 and Δ_2 as shown in Fig. 2.3. The Kondo temperature is given as follows:[11)]

$$T_{\mathrm{K}}^{\mathrm{h}} = D\exp\left(-\frac{1}{3|J_{cf}|D(E_{\mathrm{F}})}\right) \qquad \text{when } T > \Delta_1, \Delta_2, \tag{2.1}$$

and

$$T_{\mathrm{K}} = \frac{D^2}{\Delta_1\Delta_2}D\exp\left(-\frac{1}{|J_{cf}|D(E_{\mathrm{F}})}\right) \quad \text{when } T < \Delta_1, \Delta_2. \tag{2.2}$$

Here D, $|J_{cf}|$ and $D(E_{\mathrm{F}})$ are the band width, exchange energy and the density of states at the Fermi energy E_{F}, respectively. If we assume $T_{\mathrm{K}} \simeq 5$ K, for $D = 10^4$ K, $\Delta_1 = 100$ K and $\Delta_2 = 200$ K, the value of $T_{\mathrm{K}}^{\mathrm{h}} \simeq 50$ K is obtained, which is compared to the $S = \frac{1}{2}$-Kondo temperature of 10^{-3} K defined as $T_{\mathrm{K}}^0 = D\exp(-1/|J_{cf}|D(E_{\mathrm{F}}))$. These large values of the Kondo temperature shown in eqs. (2.1) and (2.2) are due to the orbital degeneracy of the $4f$ levels. Therefore, even at low temperatures the Kondo temperature is not T_{K}^0 but T_{K} shown in eq. (2.2).

On the other hand, the magnetic ordering temperature is about 5 K in the Ce compounds, which can be simply estimated from the de Gennes relation under the consideration of the Curie temperature of about 300 K in Gd. Therefore, it depends on the compound whether magnetic ordering occurs at low temperatures or not.

2.1.3 Heavy fermion system

The ground state properties of the dense Kondo system are interesting in magnetism, which are highly different from the dilute Kondo system. In the cerium intermetallic compounds such as $CeCu_6$, cerium ions are periodically aligned whose ground state cannot be a scattering state but becomes a coherent Kondo-lattice state.

The effective mass of the conduction electron in the Kondo lattice of $CeCu_6$ is extremely large, compared with the one of the free electron. It is reflected in the specific heat coefficient γ and magnetic susceptibility $\chi(0)$, which can be expressed as

$$\gamma = \frac{2\pi^2 {k_B}^2}{3} D(E_F) \tag{2.3a}$$

$$= \frac{{k_B}^2 k_F}{3\hbar^2} m^* \qquad \text{(free electron model)}, \tag{2.3b}$$

and

$$\chi(0) = 2{\mu_B}^2 D(E_F) \tag{2.4a}$$

$$= {\mu_B}^2 \frac{k_F}{\pi^2\hbar^2} m^* \quad \text{(free electron model)}, \tag{2.4b}$$

where k_F is Fermi wave number. These parameters are proportional to the effective mass. The electrical resistivity ρ decreases steeply with decreasing the temperature, following a Fermi liquid behavior as $\rho \sim AT^2$ with a large value of the coefficient A.[12] The $\sqrt{A}$ value is proportional to the effective mass of the carrier m^* and thus inversely proportional to the Kondo temperature. Correspondingly, the electronic specific heat coefficient γ roughly follows the simple relation $\gamma \sim 10^4/T_K$ (mJ/K^2·mol) because the Kramers doublet of the $4f$ levels is changed into the γ value in the Ce compound:

$$R\ln 2 = \int_0^{T_K} \frac{C}{T} dT, \tag{2.5}$$

$$C = \gamma T, \tag{2.6}$$

thus

$$\gamma = \frac{R\ln 2}{T_K} = \frac{5.8 \times 10^3}{T_K} \text{ (mJ/K}^2\text{·mol)}. \tag{2.7}$$

It reaches 1600 mJ/K^2·mol for $CeCu_6$[7] because of a small Kondo temperature of 4–5 K. The conduction electrons possess large effective masses and thus move slowly in the crystal. Actually in $CeRu_2Si_2$ an extremely heavy electron of $120m_0$ was detected from the de Haas-van Alphen (dHvA) effect measurements.[13,14] Therefore the Kondo-lattice system is called a heavy fermion or heavy electron system. The Ce Kondo-lattice

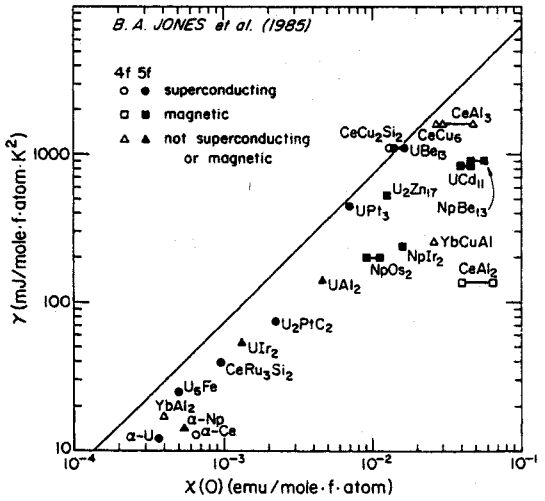

Fig. 2.4 The specific heat coefficient versus the susceptibility for some heavy fermion systems. The values are extrapolated to zero by a variety of methods. Any free, noninteracting fermion gas would lie on the straight line.[17]

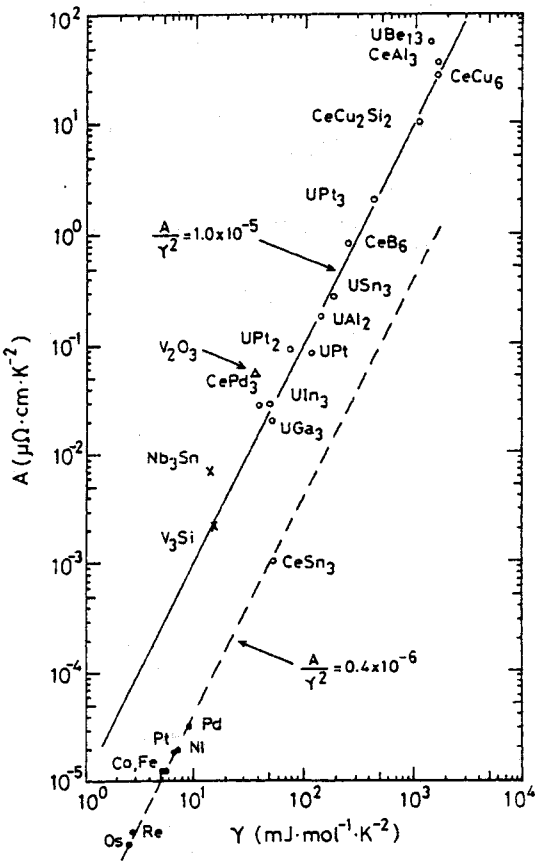

Fig. 2.5 A vs γ in the logarithmic scale.[18]

compound with magnetic ordering also possesses the large γ value even if the RKKY interaction overcomes the Kondo effect at low temperatures. For example, the γ value of CeB_6 is 250 mJ/K^2·mol,[15] which is roughly one hundred times as large as that of LaB_6, 2.6 mJ/K^2·mol.[16]

A significant correlation factor is thought to be the ratio of the measured magnetic susceptibility $\chi(0)$ to the observed γ value:

$$R_{\mathrm{W}} \equiv \left(\frac{\pi^2 {k_{\mathrm{B}}}^2}{\gamma}\right)\left(\frac{\chi(0)}{{\mu_{\mathrm{B}}}^2 {g_J}^2 J(J+1)}\right). \tag{2.8}$$

This ratio R_{W} is called Wilson-Sommerfeld ratio. Stewart[19] evaluated R_{W} for the heavy fermion system as shown in Fig. 2.4. He suggested that in the f electron system R_{W} is not 1 but roughly 2. Kadowaki and Woods stressed the importance of a universal relationship between A and γ as shown in Fig. 2.5.[20] They noted that the ration A/γ has a common value of 1.0×10^{-5} $\mu\Omega$·cm·K^2·mol^2/mJ^2.

2.1.4 Competition between the RKKY interaction and the Kondo effect

The Kondo effect can be parameterized by a single energy scale T_K. The hierarchy of ordering temperatures can be qualitatively understood by a competition between the Kondo screening and the tendency towards magnetic ordering via RKKY-type indirect exchange mechanism. The magnitude of an indirect RKKY interaction can be characterized by the ordering temperature T_{RKKY} as follows:

$$T_{RKKY} \propto |J_{cf}|^2 D(E_F), \tag{2.9}$$

where

$$J_{cf} \simeq \frac{{V_{cf}}^2}{E_F - E_f}. \tag{2.10}$$

Actually the intensity of this interaction is also dominated by the de Gennes factor and eq. (2.9) is given by the product with coefficient as $(g_J - 1)^2 J(J+1)$. This leads to the phase diagram for a Kondo lattice, originally derived by Doniach[5] and emphasized by Brandt and Moshchalkov.[6] Figure 2.6 is well known as the Doniach phase diagram. If $|J_{cf}|D(E_F)$ is small, the compound becomes antiferromagnet with a large magnetic moment, while with increasing $|J_{cf}|D(E_F)$ both the magnetic moment and the ordering temperature tend to zero. The critical point where T_N becomes zero is called a "quantum

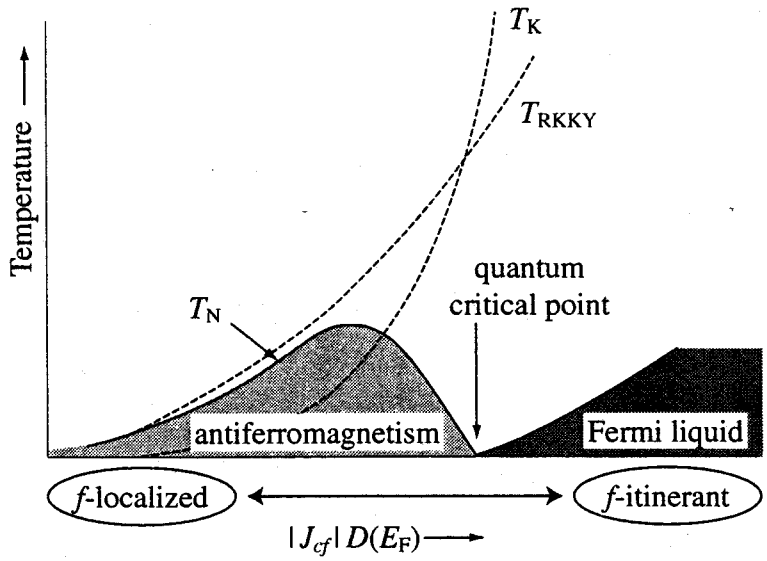

Fig. 2.6 Doniach phase diagram.[6]

critical point". Above the quantum critical point, Kondo-lattice paramagnets show up and consequently the f-atom valency becomes unstable, leading to the heavy fermion system.

The non-Fermi liquid behavior around the quantum critical point is one of the recent topics in the f electron system. Here, the heavy fermion system is based on the Landau's Fermi liquid, where the interacting electron system or the heavy electron system is related to the non-interacting one by the scaling law without a phase transition. The characteristic features are $\rho = \rho_0 + AT^2$, $C/T = \gamma$ and $\chi = \chi(0)$ at low temperatures, as mentioned in Sec. 2.1.3. On the other hand, in the non-Fermi liquid system the following relations are characterized:

$$\rho \sim T^m \quad \text{with } m < 2, \tag{2.11}$$

$$C/T \sim -\log T. \tag{2.12}$$

Nearby the quantum critical point, Ce intermetallic compounds with an extraordinary wide variety of possible ground states are found. These include Kondo-lattice compounds with magnetic ordering ($CeIn_3$, $CeAl_2$, CeB_6), small-moment antiferromagnets ($CePd_2Si_2$, $CeAl_3$), an anisotropic superconductor ($CeCu_2Si_2$), no-ordered Kondo-lattice compounds or the heavy fermion compounds ($CeCu_6$, $CeRu_2Si_2$) and valence fluctuation compounds (CeNi, $CeRh_2$, $CeRu_2$, $CeSn_3$).

We note the non-magnetic Ce compounds at low temperatures. In $CeCu_6$ and $CeRu_2Si_2$ with a small Kondo temperature, there exist no magnetic ordering but antiferromagnetic correlations between the Ce sites,[21] showing the metamagnetic transition in the magnetic field: $H_c = 2$ T in $CeCu_6$[22] and 8 T in $CeRu_2Si_2$.[23] The results of dHvA experiments[14,24,25] and the band calculations[26] in $CeRu_2Si_2$ show that $4f$ electrons are itinerant. Namely the $4f$ electrons in Ce compounds such as $CeSn_3$ with a large Kondo temperature, which belong to the valence-fluctuation regime, are also itinerant in the ground state and contribute directly to the formation of the Fermi surface.[27,28]

Finally we also pay attention to the non-magnetic Ce compounds to clarify the magnitude of Kondo temperature reflected in the magnetic susceptibility. Figure 2.7 shows the temperature dependence of the magnetic susceptibility in some Ce compounds without magnetic ordering: $CeCu_6$ (T_K = 3–4 K), $CeRu_2Si_2$ (20 K), CeNi (150 K) and $CeSn_3$ (200 K). The magnetic susceptibility in these compounds follows the Curie-Weiss law at higher temperatures, possessing the magnetic moment near Ce^{3+} of $2.54\mu_B$, while it becomes approximately temperature-independent with decreasing the temperature, namely showing a broad maximum and then forming enhanced Pauli paramagnetism. The temperature indicating the peak of the susceptibility almost corresponds to the characteristic

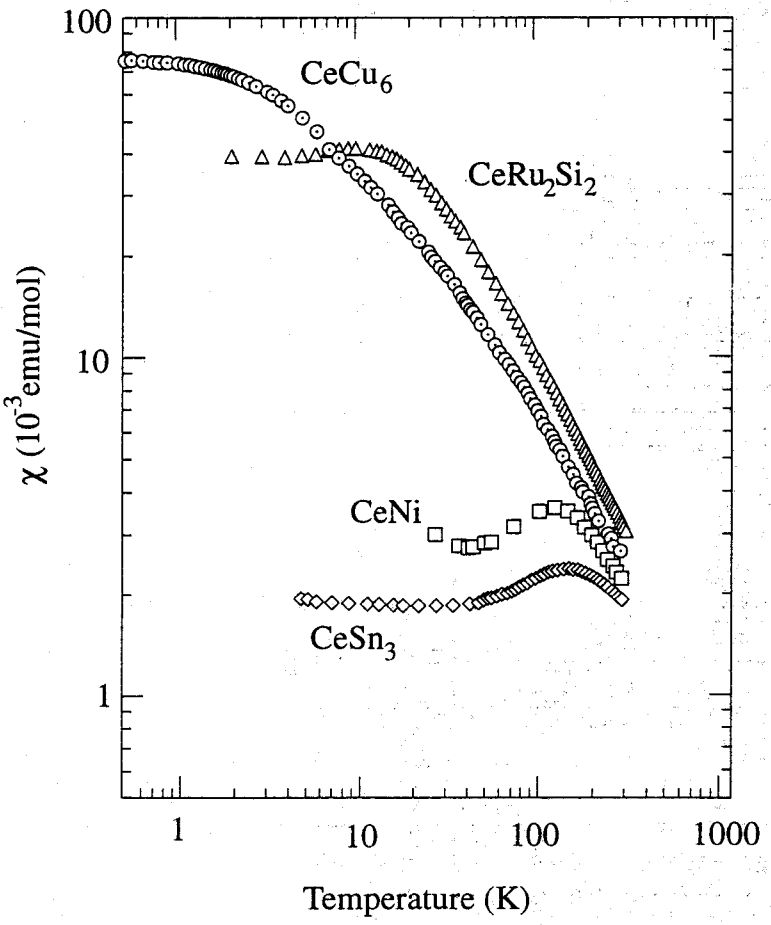

Fig. 2.7 Temperature dependence of the magnetic susceptibility for typical Ce compounds.

temperature T_K. The valence of Ce atoms seems to be changed from Ce^{3+} into Ce^{4+} (non-magnetic state) with decreasing the temperature.

2.1.5 Pressure induced superconductivity

Unconventional superconductivity has been an active area of research for several decades, ever since the discovery of the first heavy fermion superconductor, $CeCu_2Si_2$.[29] Recently, some Ce-based heavy fermion compounds were found to exhibit superconducting under pressure, such as $CeIn_3$ and $CePd_2Si_2$[30] as shown in Figs. 2.8 and 2.9. In these compounds, superconductivity appears around the quantum critical point (see Fig. 2.6). The similar pressure-induced superconductivity was also reported for the other Ce-based compounds such as $CeCu_2Ge_2$,[31] $CeRh_2Si_2$[32,33] and $CeRhIn_5$.[34] In these superconduc-

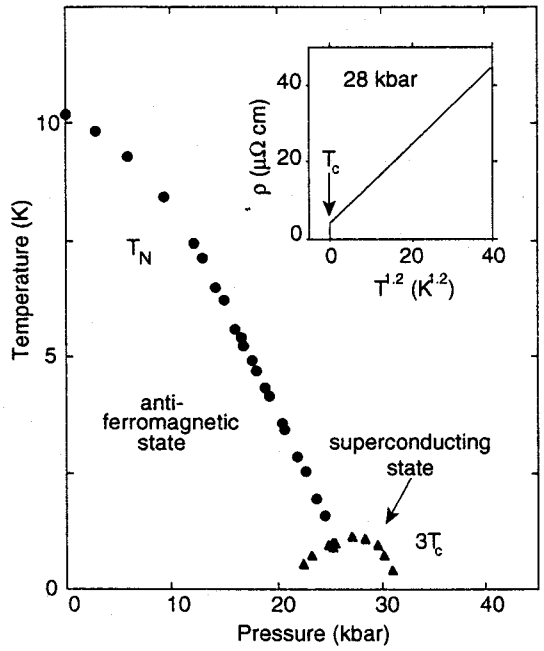

Fig. 2.8 Temperature-pressure phase diagram of $CePd_2Si_2$. Superconductivity appears below T_c in a narrow window where Néel temperature T_N tends to absolute zero.[30]

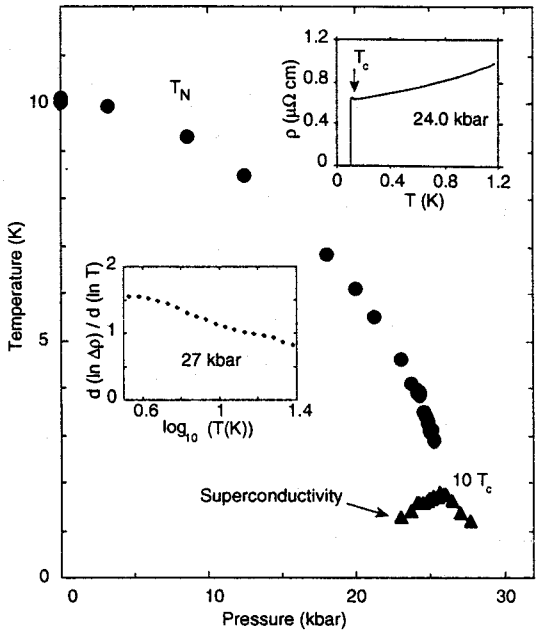

Fig. 2.9 Temperature-pressure phase diagram of $CeIn_3$. Superconductivity is observed in a narrow window near p_c, the pressure at which the Néel temperature T_N tends to absolute zero.[30]

tivity, the attractive force between quasiparticles are possible to be magnetically mediated, not to be phonon-mediated.

As mention above, pressure induced superconductivity had been discovered in the antiferromagnetic Ce compounds. Surprisingly, Saxena *et al.*[35] found the pressure induced superconductivity in a ferromagnet UGe_2. In this case, superconductivity appears inside the border of ferromagnetism.

2.1.6 Fermi surface study

Fermi surface studies are very important to know the ground-state properties of the rare earth compounds.[8] As mentioned in Sec. 2.1.4, the ground state of the Ce compounds is mainly determined by the competition between the RKKY interaction and the Kondo effect (see Fig. 2.6). When T_{RKKY} overcomes T_K, the ground state is the magnetic ordered one and $4f$ electron is regarded as localized. On the other hand, when T_K is dominant, the ground state is the non-magnetic one and the $4f$ electrons become itinerant.

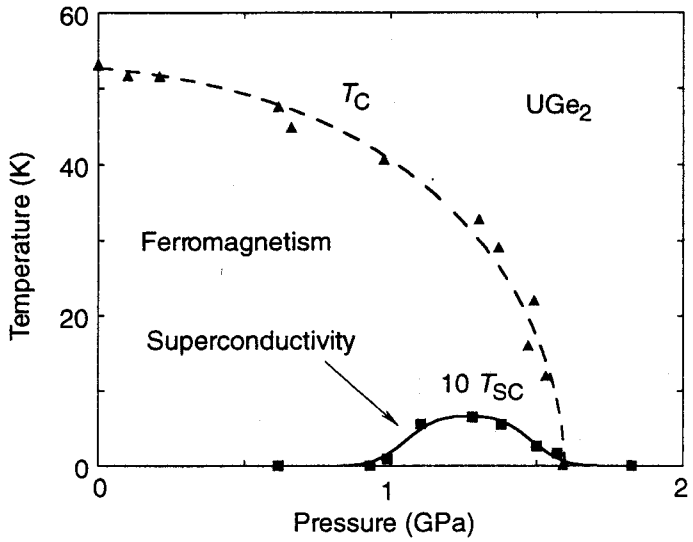

Fig. 2.10 Temperature-pressure phase diagram of UGe_2. T_c denotes the Curie temperature and T_{sc} the superconducting transition temperature.[35)]

In the $4f$-localized system, the Fermi surface is similar to that of corresponding La compound, but the presence of $4f$ electrons alters the Fermi surface through the $4f$-electron contribution to the crystal potential and through the introduction of new Brillouin zone boundaries and magnetic energy gaps which occur when $4f$-electron moments order. The latter effect may be approximated by a band-folding procedure where the paramagnetic Fermi surface is folded into smaller Brillouin zone based on the magnetic unit cell, which is larger than the chemical one. If the magnetic energy gaps associated with the magnetic structure are small enough, conduction electrons undergoing cyclotron motion in the presence of magnetic field can tunnel through these gaps and circulate the orbit on the paramagnetic Fermi surface. If this magnetic breakthrough (breakdown) effect occurs, the paramagnetic Fermi surface may be observed in the dHvA effect even in the presence of magnetic order.

For Kondo-lattice compounds with magnetic ordering, the Kondo effect is expected to have minor influence on the topology of the Fermi surface, representing that the Fermi surfaces of the Ce compounds are roughly similar to those of the corresponding La compounds, but are altered by the magnetic Brillouin zone boundaries mentioned above. Nevertheless the effective masses of the conduction carriers are extremely large compared to those of La compounds. In this system a small amount of $4f$ electron most likely contributes to make a sharp density of states at the Fermi energy. Thus the energy band becomes flat around the Fermi energy, which brings about the large mass.

In some Ce compounds such as $CeCu_6$, $CeRu_2Si_2$, CeNi and $CeSn_3$, the magnetic susceptibility follows the Curie-Weiss law with a moment of Ce^{3+}, $2.54\mu_B$/Ce, has a maximum at a characteristic temperature $T_{\chi max}$, and becomes constant at lower temperatures (see Fig. 2.7). This characteristic temperature $T_{\chi max}$ corresponds to the Kondo temperature T_K as mentioned in Sec. 2.1.4. A characteristic peak in the susceptibility is a crossover from the localized $4f$ electron to the itinerant one. The Fermi surface is thus highly different from that of the corresponding La compound. The cyclotron mass is also extremely large, reflecting a large γ-value of $\gamma \simeq 10^4/T_K$ (mJ/K^2·mol).

2.2 Characteristic Properties of $CeRh_2Si_2$

$CeRh_2Si_2$ have the tetragonal ($ThCr_2Si_2$-type) crystal structure with space group $I4/mmm$ (D_{4h}^{17}), which is shown in Fig. 2.11. The lattice parameters are $a = 4.09$Å and $c = 10.18$Å.[36,37]

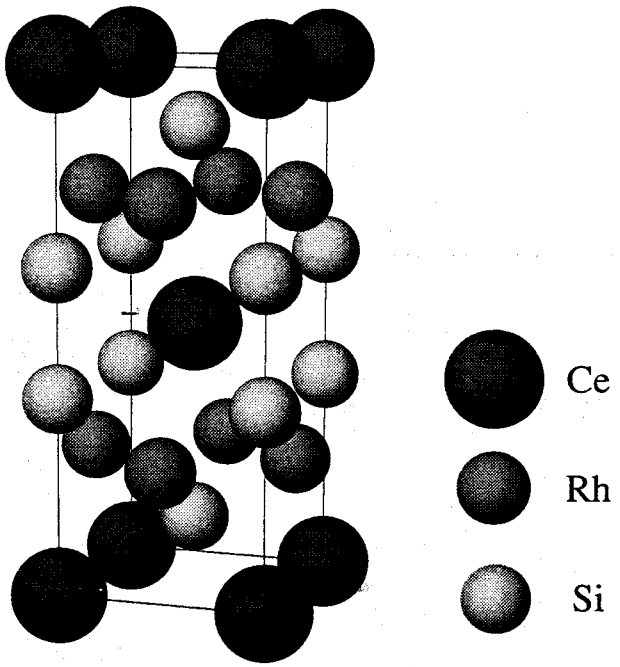

Fig. 2.11 Crystal structure of $CeRh_2Si_2$.

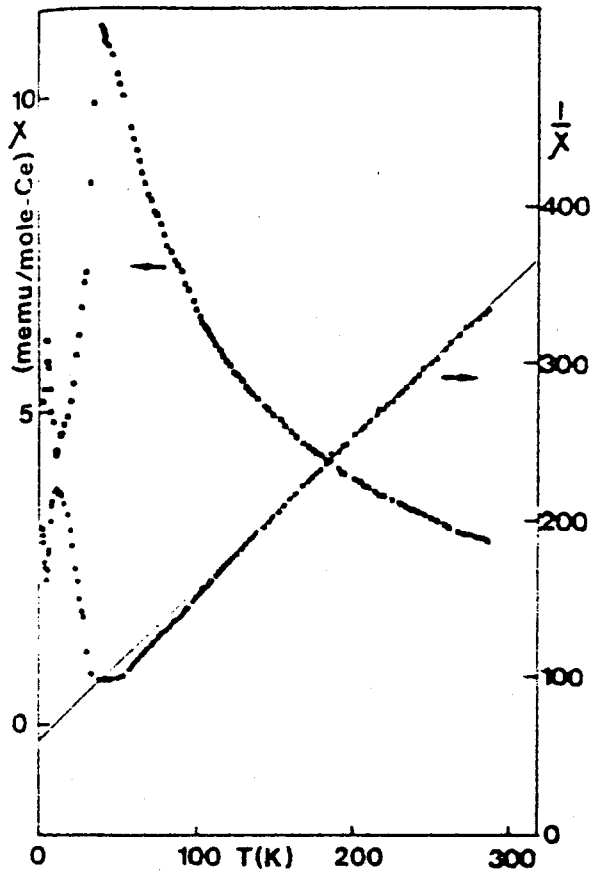

Fig. 2.12 Temperature dependence of the magnetic susceptibility and inverse susceptibility of $CeRh_2Si_2$.[36)]

Figure 2.12 shows the temperature dependence of the magnetic susceptibility in $CeRh_2Si_2$.[36)] The susceptibility follows the Curie-Weiss law $\chi = C/(T-\theta_p)$ above 130 K. A paramagnetic Curie temperature is a large negative value of $\theta_p = -72$ K and an effective moment is $\mu_{eff} = 2.9\mu_B$ per cerium ion, which is about 20% larger than the moment of the value of free Ce^{3+}, $2.54\mu_B$/Ce. This difference is mainly due to a large crystalline electric field (CEF) effect. The susceptibility exhibits a cusp-like peak at $T_{N1} = 37$ K, which is due to antiferromagnetic ordering.

Grier *et al.* performed the neutron diffraction experiments on $CeRh_2Si_2$.[37)] Two magnetic transitions were observed. The first occurs at $T_{N1} = 39$ K, with the appearance of peaks corresponding to a $(\frac{1}{2}\,\frac{1}{2}\,0)$ magnetic structure. The ratio of the integrated intensity of the $(\frac{1}{2}\,\frac{1}{2}\,0)$ peak to that of the $(\frac{1}{2}\,\frac{1}{2}\,2)$ is 2.6±0.2 compared to a calculated ratio of 2.63 for a $(\frac{1}{2}\,\frac{1}{2}\,0)$ ordering with the spins in the c-axis, the [001] direction. The second

transition occurs at $T_{N2} = 27$ K. At this temperature peaks which can be indexed on the basis of a $(\frac{1}{2}\,\frac{1}{2}\,\frac{1}{2})$ magnetic structure appear. The $(\frac{1}{2}\,\frac{1}{2}\,0)$ peaks begin to decrease as the temperature is lowered, but level off and remain relatively constant below 25 K.

Recently, Kawarazaki *et al.* studied the neutron diffraction experiments at ambient pressure and under high pressure.[38] Figure 2.13 shows the plots of the peak intensities of the reflections from the single-crystalline sample as a function of temperature. We can see that the intensity ratio of the reflections at $\boldsymbol{q}_1^+ = (\frac{1}{2}\,\frac{1}{2}\,0)$, $\boldsymbol{q}_1^- = (\frac{\bar{1}}{2}\,\frac{1}{2}\,0)$ and $\boldsymbol{q}_2 = (\frac{1}{2}\,\frac{1}{2}\,\frac{1}{2})$ at the lowest temperature is 1:1:2 within an experimental error. They suggested that the magnetic structure at lower temperature than T_{N2} is 4-$\boldsymbol{q}$ structure as shown in Fig. 2.14. In this configuration, the magnitude of moment at the corners and the centers are calculated to be $1.42\mu_B$ and $1.34\mu_B$, respectively.

Figure 2.15 shows T_{N1} and T_{N2} as a function of applied pressure. In this figure, we can see that both T_{N1} and T_{N2} decrease with increasing pressure and the system becomes non-magnetic under pressure greater than the critical pressure $p_c = 1.1$ GPa and also that the change of T_{N1} is very steep around p_c.

Figure 2.16 shows the temperature dependence of the electrical resistivity at various

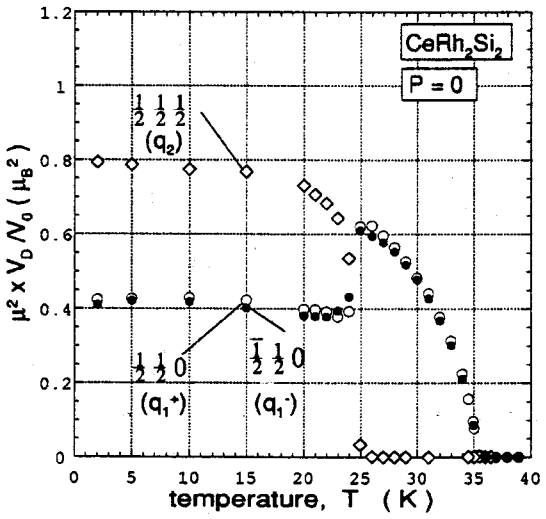

Fig. 2.13 The temperature dependences of the intensities of the three magnetic Bragg reflections from the single-crystalline $CeRh_2Si_2$ at ambient pressure. The intensities have been corrected so that they represent the product of the relative domain volume V_D/V_0, and the square of the magnetic moment.[38]

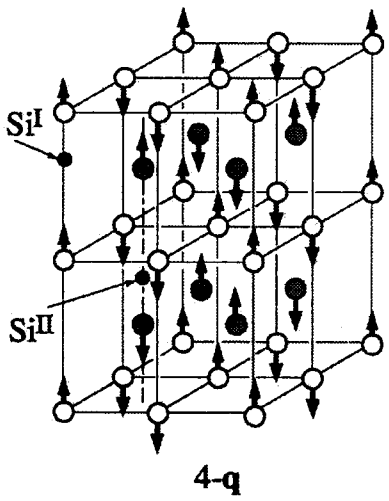

Fig. 2.14 The spin configuration of the 4-$\boldsymbol{q}$ structure of $CeRh_2Si_2$.[38]

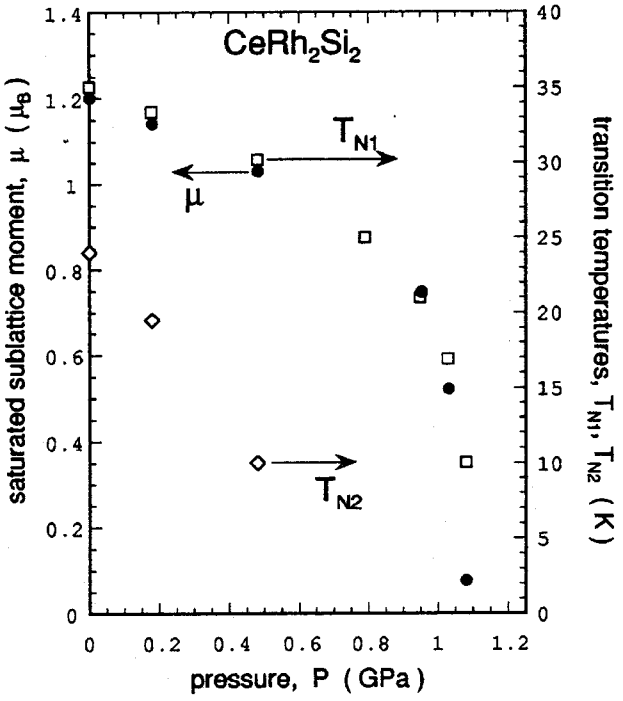

Fig. 2.15 The saturated sublattice moment (per cerium atom) and the transition temperatures as functions of the applied pressure.[38)]

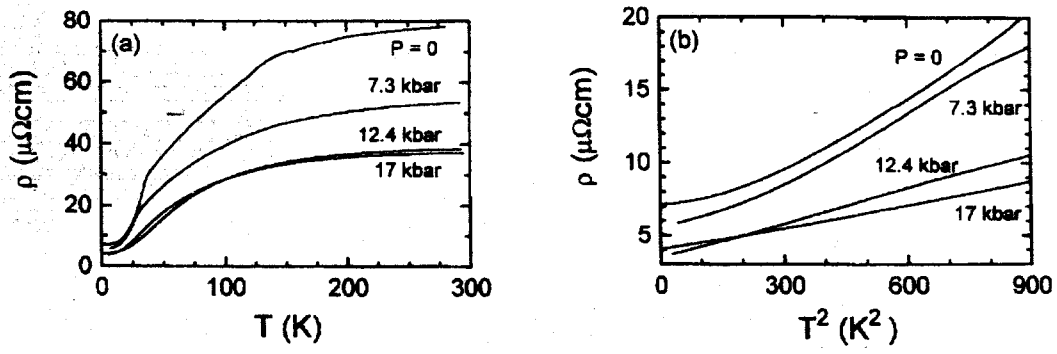

Fig. 2.16 (a)Electrical resistivity ρ versus temperature for $CeRh_2Si_2$ at various applied pressures. (b)Expanded view of the low temperature variation of $\rho(T)$.[32)]

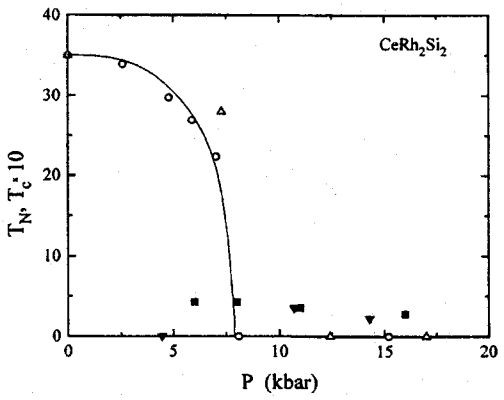

Fig. 2.17 P-T phase diagram of $CeRh_2Si_2$. Open symbols represent the antiferromagnetic ordering transition $T_N(P)$. Solid symbols are $T_c(P)$ points of the superconducting transitions obtained the onset of suppression of resistivity for several samples that are represented by different symbols. Notice the different temperature scales for the two phase transitions.[33)]

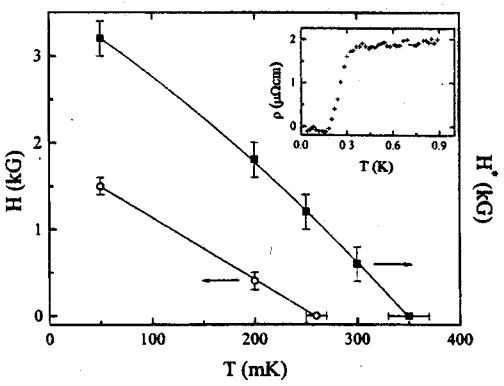

Fig. 2.18 Magnetic field at the onset of suppression of resistivity (solid squares) and the midpoint of the transition (open circles) as a function of temperature at a pressure of 11.0±0.3 kbar. Inset, superconducting transition displayed in resistivity data at 11.0±0.3 kbar.[33)]

applied pressures. At ambient pressure the Néel temperature is indicated by a sharp drop. With increasing pressure, T_N moves rapidly to lower temperatures; at 12.4 kbar, there is no obvious evidence for a magnetic transition. As shown in Fig. 2.16(b), at ambient and 7.3 kbar pressures, the resistivity increases approximately as T^3, but once antiferromagnetic order is suppressed, a Fermi-liquid T^2-dependence develops over a low-temperature interval that increases with pressure and with a slope that decreases correspondingly.

The pressure dependence of T_N, plotted in Fig. 2.17 by solid symbols, shows that $T_N \to 0$ is attained at a critical pressure $p_c = 9 \pm 1$ kbar. The inset of Fig. 2.18 shows the temperature dependence of the resistivity at 11.0±0.3 kbar. The superconducting resistivity drop occurs at 350 mK. The pressure dependence of the superconducting transition temperature T_c is plotted in Fig 2.17 by open symbols. The superconductivity appears around p_c. Figure 2.18 shows the superconducting phase diagram, namely the temperature dependence of upper critical field H_{c2}, which is defined as an onset and a midpoint of the resistivity drop, H^* and H.

The inset in figure 2.20 shows the magnetic specific heat $C_m(T) = C_{CeRh_2Si_2}(T) - C_{LaRh_2Si_2}(T)$ divided by temperature, C_m/T, and the corresponding magnetic entropy $S(T)$ of $CeRh_2Si_2$.[39)] The peak in C_m/T at 35 K corresponds to the onset of antiferro-

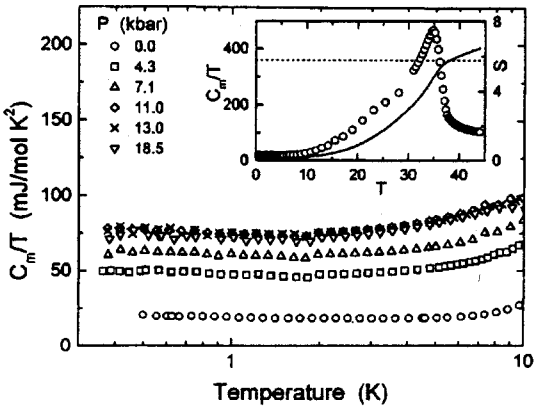

Fig. 2.19 Magnetic specific heat C_m divided by temperature as a function of a logarithmic scale for $CeRh_2Si_2$ at various pressures. The inset is a plot of C_m/T vs T for $CeRh_2Si_2$ at ambient pressure. The solid curve is the magnetic entropy, and the dotted horizonal line corresponds to $S_m = R\ln 2$.[39)]

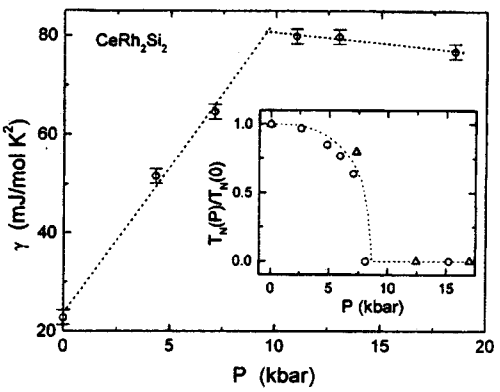

Fig. 2.20 Linear-in-temperature specific heat coefficient γ of $CeRh_2Si_2$ as a function of pressure. The inset is a plot of $T_N(P)$ normalized to its $P = 0$ value for two different samples. In both cases, the dotted constructions are guides to eyes.[39)]

magnetic order, as also found in the magnetic susceptibility. Moreover, there is a kink in C_m/T around $T_{N2} = 25$ K, which corresponds to the transition of magnetic structure. The entropy reaches almost full $R\ln 2$ at T_{N1}, consistent with magnetic ordering in a doublet ground state. Quasielastic neutron scattering[40)] gives a Kondo temperature $T_K = 33$ K just above T_{N1}. Consequently, most of the magnetic entropy should be associated with ordering of the $4f$ moments. In the absence of ordering, the electronic specific heat coefficient can be estimated from $\gamma = (N-1)\pi R/6T_K$, where N is the groundstate degeneracy ($N = 2$ in this case) and R is gas constant. From this single Kondo impurity relationship, $\gamma = 130$ mJ/K^2·mol was calculated. The observed T linear contribution to C_m at low temperatures was 22.8 mJ/K^2·mol. This large reduction of γ in the ordered state is found commonly in Ce-based magnets and may be attributed to the existence of a large internal magnetic field produced by the $4f$-moment ordering that quenches, at least partially, Kondo-like spin fluctuations.

Figure 2.19 shows the effect of pressure on C_m/T at $T \leq 10$ K. With the application of pressure, there is qualitative increase in C_m/T at all temperatures. However, for higher pressures, γ does decrease, approximately linearly, with increasing pressure. The linear-in-pressure constructions in Fig. 2.20 shows that the crossover from $\partial\gamma/\partial P > 0$ to $\partial\gamma/\partial P < 0$ occurs very near p_c. Qualitatively, this behavior of $\gamma(P)$ can be understood

on the basis of Doniach model (Sect. 2.1.4).

The de Haas-van Alphen (dHvA) measurements were carried out by Abe *et al.*[41] Figure 2.21 shows the angular dependence of the dHvA frequencies. Many branches were observed, but most branches were observed only slight angle region centered at symmetrical axis. The cyclotron effective mass determined range from 0.44 to $4.4m_0$, but that of most branch was not determined.

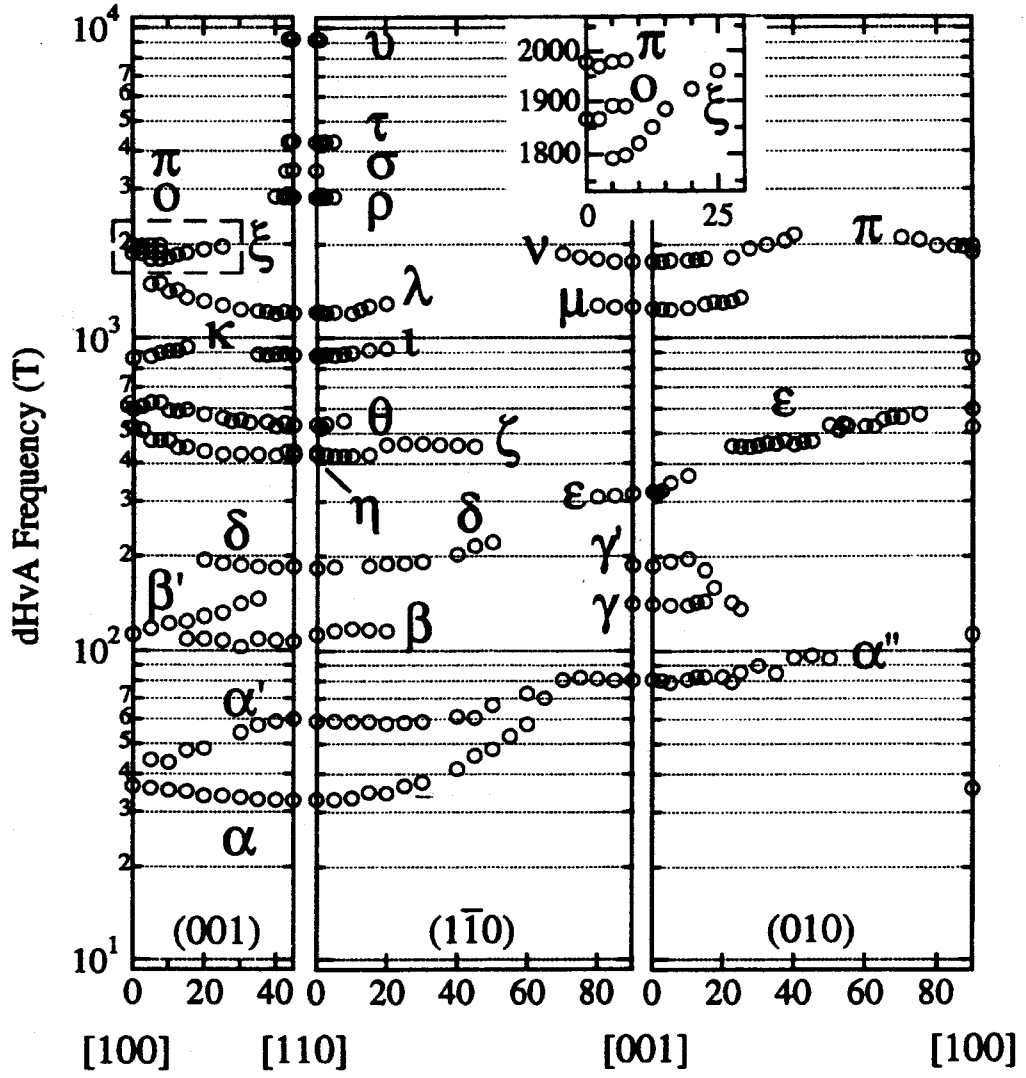

Fig. 2.21 Angular dependence of the dHvA frequencies in the measurement field region from 2 T to 16 T. The inset figure indicates the expanded plot of the ξ-, o- and π-branches in a dotted rectangle.[41]

2.3 Characteristic Properties of CeNi

CeNi have the orthorhombic (CrB-type) crystal structure with space group $Cmcm$, which is shown in Fig. 2.22. The lattice parameters are $a = 3.77$Å $b = 10.46$Å and $c = 4.37$Å.[42]

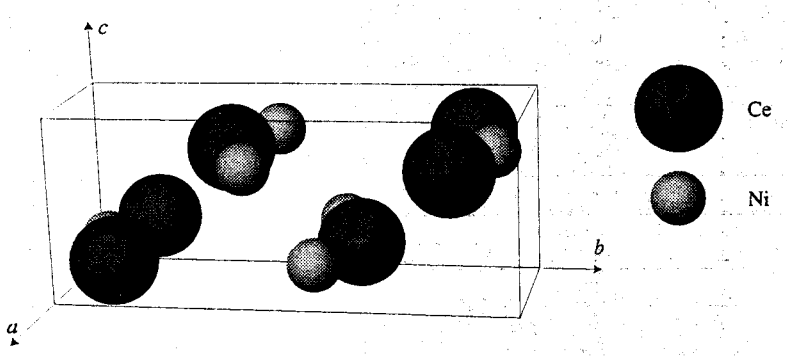

Fig. 2.22 Crystal structure of CeNi.

Figure 2.23 shows the temperature dependence of the magnetic susceptibility of CeNi.[43] The magnetic susceptibility is anisotropic, reflecting the CEF effect. At higher temperatures than 180 K, the susceptibility follows the Curie-Weiss law, but a Curie constant is lower than that of a free Ce^{3+} ion, indicating an intermediate valence. The susceptibility makes a broad maximum around 140 K and decreases with decreasing temperature.

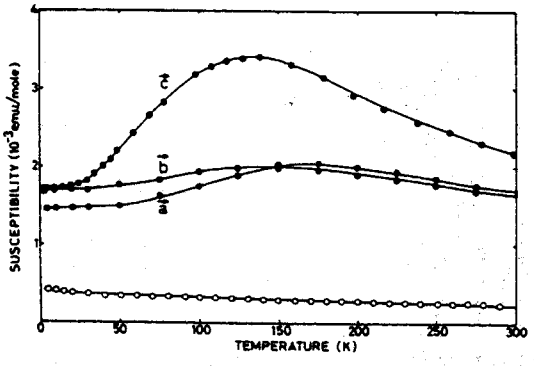

Fig. 2.23 Temperature dependence of the magnetic susceptibility of CeNi (•) and LaNi (○).[43]

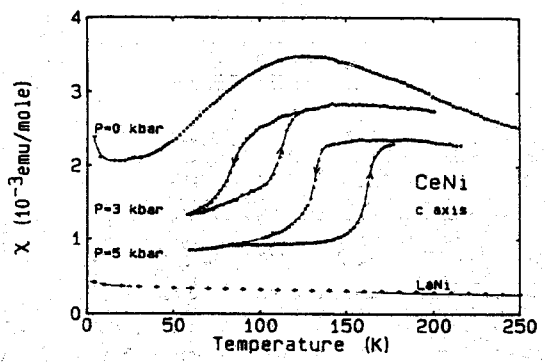

Fig. 2.24 Temperature dependence of the magnetic susceptibility of CeNi for the field along the c-axis under pressures.[44]

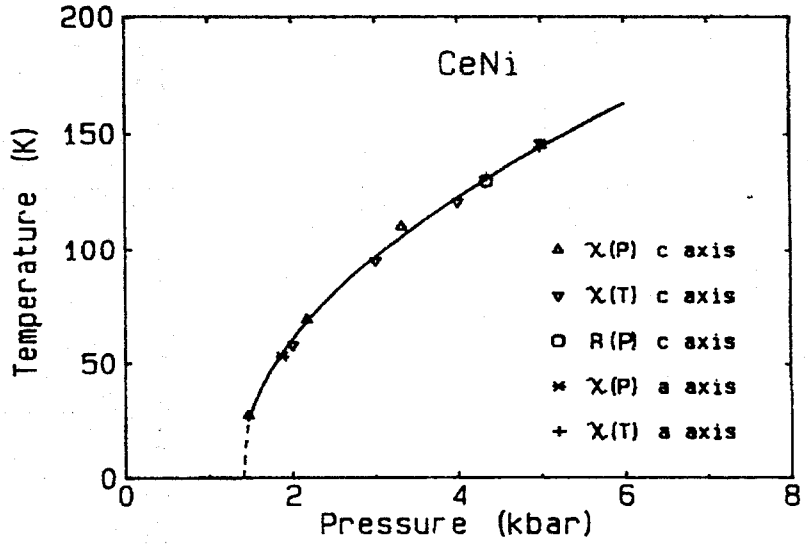

Fig. 2.25 T-P diagram of the low and high magnetic states in CeNi.[44]

Figure 2.24 shows the temperature dependence of the susceptibility under pressure. A drastic drop of the susceptibility takes place around 150 K at 5 kbar and around 100 K at 3 kbar. It corresponds to a first-order transition with a large hysteresis of a temperature interval ($\simeq$ 25–30 K). We note the susceptibility at low temperatures. At ambient pressure, it is 2.1×10^{-3} emu/mol, with increasing pressure, it decreases and becomes 0.8×10^{-3} emu/mol at 5 kbar. The pressure-temperature phase diagram is shown in Fig. 2.25, in which the data correspond to the mean values of transition width. The extrapolation of the transition line at lower temperatures indicates a critical pressure $p_c \simeq 1.3$ kbar at $T = 0$. The authors pointed out that this transition is analogous to the γ–α transition found in cerium metal.[45]

Figure 2.26 shows the temperature dependence of the specific heat.[43] As seen in an inset of Fig. 2.26, the magnetic part of the specific heat exhibits a maximum at 120 K, which almost coincides with the susceptibility maximum. The electronic specific heat coefficient is $\gamma = 65$ mJ/K^2·mol for CeNi and 5 mJ/K^2·mol for LaNi.[46]

Uwatoko *et al.* measured the thermal expansion coefficient of CeNi under pressure.[47] The thermal expansion coefficient at low temperatures is expressed by the following equation:

$$\frac{\alpha}{T} = A + BT^2, \tag{2.13}$$

where the first term is the electronic and the magnetic contributions, and the second one is the phonon contribution. In Fig. 2.27, the values of α_c/T are plotted as a function

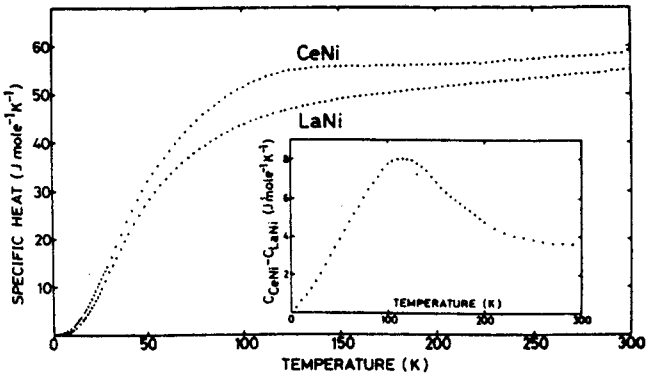

Fig. 2.26 Temperature dependence of the specific heat in CeNi and LaNi.[43]

of T^2 for CeNi below 30 K under pressure. By a linear extrapolation of α_c/T to 0 K, the value of $\alpha_c/T(T=0)=A$, which is proportional to the density of state at Fermi level $D(E_F)$, was obtained. The A value is shown in Fig. 2.28 as a function of pressure. The decreasing rate in the magnitude of A below 5 kbar is larger an that above 10 kbar. This suggests that the decrease in A saturates at high pressure. The present decrease corresponds to a decrease of $D(E_F)$ by applying pressure. In other words, T_K increases with increasing pressure because $D(E_F)$ is roughly proportional to ${T_K}^{-1}$.

Figures 2.29–2.31 show the transverse magnetoresistance $\Delta\rho/\rho=[\rho(H)-\rho(0)]/\rho(0)$ in the a-, b- and c-planes, respectively. In the figures, (a) shows the angular dependence of $\Delta\rho/\rho$ and (b) shows the field dependences for certain characteristic direction of the field, where $\rho(0)$ is the residual resistivity. The magnetoresistance increases with increasing field

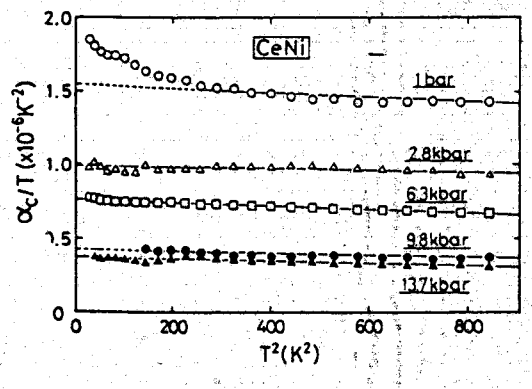

Fig. 2.27 Values of α_c/T as a function of T^2 for CeNi.[47]

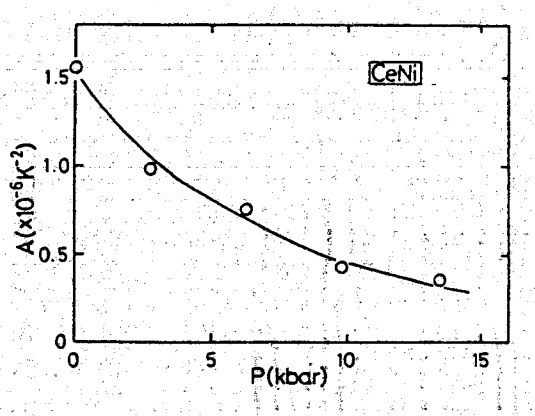

Fig. 2.28 Pressure dependence of A for a CeNi single crystal.[47]

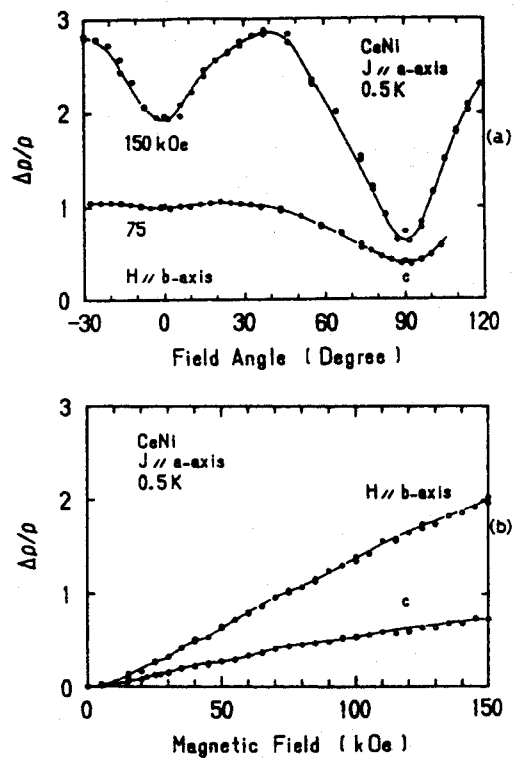

Fig. 2.29 (a) Angular and (b) field dependence of magnetoresistance in the a-plane of CeNi.[48)]

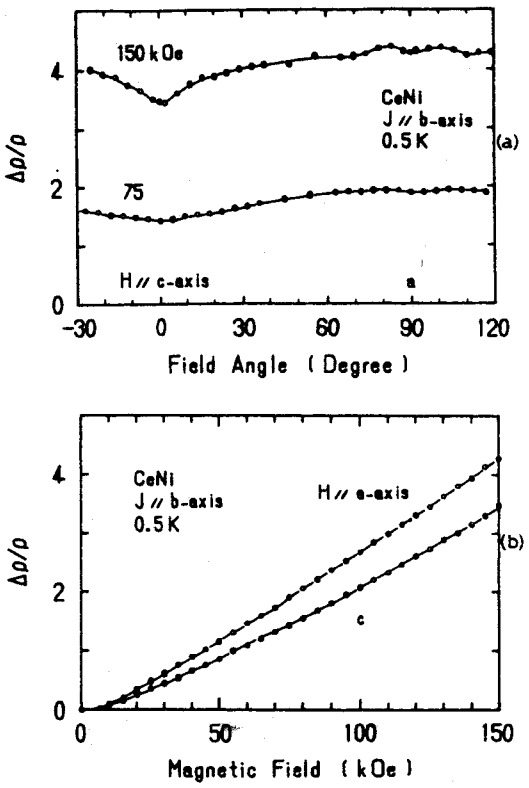

Fig. 2.30 (a) Angular and (b) field dependence of magnetoresistance in the b-plane of CeNi.[48)]

over the wide angle region, following $H^{1.1-1.4}$, although for several particular configuration of the field and the current, the field dependence is not smooth, as shown in Figs. 2.30 and 2.31. This behavior claims that this substance is a compensated metal with equal carrier concentration of electrons and holes. This is consistent with a simple expectation that CeNi possesses an even number of electrons because there exist four molecules of CeNi in a chemical unit cell. The magnetoresistance saturates above 100 kOe, being proportional to $H^{0.6-0.8}$, for the following configurations: the field H is directed along the b- and c-axes with the current J along the a-axis, and the field is along the a-axis with the current along the c-axis. Therefore, the open orbits exist along the b- and c-axes.

The study of the dHvA experiments were performed.[48)] Figure 2.33 shows the typical dHvA oscillations and fast Fourier transformation spectra at 0.43 K in the field along the b-axis. Four dHvA branches were observed. Figure 2.34 shows the angular dependence of dHvA frequencies. Solid lines indicate the experimental result in LaNi.

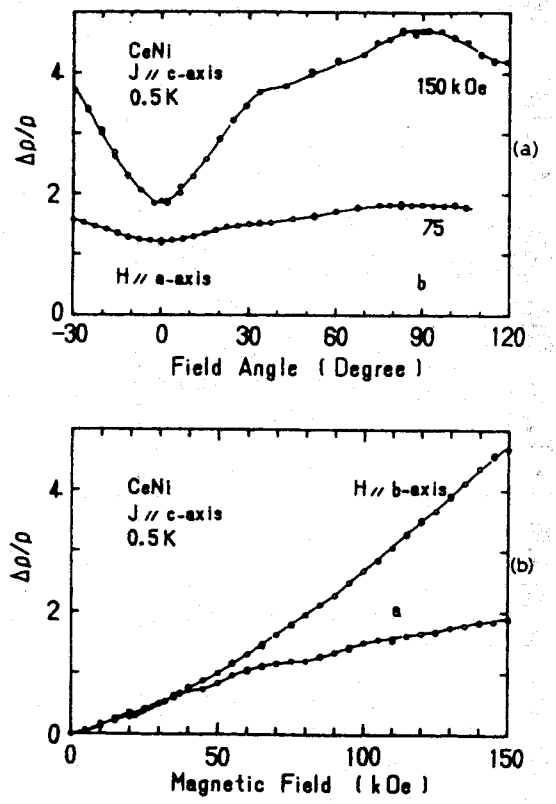

Fig. 2.31 (a) Angular and (b) field dependence of magnetoresistance in the c-plane of CeNi.[48]

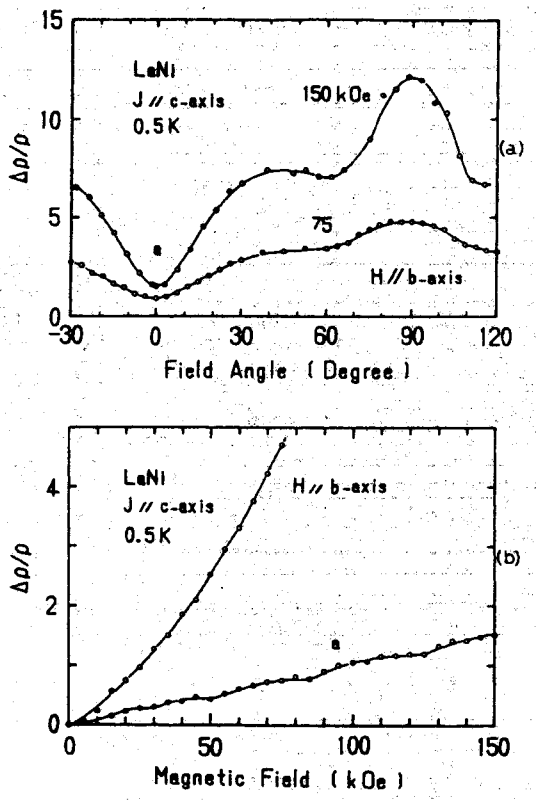

Fig. 2.32 (a) Angular and (b) field dependence of magnetoresistance in the c-plane of LaNi.[48]

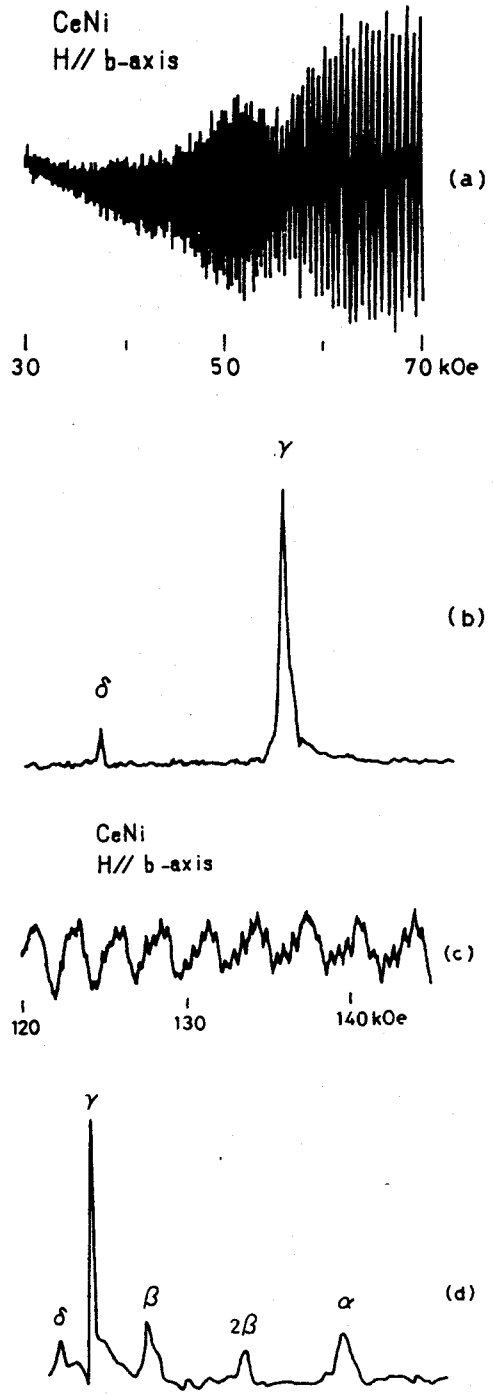

Fig. 5. de Haas-van Alphen oscillations and fast Fourier transformation spectra at 0.43 K in CeNi.

Fig. 2.33 de Haas-van Alphen oscillations and fast Fourier transformation spectra at 0.43 K in CeNi.[48)]

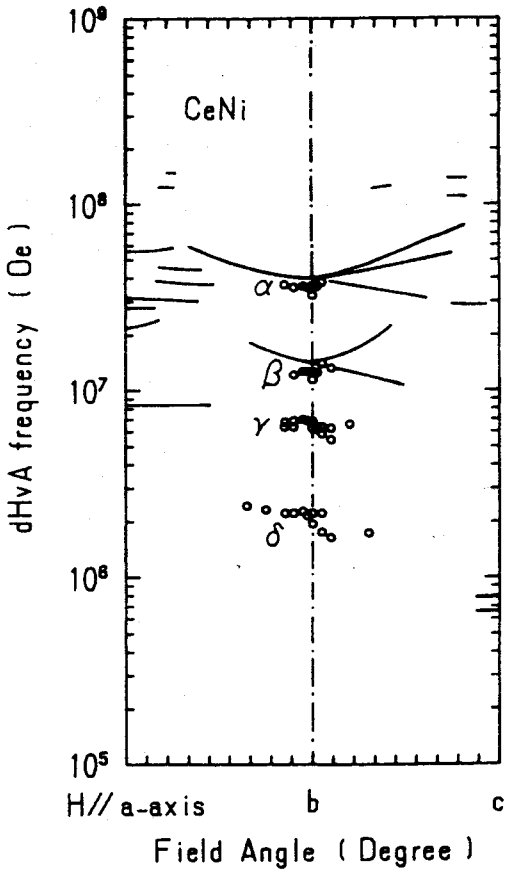

Fig. 2.34 Angular dependence of dHvA frequencies in CeNi. Solid lines show the dHvA frequencies in LaNi.[48)]

3 Experimental

3.1 Sample preparation

3.1.1 $CeRh_2Si_2$

Single crystal growth

Starting materials of $CeRh_2Si_2$ were 4N(99.99% pure)-Ce, -Rh and 5N-Si. The Ce-metal block was cut by a spark cutter or diamond cutter and etched chemically. An etching liquid for Ce is a 1:3 mixture of nitric acid and water. The Rh-powder was compressed into small plates because the powder is not suitable for arc-melting. Then, these plates were melted into pellets in an arc furnace.

The melting point of $CeRh_2Si_2$ is high, 1983 K.[49] A Czochralski (CZ) pulling method in an arc furnace is the best method for the single crystal growth of $CeRh_2Si_2$, because a Cu hearth, which corresponds to the crucible, is water-cooled one and Ce, Rh and Si are low-vapor pressure materials. The schematic view of the arc furnace is shown in Fig. 3.1. It has four torches to improve a stability of the temperature of the melted material.

Arc melting has been done under high-quality (6N) argon gas atmosphere. The melting procedure was repeated several times to ensure the sample homogeneity. The first seed crystal of $CeRh_2Si_2$ was obtained from the pellet. Therefore, the first seed was poly-crystalline. The single seed-crystal was grown by using the first seed by the CZ pulling method. If there are a few grains in a seed crystal, the obtained ingot also possesses the same grains. Therefore, the necking procedure is important. A typical necking diameter was about 1 mm, while a typical diameter of the ingot was 3–4 mm. The growth rate was 10 mm/h to avoid stacking faults in the sample. We kept this speed all over the time and did not rotate both the seed and hearth to avoid stacking faults in the sample. Figure 3.2 shows a photograph of $CeRh_2Si_2$ ingot with 50 mm in length.

Determination of the crystallographic direction of the sample

We characterized all the obtained samples by the x-ray Laue method. We show the Laue patterns for the (001), (100) and (110) planes of $CeRh_2Si_2$ in Fig. 3.3. If both ends of an ingot show the same pattern, precisely we should obtain a mirror image: the ingot is regarded as a single crystal. As a matter of fact, the tale side was usually not good, containing stacking faults.

After determining a sample direction, we cut the sample by an electrode spark cutter.

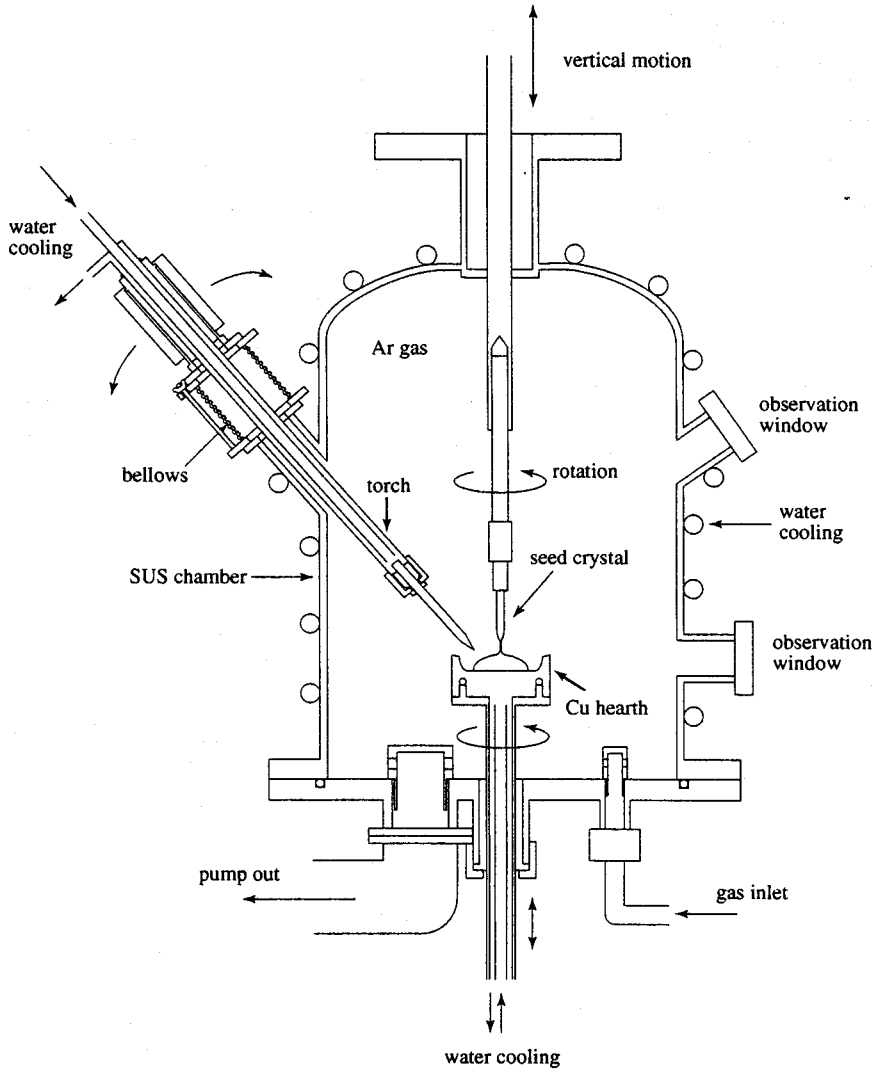

Fig. 3.1 Illustration of the tetra-arc furnace.

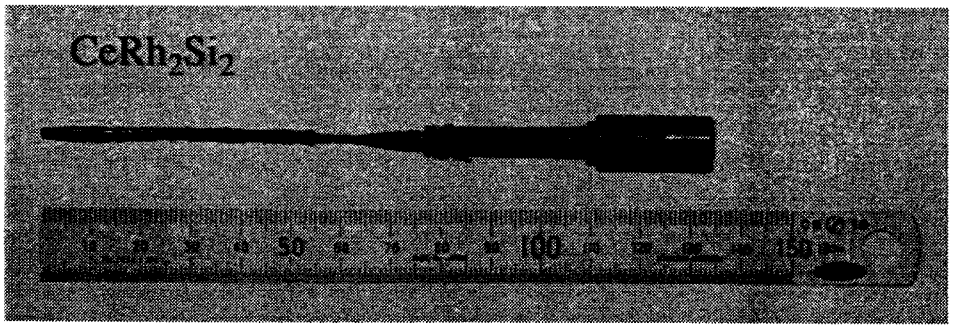

Fig. 3.2 Photograph of a $CeRh_2Si_2$ ingot.

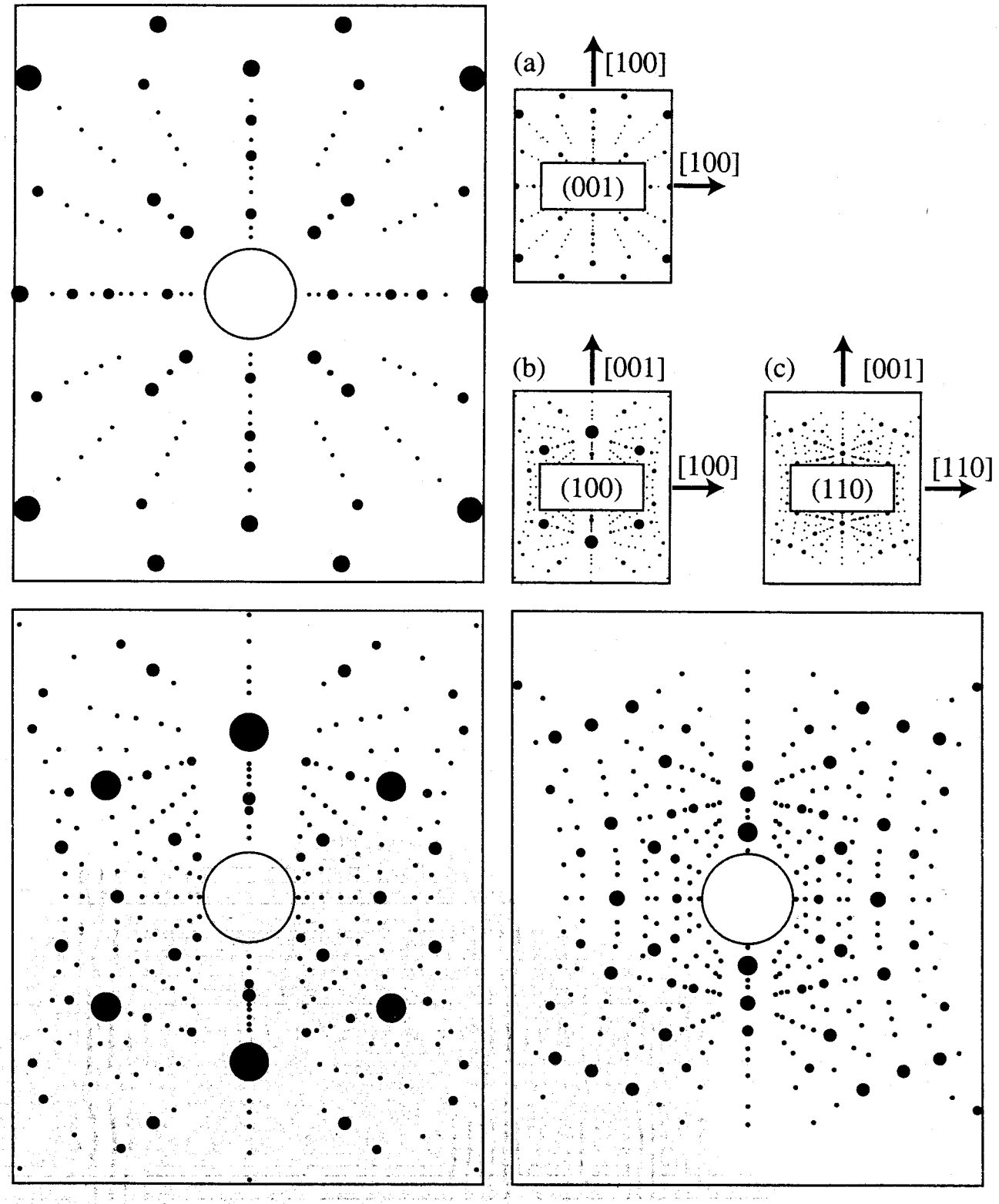

Fig. 3.3 Laue patterns for the typical planes of $CeRh_2Si_2$. (a) (001) plane, (b) (100) plane and (c) (110) plane.

3.1.2 CeNi

Single crystal growth

The starting materials of CeNi were 4N(99.99% pure)-Ce and 5N-Ni. The Ni-rod was cut by a handsaw, burnished by a grinder, and then etched chemically at about 70°C. An etching liquid for Ni is a 5:10:2 mixture of nitric acid and phosphoric acid and water. A seed crystal was obtained by an arc-melting polycrystalline CeNi metal.

The phase diagram of Ce-Ni alloys is shown in Fig. 3.4. CeNi is a congruent melting compound and the melting point is 680°C. The single crystal of CeNi was grown by the

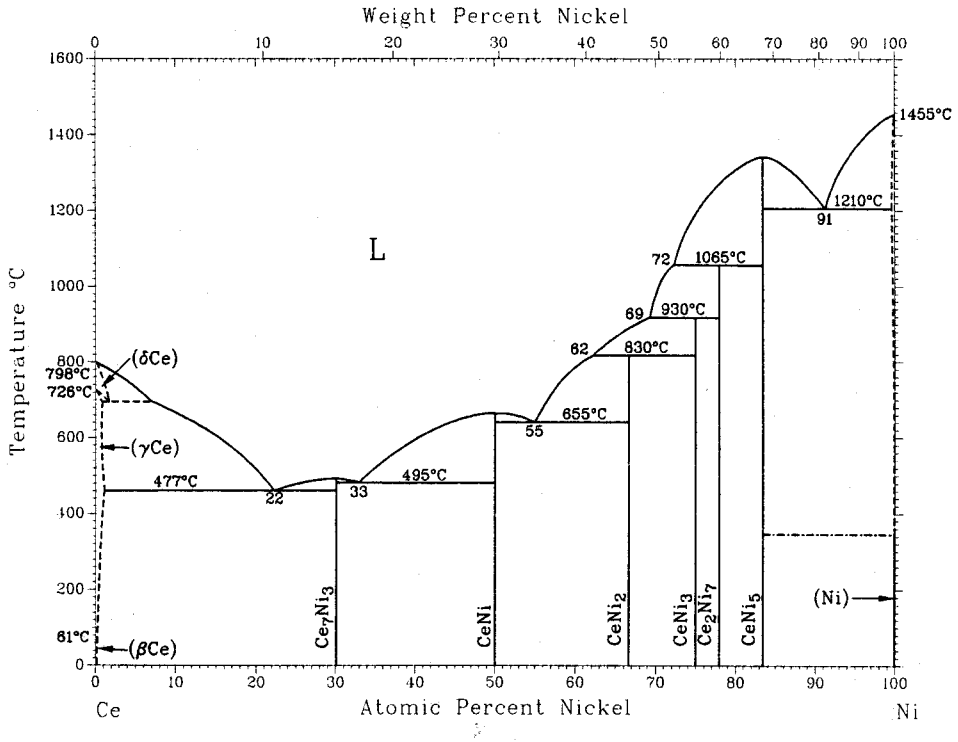

Fig. 3.4 Phase diagram of Ce-Ni alloys.

CZ pulling method in an rf furnace under He gas atmosphere. He gas was purified by a liquid nitrogen trap and the gas pressure was 3.5 kg/cm^2. Figure 3.5 shows a block diagram of the rf furnace. A tungsten crucible, which is supported by a tungsten bar standing on the stainless table, is heated by a rf-water-cooled working coil. These are surrounded with a quartz-glass thermal-insulator wall.

The tungsten crucible was heated up to the temperature slightly higher than the melting point. The Ni metal and the tungsten crucible reacts when the temperature is higher than 1000°C. Fortunately, this is no problem in the present case, because a melting

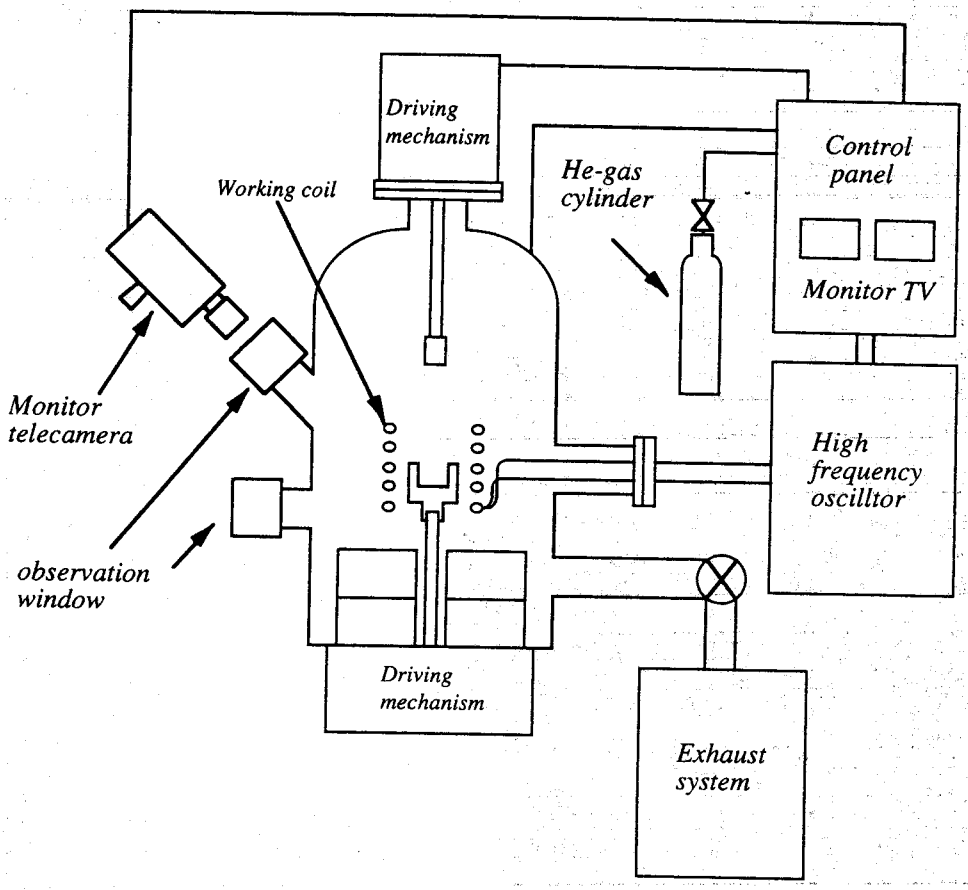

Fig. 3.5 Block diagram of the rf furnace.

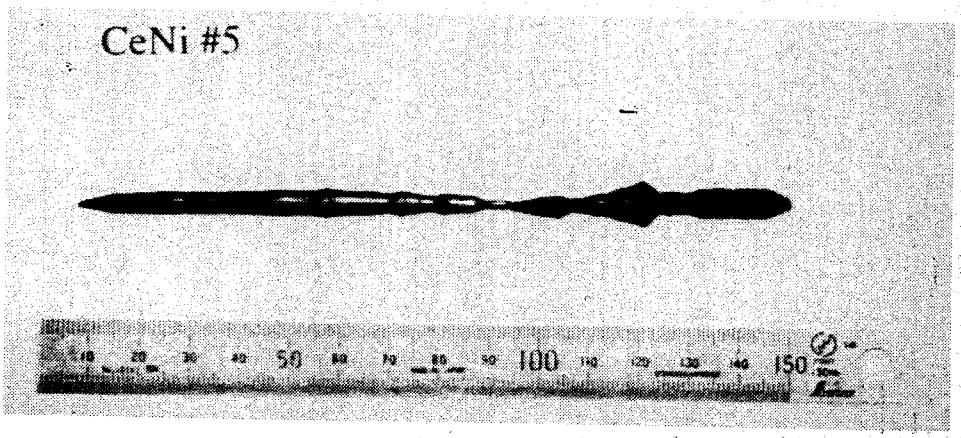

Fig. 3.6 Photograph of a CeNi ingot.

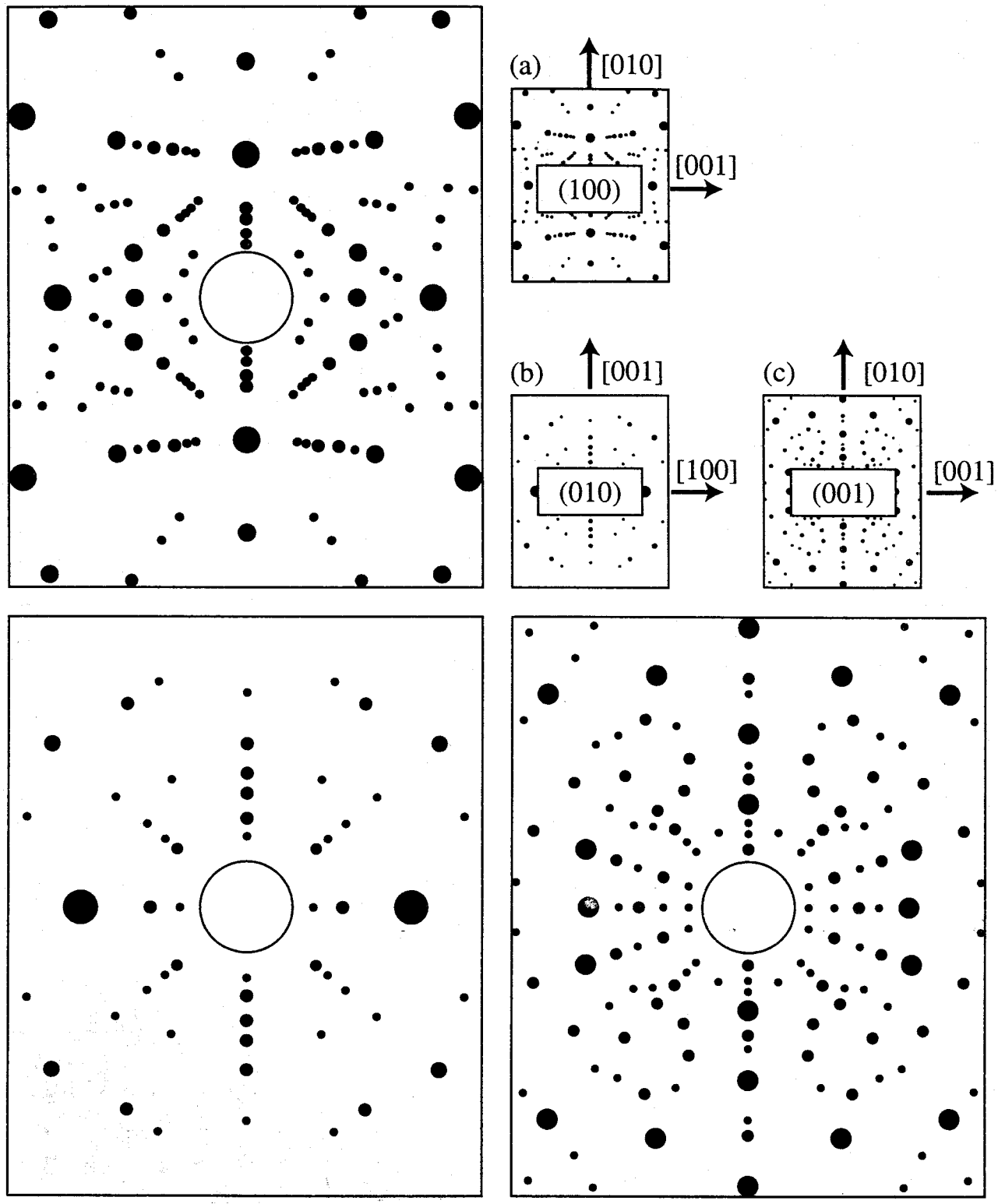

Fig. 3.7 Laue patterns for the typical planes of CeNi. (a) (100) plane, (b) (010) plane and (c) (001) plane.

point of CeNi is lower than 1000°C. After melting of the starting materials, a seed crystal was inserted into the melt and then pulled out to grow a single crystal ingot. The pulling speed was 10 mm/h with rotation of 1 rpm, while a typical diameter of the ingot was 4 mm. Figure 3.2 shows a photograph of CeNi ingot with 70 mm in length.

Determination of the crystallographic direction of the sample

We characterized all obtained samples by the x-ray Laue method. We show the Laue patterns for the (100) (a-), (010) (b-) and (001) (c-) planes of CeNi in Fig. 3.7.

After determining a sample direction, we cut the sample by an electrode spark cutter.

3.2 Experimental method

3.2.1 Electrical resistivity

Introduction to the electrical resistivity

An electrical resistivity consists of four contributions: the electron scattering due to impurities or defects ρ_0, the electron-phonon scattering $\rho_{\rm ph}$, the electron-electron scattering $\rho_{\rm e-e}$ and the electron-magnon scattering $\rho_{\rm mag}$:

$$\rho = \rho_0 + \rho_{\rm ph} + \rho_{\rm e-e} + \rho_{\rm mag}. \tag{3.1}$$

This relation is called a Matthiessen rule.

The ρ_0 value, which originates from the electron scattering due to impurities and defects, is constant for a variation of the temperature. This value is important to determine whether an obtained sample is goo or not, because if ρ_0 is large, it contains many impurities or defects. A quality of a sample can be estimated by determining a so-called residual resistivity ratio (RRR = $\rho_{\rm RT}/\rho_0$), where $\rho_{\rm RT}$ is the resistivity at room temperature. Of course, a large value of RRR indicates that the quality of the sample is good. We will introduce a scattering lifetime τ_0 and a mean free path l_0 from the residual resistivity. The residual resistivity ρ_0 can be written as

$$\rho_0 = \frac{m^*}{ne}\frac{1}{\tau_0}, \tag{3.2}$$

where n is a density of carrier and e is the electric charge. Then τ_0 and l_0 values are

$$\tau_0 = \frac{m^*}{ne\rho_0}, \tag{3.3}$$

$$l_0 = v_{\rm F}\tau_0 = \frac{\hbar k_{\rm F}}{ne\rho_0}. \tag{3.4}$$

The temperature dependence of $\rho_{\rm ph}$, which is originated from the electron scattering by phonon, is monotonously. The value of $\rho_{\rm ph}$ is proportional to T above the Debye temperature, while it is proportional to T^5 far below the Debye temperature, and $\rho_{\rm ph}$ will be zero at $T = 0$.

In the strongly correlated electron system, the contribution of $\rho_{\rm e-e}$, which can be expressed in terms of the reduction factor of the quasiparticles and the Umklapp process, is dominant at low temperatures. Therefore, we can regard the total resistivity in the non-magnetic compounds at low temperatures as follows:

$$\begin{aligned} \rho(T) &= \rho_0 + \rho_{\rm e-e}(T) \\ &= \rho_0 + AT^2, \end{aligned} \tag{3.5}$$

where the coefficient $\sqrt{A}$ is proportional to the effective mass. Yamada and Yosida obtained the rigorous expression of $\rho_{\rm e-e}$ in the strongly correlated electron system on the basis of the Fermi liquid theory.[12] According to their theory, $\rho_{\rm e-e}$ is proportional to the imaginary part of the f-electron self-energy Δk. This Δk is proportional to the square of the enhancement factor and gives a large T^2-resistivity to the heavy fermion system.

In a magnetic compound, an additional contribution to the resistivity must be taken into consideration, namely $\rho_{\rm mag}$. This contribution describes scattering processes of conduction electrons due to disorder in the arrangement of the magnetic moments. In general, above the ordering temperature $T_{\rm ord}$, $\rho_{\rm mag}$ is given by

$$\rho_{\rm mag} = \frac{3\pi N m^*}{2\hbar e^2 E_{\rm F}} |J_{cf}|^2 (g_J - 1)^2 J(J+1). \tag{3.6}$$

When $T = T_{\rm ord}$, $\rho_{\rm mag}$ shows a pronounced kink, and when $T < T_{\rm ord}$, $\rho_{\rm mag}$ strongly decreases with decreasing temperature. The magnetic resistivities in the lanthanides, however, are ascribed to strong scattering of the conduction electrons by the spin fluctuations of $4f$ electrons. This contribution to the resistivity at low temperatures is given by the square of the temperature, namely $\rho_{\rm mag} = A'T^2$. In the heavy fermion system, the coefficient A' is extremely large. Therefore $\rho_{\rm mag}$ and $\rho_{\rm e-e}$ are inseparable and $\rho_{\rm mag}$ can be replaced by $\rho_{\rm e-e}$. An analogous situation occurs to the specific heat. Namely, in the heavy fermion system, the magnetic specific heat $C_{\rm mag}$ is changed into a large electronic one γT.

Experimental method of the electrical resistivity

We have done the resistivity measurement using a standard four probe dc current method. The sample is fixed on a plastic plate by a GE7031 varnish. The gold wire with

0.025 mm in diameter and silver paste were used to form contacts on the sample. The sample was mounted on a sample-holder and installed in a ^{4}He cryostat. We measured the resistivity from 1.3 K to the room temperature. The thermometers are a RuO_2 registor at lower temperature (below 20 K) and a Au-Fe-Ag thermocouple at higher temperatures.

3.2.2 Specific heat

Introduction to the specific heat

At low temperatures, the specific heat is written as the sum of electronic, lattice and magnetic contributions:

$$C = C_{\rm e} + C_{\rm ph} + C_{\rm mag} \tag{3.7}$$
$$= \gamma T + \beta T^3 + C_{\rm mag}, \tag{3.8}$$

where γ and β are constants characteristic of the material. Here we neglect the nuclear contribution.

The electronic term is linear in T and is dominant at sufficiently low temperatures. If we can neglect the magnetic contributions, it is convenient to exhibit the experimental values of C as a plot of C/T versus T^2:

$$\frac{C}{T} = \gamma + \beta T^2. \tag{3.9}$$

Then we can estimate the electronic specific coefficient γ. Using the density of states, the coefficient γ can be expressed as

$$\gamma = \frac{\pi^2}{3} {k_{\rm B}}^2 D(E_{\rm F}). \tag{3.10}$$

Since the density of states based on the free electron model is proportional to the electron mass, the coefficient γ possesses an extremely large value in the heavy fermion system.

According to the Debye T^3 law, for $T \ll \Theta_{\rm D}$

$$C_{\rm ph} \simeq \frac{12\pi^4 N k_{\rm B}}{5} \left(\frac{T}{\Theta_{\rm D}}\right)^3 \equiv \beta T^3, \tag{3.11}$$

where $\Theta_{\rm D}$ is the Debye temperature, N is the number of atoms. For the actual lattices the temperatures at which the T^3 approximation holds are quite low. It may be necessary to be below $T = \Theta_{\rm D}/50$ to get a reasonably pure T^3 law.

If the f-energy level splits due to the crystalline electric field (CEF) in the paramagnetic state, the inner energy per one magnetic ion is given by

$$E_{\rm CEF} = \langle E_i \rangle = \frac{\sum_i n_i E_i \exp(-E_i/k_{\rm B}T)}{\sum_i \exp(-E_i/k_{\rm B}T)}, \tag{3.12}$$

where E_i and n_i are the energy and the degenerate degree on the level i, respectively. The magnetic contribution to the specific heat is given by

$$C_{\rm sch} = \frac{\partial E_{\rm CEF}}{\partial T}. \tag{3.13}$$

This contribution is called a Schottky term. Here, the entropy of the f electron S is defined as

$$S = \int_0^T \frac{C_{\rm sch}}{T} {\rm d}T. \tag{3.14}$$

The entropy is also described as

$$S = R \ln W, \tag{3.15}$$

where W is a state number at temperature T. Therefore it acquires information about the CEF level.

In the magnetic ordering state $C_{\rm mag}$ is

$$C_{\rm mag} \propto T^{3/2} \quad \text{(ferromagnetic ordering)} \tag{3.16}$$

$$\propto T^3 \quad \text{(antiferromagnetic ordering)}. \tag{3.17}$$

Experimental method of the specific heat

The specific heat was measured by the quasi-adiabatic heat-pulse method using a ^{4}He cryostat at temperatures down to 1.5 K. The sample was put on the Cu-addenda. We measured the temperature of a sample with constant heating, and the specific heat is deduced as follows:

$$C = \frac{\Delta Q}{\Delta T} = \frac{IV\Delta t}{\Delta T}. \tag{3.18}$$

Here, ΔQ is the amount of heat, I and V are the current and the voltage flowing to the heater, respectively, Δt is the duration of heating and ΔT is the change of temperature due to heating. The temperature was measured by the RuO_2 resistor at the addenda. The specific heat of the sample is derived by subtracting the specific heat of the addenda measured.

3.2.3 Thermal expansion coefficient

Introduction to the thermal expansion coefficient

The thermal expansion coefficient α is closely related to the specific heat as follows:

$$\alpha = \frac{\Gamma}{3B_T V} C, \tag{3.19}$$

where Γ is a Grüneisen parameter, B_T is bulk modulus and V is volume. From eq. (3.7), α is expressed as in the specific heat:

$$\alpha = \alpha_{\rm e} + \alpha_{\rm ph} + \alpha_{\rm mag}. \tag{3.20}$$

Experimental method of the thermal expansion coefficient

The thermal expansion coefficient were measured by a capacitance method. For an ideal plate capacitor with area A and distance d, the capacitance is expressed as follows:

$$C = \varepsilon_r \varepsilon_0 \frac{A}{d}, \tag{3.21}$$

where $\varepsilon_0 = 8.854 \times 10^{-12}$ Fm^{-1} and ε_r is the dielectric constant of the medium. Here ε_r can be regarded as equal to 1. In the case of circular plates with radius r, the distance between the capacitor plates is

$$d = \varepsilon_0 \frac{\pi r^2}{C}. \tag{3.22}$$

Therefore a change in the distance of the plates is

$$\Delta d \equiv d_2 - d_1 = -\varepsilon_0 \pi r^2 \frac{C_2 - C_1}{C_2 C_1}. \tag{3.23}$$

Since the Δd is equal to the length change $\Delta \ell$ of the sample, $\Delta \ell$ can be determined by measuring the capacitance of the cell.

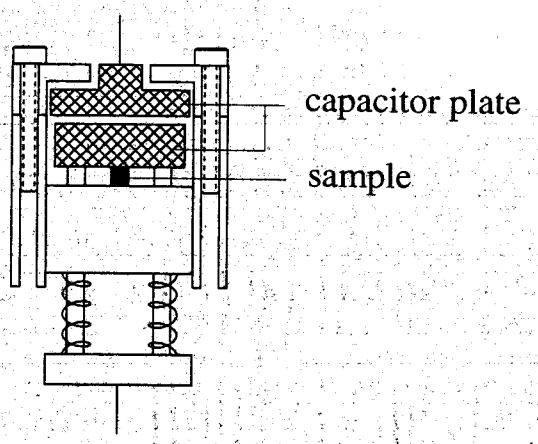

Fig. 3.8 Schematic view of the capacitance cell.

3.2.4 de Haas-van Alphen effect

Introduction to the de Haas-van Alphen effect

Under a strong magnetic field, the orbital motion of the conduction electron is quantized and forms Landau levels.[50] Therefore various physical qualities shows a periodic variation with H^{-1} since increasing the field strength H causes a sharp change in the free energy of the electron system when Landaus level cross the Fermi energy. In a three-dimensional system this sharp structure is observed at extremal areas in $\boldsymbol{k}$-space, perpendicular to the field direction and enclosed by the Fermi energy because the density of state also becomes extremal. From the field and temperature dependence of various physical quantities, we can obtain the extremal area S, the cyclotron mass m_{c}^* and the scattering lifetime τ for this cyclotron orbit. The magnetization or the magnetic susceptibility is the most common one of these physical quantities, and its periodic character is called the de Haas-van Alphen (dHvA) effect. It provides one of the best tools for the investigation of Fermi surfaces of metals.

The theoretical expression for the oscillatory component of magnetization M_{osc} due to the conduction electrons was given by Lifshitz and Kosevich as follows:

$$M_{\mathrm{osc}} = \sum_r \sum_i \frac{(-1)^r}{r^{3/2}} A_i \sin\left(\frac{2\pi r F_i}{H} + \beta_i\right), \tag{3.24a}$$

$$A_i \propto F H^{1/2} \left|\frac{\partial^2 S_i}{\partial {k_{\mathrm{H}}}^2}\right|^{-1/2} R_{\mathrm{T}} R_{\mathrm{D}} R_{\mathrm{S}}, \tag{3.24b}$$

$$R_{\mathrm{T}} = \frac{\alpha r m_{ci}^* T/H}{\sinh(\alpha r m_{ci}^* T/H)}, \tag{3.24c}$$

$$R_{\mathrm{D}} = \exp(-\alpha r m_{ci}^* T_{\mathrm{D}}/H), \tag{3.24d}$$

$$R_{\mathrm{S}} = \cos(\pi g_i r m_{ci}^*/2m_0), \tag{3.24e}$$

$$\alpha = \frac{2\pi^2 k_{\mathrm{B}}}{e\hbar}. \tag{3.24f}$$

Here the magnetization is periodic on $1/H$ and has a dHvA frequency F_i

$$\begin{aligned} F_i &= \frac{\hbar}{2\pi e} S_i \\ &= 1.05 \times 10^{-12}\ [\mathrm{T \cdot cm^2}] \cdot S_i, \end{aligned} \tag{3.25}$$

which is directly proportional to the i-th extremal (maximum or minimum) cross-sectional area S_i $(i = 1, \ldots, n)$. The extremal area means a gray plane in Fig. 3.9, where there is one extremal area in a spherical Fermi surface. The factor R_{T} in the amplitude A_i is related to the thermal damping at a finite temperature T. The factor R_{D} is also related to the Landau level broadening $k_{\mathrm{B}}T_{\mathrm{D}}$. Here T_{D} is due to both the lifetime broadening

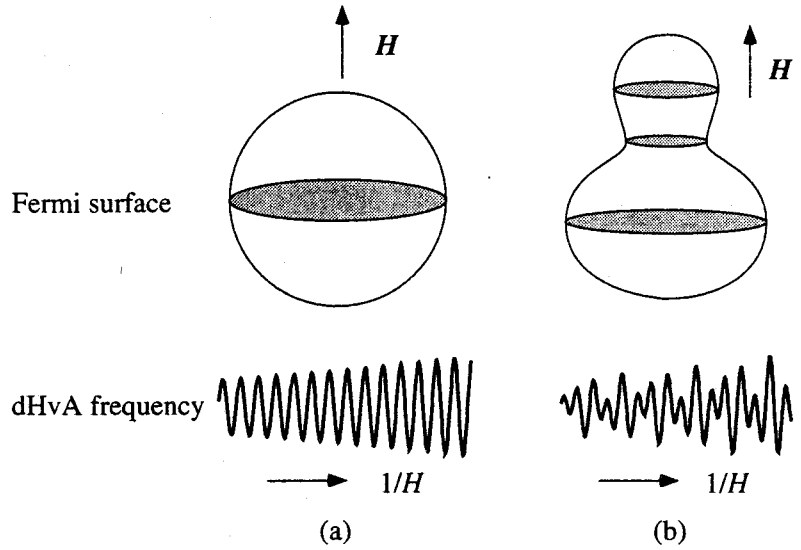

Fig. 3.9 Simulations of the cross-sectional area and its dHvA signal for a simple Fermi surface. There is one dHvA frequency in (a), while there are three different frequencies in (b).

and inhomogeneous broadening caused by impurities, crystalline imperfections or strains. The factor T_{D} is called the Dingle temperature and is given by

$$\begin{aligned} T_{\mathrm{D}} &= \frac{\hbar}{2\pi k_{\mathrm{B}}}\tau^{-1} \\ &= 1.22 \times 10^{-12}\ [\mathrm{K}\cdot\mathrm{sec}]\cdot\tau^{-1}. \end{aligned} \tag{3.26}$$

The factor R_{S} is called the spin factor and related to the difference of phase between the Landau levels due to the Zeeman split. When $g_i = 2$ (a free electron value) and $m_{\mathrm{c}}^* = 0.5m_0$, this term becomes zero for $r = 1$. The fundamental oscillation vanishes for all values of the field. This is called the zero spin splitting situation in which the up and down spin contributions to the oscillation cancelled out, and this can be useful for determining the value of g_i. Note that in this second harmonics for $r = 2$ the dHvA oscillation should show a full amplitude. The quantity $|\partial^2 S/\partial {k_{\mathrm{H}}}^2|^{-1/2}$ is called the curvature factor. The rapid change of cross-sectional area around the extremal area along the field direction diminishes the dHvA amplitude for this extremal area.

The detectable conditions of dHvA effect are as follows:

1) The distance between the Landau levels $\hbar\omega_{\mathrm{c}}$ must be larger than the thermal broadening width $k_{\mathrm{B}}T$: $\hbar\omega_{\mathrm{c}} \ll k_{\mathrm{B}}T$ (high fields, low temperatures).

2) At least one cyclotron motion must be performed during the scattering, namely $\omega_c\tau/2\pi > 1$ (high quality samples). In reality, however, it can be observed even if a cyclotron motion is about ten percent of one cycle.

3) The fluctuation of the static magnetic field must be smaller than the field interval of one cycle of the dHvA oscillation (homogeneity of the magnetic field).

Shape of the Fermi surface

The angular dependence of dHvA frequencies gives very important information about a shape of the Fermi surface. As a value of Fermi surface corresponds to a carrier number, we can obtain the carrier number of a metal directly.

We show the typical Fermi surfaces and their angular dependences of dHvA frequencies in Fig. 3.10. In a spherical Fermi surface, the dHvA frequency is constant for any field direction. On the other hand, in a ellipsoidal Fermi surface such as in Fig. 3.10(b), it takes a minimum value for the field along the z-axis. These relatively simple shape Fermi

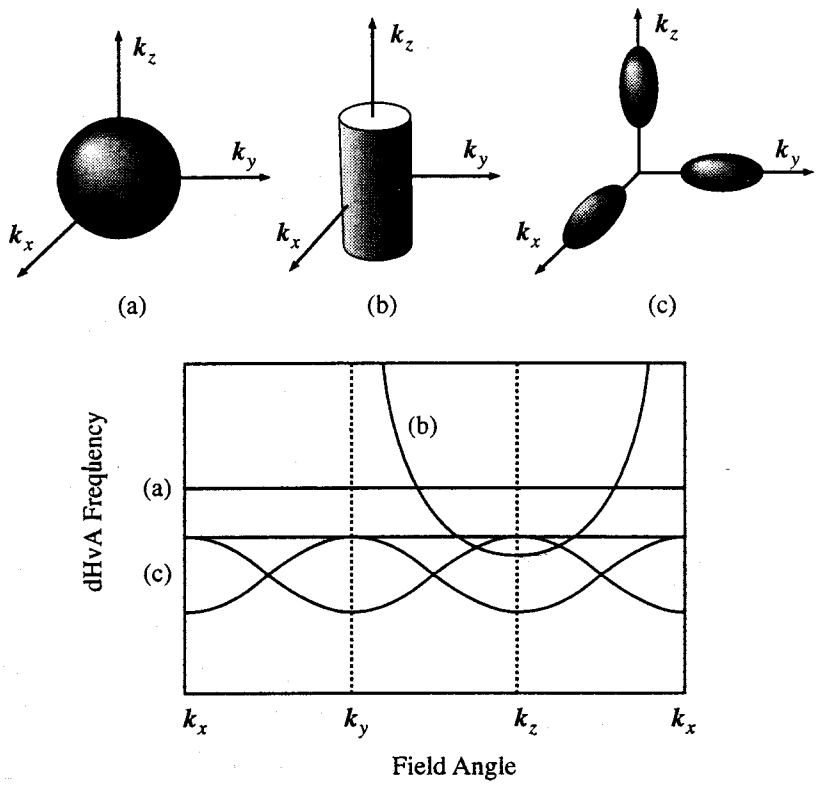

Fig. 3.10 Angular dependence of the dHvA frequency in three typical Fermi surfaces (a) sphere, (b) cylinder and (c) ellipsoid.

surfaces can be determined only by the experiment. However, information from an energy band calculation is needed to determine a complicated one.

Cyclotron effective mass

We can determine the cyclotron effective mass m^*_{ci} from the measuring a temperature dependence of a dHvA amplitude. Equation (3.24c) is transformed into

$$\ln\left\{A_i\left[1-\exp\left(\frac{-2\alpha m^*_{ci}T}{H}\right)\right]/T\right\}=\frac{-\alpha m^*_{ci}}{H}T+\text{const.} \tag{3.27}$$

Therefore, from the slope of a plot of $\ln\{A_i[1-\exp(-2\lambda m^*_{ci}T/H)]/T\}$ versus T at constant field H, the effective mass can be obtained.

Let us consider the relation between the cyclotron mass and the electrical specific heat γ. Using a density of states $D(E_\mathrm{F})$, γ is written as

$$\gamma=\frac{\pi^2}{3}{k_\mathrm{B}}^2D(E_\mathrm{F}). \tag{3.28}$$

In the spherical Fermi surface, using $E_\mathrm{F}=\hbar^2{k_\mathrm{F}}^2/2m^*_\mathrm{c}$ takes

$$\begin{aligned}\gamma&=\frac{\pi^2}{3}{k_\mathrm{B}}^2\frac{V}{2\pi^2}\left(\frac{2m^*_\mathrm{c}}{\hbar^2}\right)^{3/2}{E_\mathrm{F}}^{1/2}\\&=\frac{{k_\mathrm{B}}^2V}{3\hbar^2}m^*_\mathrm{c}k_\mathrm{F},\end{aligned} \tag{3.29}$$

where V is molar volume and $k_\mathrm{F}=(S_\mathrm{F}/\pi)^{1/2}$. We obtain from eq. (3.25)

$$\begin{aligned}\gamma&=\frac{{k_\mathrm{B}}^2m_0}{3\hbar^2}\left(\frac{2e}{\hbar}\right)^{1/2}V\frac{m^*_\mathrm{c}}{m_0}F^{1/2}\\&=2.87\times10^{-4}\,[(\mathrm{mJ/K^2\cdot mol})(\mathrm{mol/cm^3})\mathrm{T}^{-1/2}]\cdot V\frac{m^*_\mathrm{c}}{m_0}F^{1/2}.\end{aligned} \tag{3.30}$$

In the case of the cylindrical Fermi surface,

$$\begin{aligned}\gamma&=\frac{\pi^2}{3}{k_\mathrm{B}}^2\frac{V}{2\pi^2\hbar^2}m^*_\mathrm{c}k_z\\&=\frac{{k_\mathrm{B}}^2V}{6\hbar^2}m^*_\mathrm{c}k_z,\end{aligned} \tag{3.31}$$

where the Fermi wave number k_z is parallel to an axial direction of the cylinder. If we regard simply the Fermi surfaces as sphere, ellipse or cylinder approximately and then can calculate them.

Dingle temperature

We can determine the Dingle temperature T_D from measuring a field dependence of a dHvA amplitude. Equations (3.24b)-(3.24d) yield

$$\ln\left\{A_i H^{1/2}\left[1-\exp\left(\frac{-2\lambda m_{ci}^* T}{H}\right)\right]\right\} = -\lambda m_{ci}^*(T+T_D)\frac{1}{H} + \text{const.} \tag{3.32}$$

From the slope of a plot of $\ln\{A_i H^{1/2}[1-\exp(-2\lambda m_{ci}^* T/H)]\}$ versus $1/H$ at constant T, the Dingle temperature can be obtained. Here, the cyclotron effective mass must have been already obtained.

We can estimate the mean free path l or the scattering life time τ from the Dingle temperature. The relation between an effective mass and life time takes the form

$$\hbar k_F = m^* v_F, \tag{3.33}$$

$$l = v_F \tau. \tag{3.34}$$

Then eq. (3.26) is transformed into

$$l = \frac{\hbar^2 k_F}{2\pi k_B m_c^* T_D}. \tag{3.35}$$

When the extremal area can be regarded as a circle approximately, using the eq. (3.25), the mean free path is expressed as

$$\begin{aligned} l &= \frac{\hbar^2}{2\pi k_B m_0}\left(\frac{2e}{\hbar c}\right)^{1/2} F^{1/2}\left(\frac{m_c^*}{m_0}\right)^{-1} {T_D}^{-1} \\ &= 77.6\ [\text{Å}\cdot \text{T}^{-1/2}\cdot \text{K}]\cdot F^{1/2}\left(\frac{m_c^*}{m_0}\right)^{-1} {T_D}^{-1}. \end{aligned} \tag{3.36}$$

Field modulation method

Experiments of the dHvA effect were constructed by using the usual ac-susceptibility field modulation method. Now we give an outline of the field modulation method in the present study.

A small ac-field $h_0 \cos\omega t$ is varied on an external field H_0 ($H_0 \gg h_0$) in order to obtain the periodic variation of the magnetic moment M. The sample is set up into a pair of balanced coils (pick up and compensation coils), as shown in Fig. 3.11. An induced emf

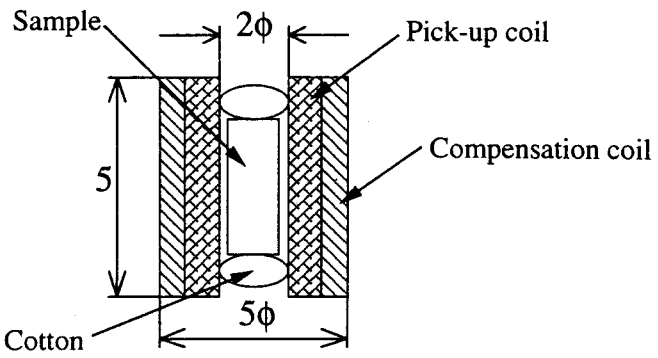

Fig. 3.11 Detecting coil and the sample location.

V will be proportional to $\mathrm{d}M/\mathrm{d}t$:

$$\begin{aligned} V &= c\frac{\mathrm{d}M}{\mathrm{d}t} \\ &= c\frac{\mathrm{d}M}{\mathrm{d}H}\frac{\mathrm{d}H}{\mathrm{d}t} \\ &= -ch_0\omega \sin\omega t \sum_{k=1}^{\infty} \frac{h_0^k}{2^{k-1}(k-1)!}\left(\frac{\mathrm{d}^k M}{\mathrm{d}H^k}\right)_{H_0} \sin k\omega t, \end{aligned} \tag{3.37}$$

where c is constant which is fixed by the number of turns in the coil and so on, and the higher differential terms of the coefficient of $\sin k\omega t$ are neglected. Calculating the

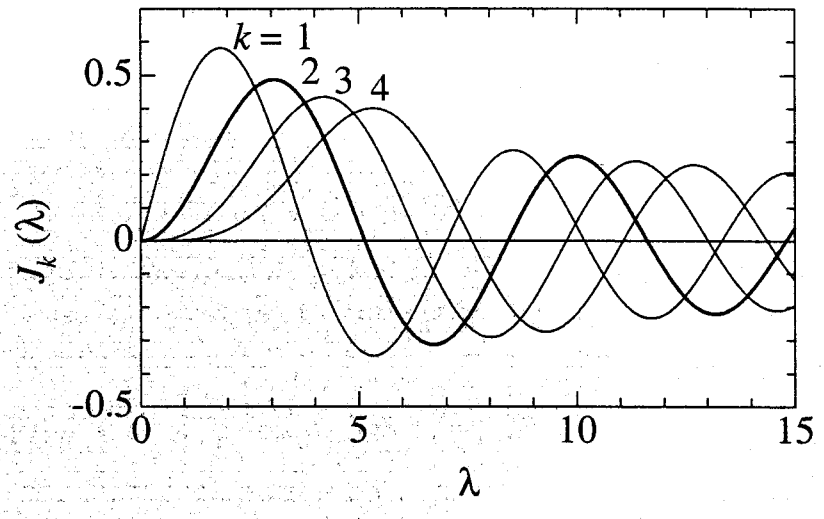

Fig. 3.12 Bessel function $J_k(\lambda)$ of the first kind.

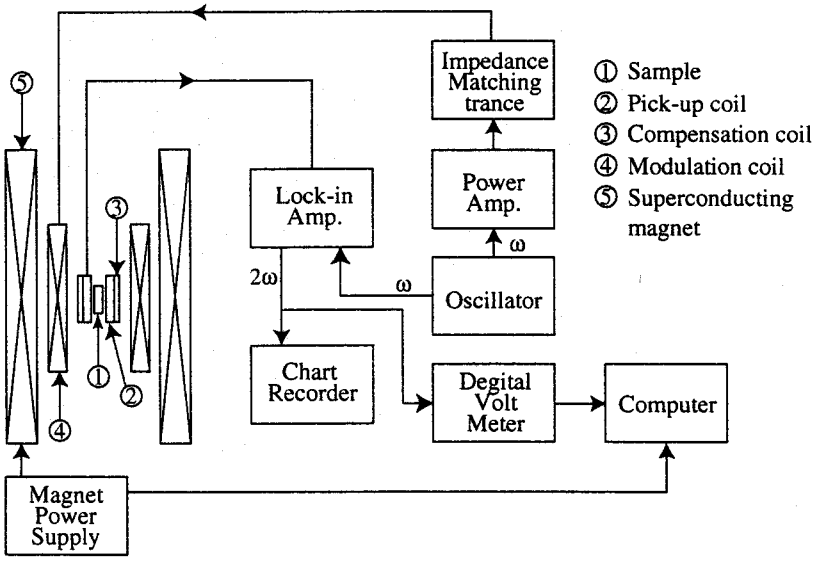

Fig. 3.13 Block diagram for the dHvA measurement.

$\mathrm{d}^k M/\mathrm{d}H^k$ it becomes

$$V = -c\omega A \sum_{k=1}^{\infty} \frac{1}{2^{k-1}(k-1)!} \left(\frac{2\pi h_0}{\Delta H}\right)^k \sin\left(\frac{2\pi F}{H} + \beta - \frac{k\pi}{2}\right) \sin k\omega t. \tag{3.38}$$

Here, $\Delta H = H^2/F$. Considering ${h_0}^2 \ll {H_0}^2$ the time dependence of magnetization $M(t)$ is given by

$$M(t) = A\left[J_0(\lambda)\sin\left(\frac{2\pi F}{H_0} + \beta\right) + 2\sum_{k=1}^{\infty} kJ_k(\lambda)\cos k\omega t \sin\left(\frac{2\pi F}{H_0} + \beta - \frac{k\pi}{2}\right)\right], \tag{3.39}$$

where

$$\lambda = \frac{2\pi F h_0}{{H_0}^2}. \tag{3.40}$$

Here, J_k is k-th Bessel function. Figure 3.12 shows the Bessel function of the first kind for the various order k. Finally we can obtain the output emf as follows:

$$V = c\left(\frac{\mathrm{d}M}{\mathrm{d}t}\right) = -2c\omega A \sum_{k=1}^{\infty} kJ_k(\lambda)\sin\left(\frac{2\pi F}{H_0} + \beta - \frac{k\pi}{2}\right)\sin k\omega t. \tag{3.41}$$

The signal was detected at the second harmonic of the modulation frequency 2ω using a Lock-in Amplifier, since this condition may cut off the offset magnetization and then

detect the component of the quantum oscillation only. We usually choose the modulation field h_0 to make the value of $J_2(\lambda)$ maximum, namely $\lambda = 3.1$. We used modulation frequency of 75 Hz for ^{3}He cryostat or 12 Hz for dilution refrigerator, respectively. Figure 3.13 shows a block diagram for the dHvA measurement in the present study.

3.2.5 Pressure cell

Construction of the pressure cell

The electrical resistivity and the dHvA experiments under pressure were performed with a conventional Be-Cu piston-cylinder clamping type pressure cell as shown in Fig. 3.14. Most part of the pressure cell is made of Be-Cu and piston is made of tungsten carbide (WC). Electrical leads were introduced into the sample region through the hole (0.6 mmϕ) of obturator. Then, the hole was sealed by Stycast 2850FT epoxy. The anti-extrusion ring are used to prevent extrusion of Teflon into the clearance between piston or obturator, and cylinder under pressure.

We used a 1:1 mixture of Daphne7373 and kerosine as a pressure transmitting medium.[51]

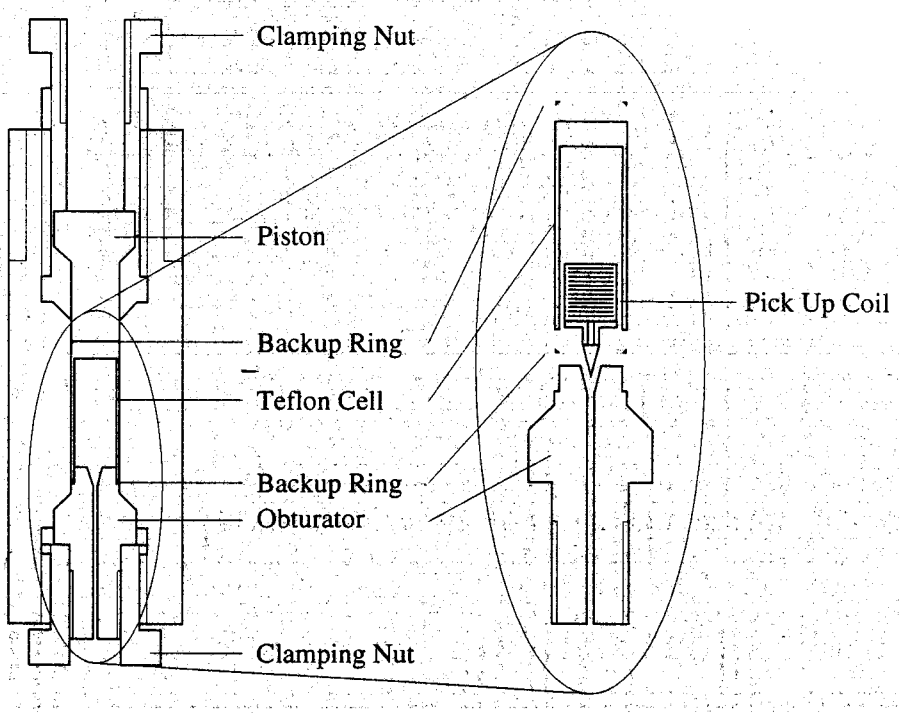

Fig. 3.14 Cross-sectional view of the pressure cell.

Pressure calibration

The pressure at room temperature was determined by the resistance of the manganin gauge, which was measured by a standard four probe dc current method. When the pressure was increased by an oil press, the pressure inside was monitored with the manganin resistance.

The pressure at liq. He temperature was determined by the superconducting transition temperature of Sn, using a relation:

$$T_c = T_c(0) - 4.95 \times 10^{-5} P + 3.9 \times 10^{-10} P^2, \tag{3.42}$$

where T_c is in K and P in atoms.[52] In this study, the transition temperature was measured by the ac-susceptibility method. Figure 3.15 shows the superconducting transition of Sn at various pressure. The transition width is almost the same in the whole pressure, indicating that the pressure distribution is small. The pressure at low temperatures was estimated experimentally from the pressure at room temperature as shown in Fig. 3.16.

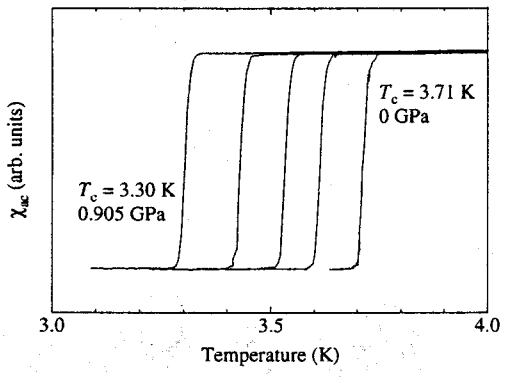

Fig. 3.15 Ac-susceptibility χ_{ac} in Sn at ambient pressure and under pressures.

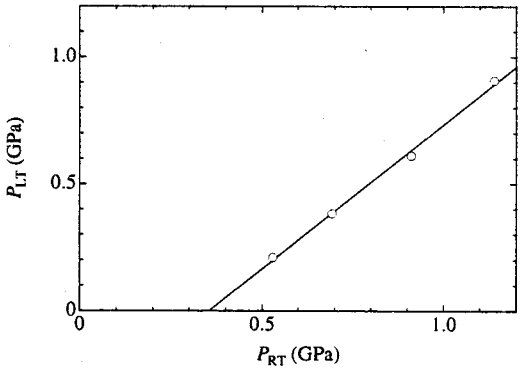

Fig. 3.16 Relation between the pressure at liq. He temperature P_{LT} and the applied pressure at room temperature P_{RT}.

dHvA measurement under pressure

Experiments of the dHvA effect under pressure were constructed by using the usual ac-susceptibility field modulation method. To increase sensitivity of a weak dHvA signal, some improvement were carried out in the present study.

The signal voltage is proportional to the number of turns of a pick up coil, so that it is better to increase the turn number. We wound a pick up coil with 20 $\mu m\phi$ copper

wire. The length of coil is 5 mm and outside dimension is 4.5 mmϕ. The number of turns of pick up part is 3100 and that of compensation part is about 1700.

The hydrostatic pressure is desirable, because the strain of a sample due to the pressure distribution causes the reduction of the oscillation. According to Takashita's trial,[51] we choose the pressure transmitting medium as a 1:1 mixture of Daphne7373 and kerosine. The pressure cell were slowly cooled down, taking 8 hour from room temperature to liq. He temperature, because the fast cooling may cause the pressure distribution.

The temperature outside of the pressure cell was measured with a RuO_2 thermometer. In the measurement using field modulation method, the pressure cell is heated up and the temperature difference between inside and outside become an inevitable problem. This causes a considerable error in determining the cyclotron effective mass, particularly in the case of heavy mass. We measured the temperature both inside and outside of pressure cell with the RuO_2 thermometer as a function of modulation frequency and amplitude. In the dHvA measurements, the temperature of a sample was calculated from the temperature outside. The typical value of modulation frequency and amplitude is 5 Hz and 100 Oe, respectively. We confirmed that the effective mass determined in CeNi without a pressure cell at ambient pressure is good agreement with that in the experiment with the pressure cell.

4 Experimental Results and Discussion

4.1 $CeRh_2Si_2$

4.1.1 Electrical resistivity

at ambient pressure

Figure 4.1 shows the temperature dependence of the electrical resistivity in $CeRh_2Si_2$. Anisotropy of the electrical resistivity is similar to that in $CeRu_2Si_2$.[25] We note here that the subtracted resistivity $\rho_{mag} = \rho(CeRh_2Si_2) - \rho(LaRh_2Si_2)$ possesses a broad maximum around 200 K, which corresponds to the combined effect of the crystalline electric field (CEF) and the Kondo effect. The residual resistivity ρ_0 and the residual resistivity ratio ρ_{RT}/ρ_0 (=RRR) are 1.3 $\mu\Omega$·cm and 90 for the current along the [100] direction, 0.6 $\mu\Omega$·cm and 110 for the [001] direction, respectively. These values of RRR are highest ones, and the measurement of the de Haas-van Alphen (dHvA) effects were performed for these high-quality samples. The resistivity decreases steeply below the Néel temperature of $T_{N1} = 36$ K. We cannot find any anomaly around T_{N2} in Fig. 4.1, although poor-quality (RRR$\simeq$30) samples show anomaly at T_{N2}. In the low temperature region, the resistivity

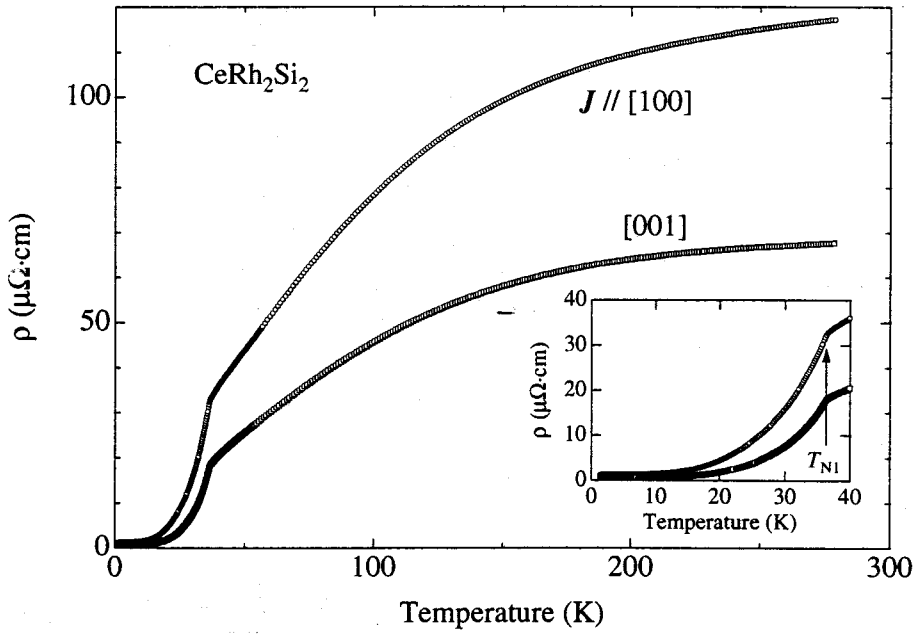

Fig. 4.1 Temperature dependence of the electrical resistivity in $CeRh_2Si_2$.

follows the AT^2 behaviour below 8 K. The A value is 2.1×10^{-3} $\mu\Omega$·cm·K^{-2} for the current along the [100] direction, and 6.2×10^{-4} $\mu\Omega$·cm·K^{-2} for the [001] direction.

under high pressure

The electrical resistivity measurements under pressure was performed for several samples (single crystals and polycrystals) and using different pressure generating system.

First, we show the results for a high-quality single crystalline sample (RRR=110), where pressure was applied by utilizing a CuBe piston-cylinder cell. Figure 4.2 shows the temperature dependence of the electrical resistivity at ambient pressure (0 GPa) and at 1.1 GPa for the current along the [001] direction. There is no trace of T_{N1} for pressure of 1.1 GPa. The resistivity at 1.1 GPa shows the AT^2 behavior with $A = 1.5 \times 10^{-2}$ $\mu\Omega$·cm·K^{-2}. The effective mass is about 5 times enhanced from those at ambient pressure, as $\sqrt{A}$ is proportional to the effective mass. The resistivity decreases steeply below 380 mK and becomes almost zero at 100 mK, as shown in Fig. 4.3. We define here the transition temperature of superconductivity T_c as an onset of the resistivity drop, because the width of the transition is wide. The onset temperature of T_c = 380 mK is

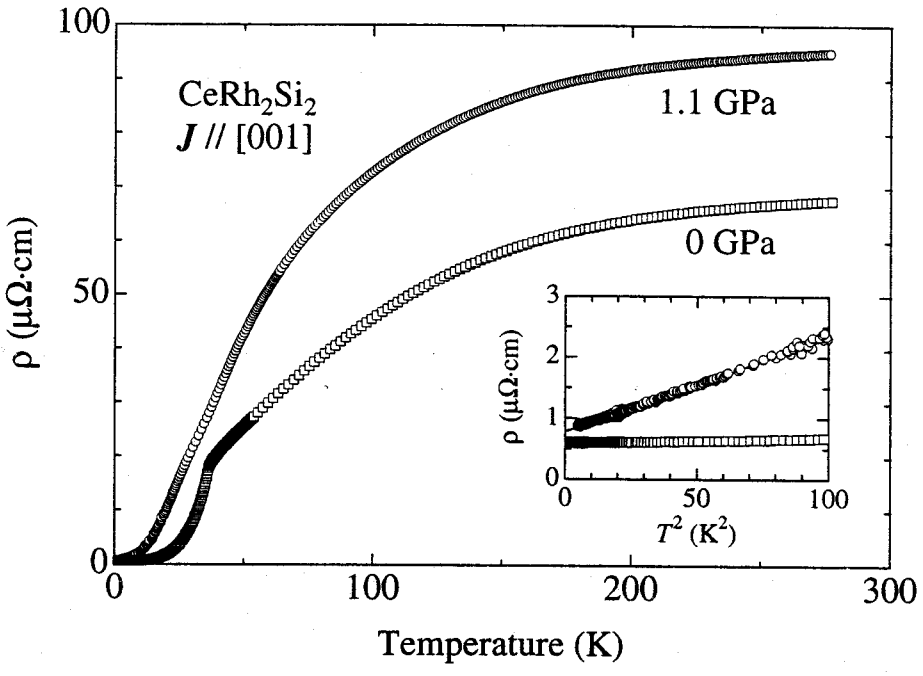

Fig. 4.2 Temperature dependence of the electrical resistivity at $P = 0$ GPa and 1.1 GPa in $CeRh_2Si_2$. The inset shows the T^2 dependence of the electrical resistivity at low temperature.

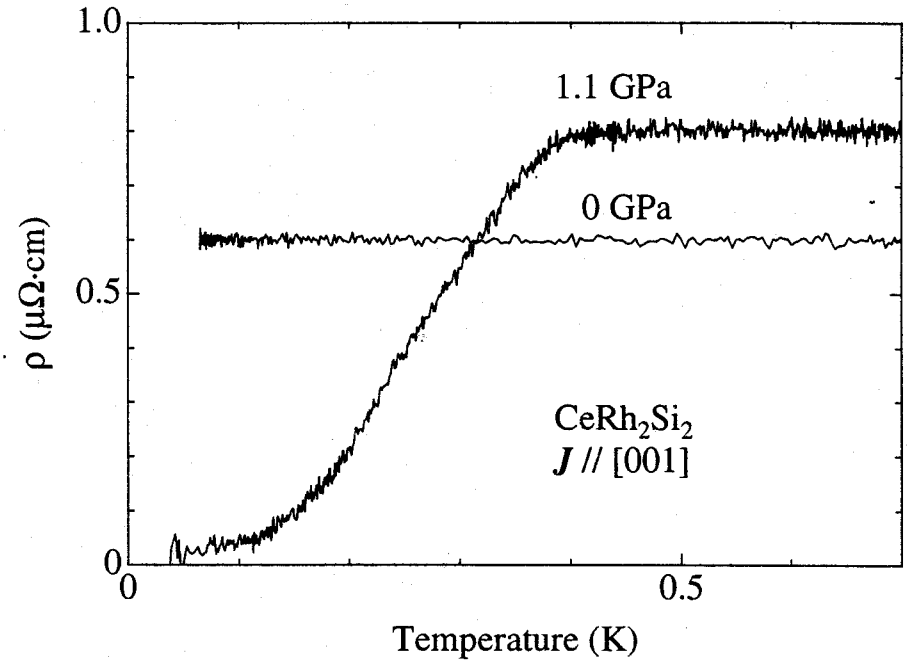

Fig. 4.3 Low-temperature electrical resistivity at $P = 0$ GPa and 1.1 GPa in $CeRh_2Si_2$.

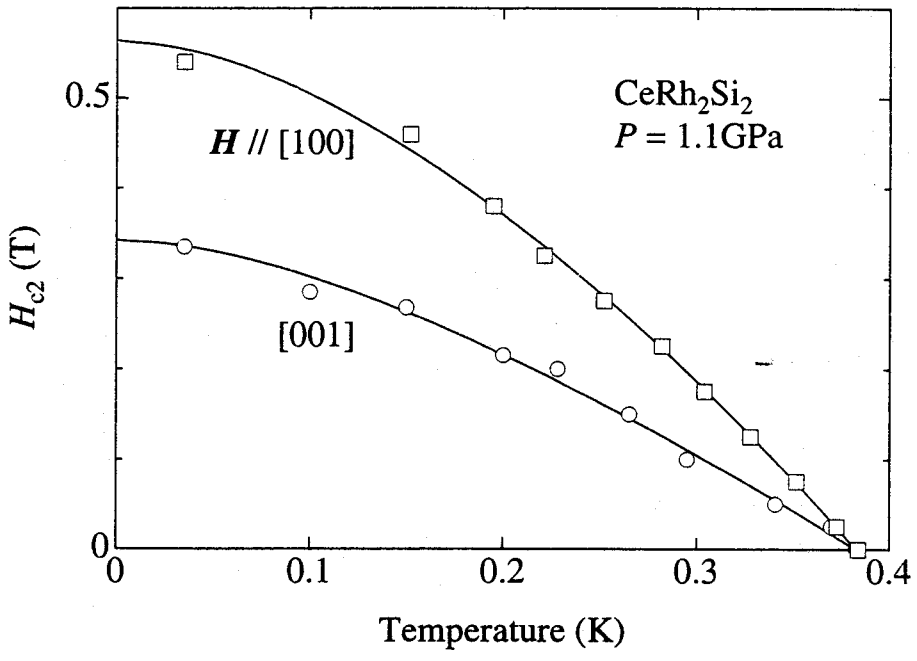

Fig. 4.4 Temperature dependence of H_{c2} at $P = 1.1$ GPa in $CeRh_2Si_2$. Solid lines are guides to eyes.

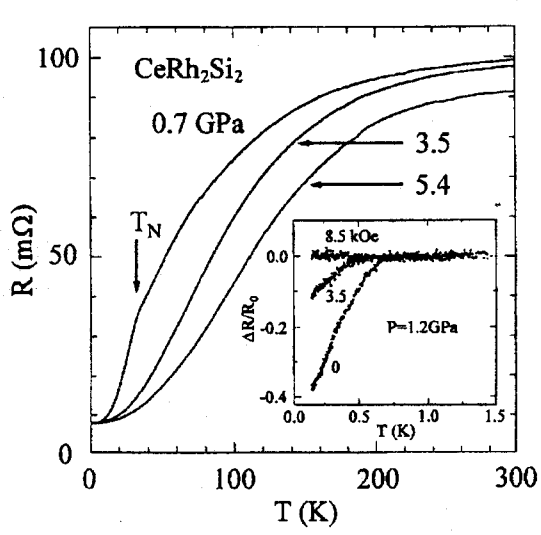

Fig. 4.5 Temperature dependence of the electrical resistance in $CeRh_2Si_2$ under high pressures. The inset shows typical resistance drop.

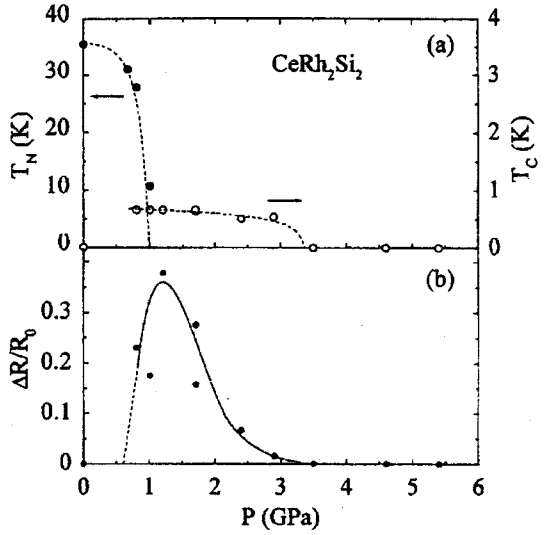

Fig. 4.6 (a) P–T phase diagram of $CeRh_2Si_2$. Closed and open circles represent the antiferromagnetic transition T_{N1} and the onset temperature T_c, respectively. (b) Pressure dependence of the relative decrease.

consistent with the previous value of 350 mK.[32,33]

We also measured the resistivity under magnetic fields and determined the upper critical field H_{c2} for superconductivity. Figure 4.4 shows the temperature dependence of H_{c2} for the fields along the [100] and [001] directions. The coherence length is estimated as 240 Å for [100] and 310 Å for [001] from $H_{c2}(0)$ $(= \Phi_0/2\pi\xi^2)$, where Φ_0 is the quantum flux. The present anisotropy of H_{c2} is related to the corresponding anisotropy of the magnetic susceptibility. As described in Sec. 4.1.3, the ratio of $\chi_c/\chi_a = 3.8$ at low temperatures. This is most likely reflected in the anisotropy of H_{c2} as the paramagnetic effect.

Second, we show the results of high-quality polycrystalline sample (RRR=62), where pressure was applied by utilizing a DAC. Figure 4.5 shows the temperature dependence of the electrical resistance under high pressure in the polycrystal $CeRh_2Si_2$. A kink corresponding to T_{N1} is observed at 31 and 28 K under pressures of 0.7 and 0.8 GPa, respectively; it disappears above 1.0 GPa. The inset in Fig. 4.5 shows the resistance drop in the low temperature range at a pressure of 1.2 GPa. Since the resistance drop is suppressed by an external field below 1 T, superconductivity is partially realized in the present sample. Zero resistance cannot be observed also through this experiment. Figure 4.6(a) shows the P–T phase diagram, where T_c is determined by the onset of the

resistance drop. Figure 4.6(b) shows the pressure dependence of the relative decrease against the residual resistance. The onset temperature $T_c \sim 600$ mK shows no obvious pressure dependence up to 2.9 GPa and is higher than the previous value[32,33] or the value obtained with a single crystal sample. The relative decrease exhibits a maximum of $\Delta R/R_0 \sim 38\%$ at 1.2 GPa and disappears at 3.5 GPa. This behavior is similar to the previous results.[32,33]

4.1.2 Specific heat

Figure 4.7 shows the temperature dependence of the specific heat in $CeRh_2Si_2$ and $LaRh_2Si_2$. We can find two anomalies which correspond to T_{N1} and T_{N2}. An inset indicate the T^2-dependence of the specific heat in the form of C/T. The specific heat C is well explained by the simple form of $\gamma T + \beta T^3$. A γ-value is 23 mJ/K^2·mol in $CeRh_2Si_2$, and 11 mJ/K^2·mol in $LaRh_2Si_2$. As indicated in the previous paper,[32,39] at about 40 K the magnetic entropy reaches approximately $R \ln 2$, indicating the doublet ground state of the $4f$ levels.

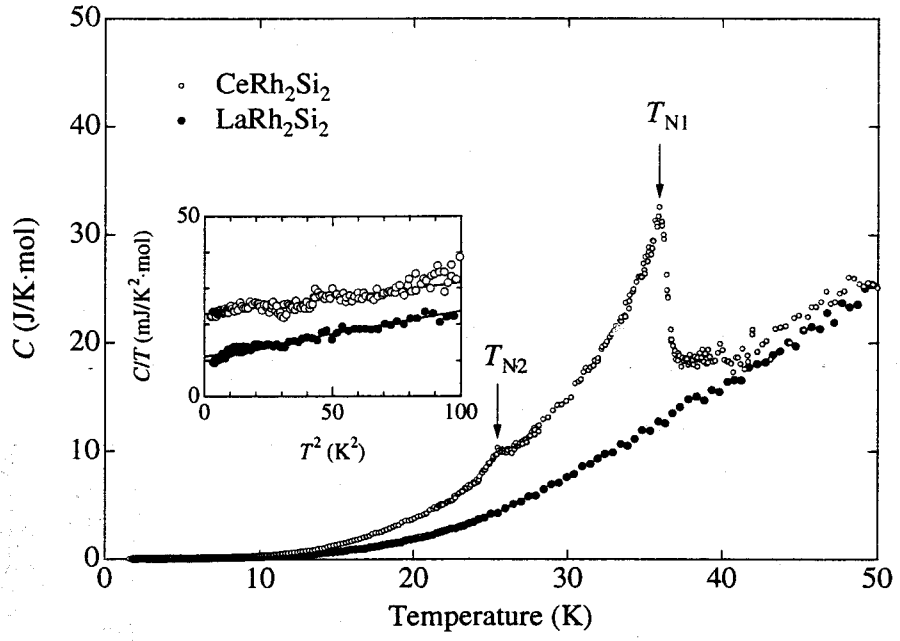

Fig. 4.7 Temperature dependence of the specific heat in $CeRh_2Si_2$ and $LaRh_2Si_2$.

4.1.3 Magnetic susceptibility

at ambient pressure

We show in Fig. 4.8 the temperature dependence of the magnetic susceptibility χ. The susceptibility is also highly anisotropic, reflecting the CEF effect for the tetragonal crystal structure. The susceptibility value for the field along the [001] direction is much higher than that for the [100] direction. The magnetic susceptibility above 100 K follows the Curie-Weiss law. The effective Bohr magneton is $3.0\mu_B$/Ce for both the field directions, which is 20% larger than the value of Ce^{3+}, $2.54\mu_B$/Ce. This discrepancy is mainly due to a large CEF splitting energy.

In order to determine the CEF property, we analyzed the temperature dependence of the magnetic susceptibility by considering CEF splitting of Ce^{3+} $4f$-levels with a molecular exchange field constant λ. The CEF Hamiltonian for the tetragonal symmetry can be represented as

$$\mathcal{H}_{\rm CEF} = B_2^0 O_2^0 + B_4^0 O_4^0 + B_4^4 O_4^4, \tag{4.1}$$

where O_ℓ^m and B_ℓ^m are the Steven's operators and the CEF parameters, respectively.[53] We determined the CEF parameters using a least square fitting. The solid lines in Fig. 4.8

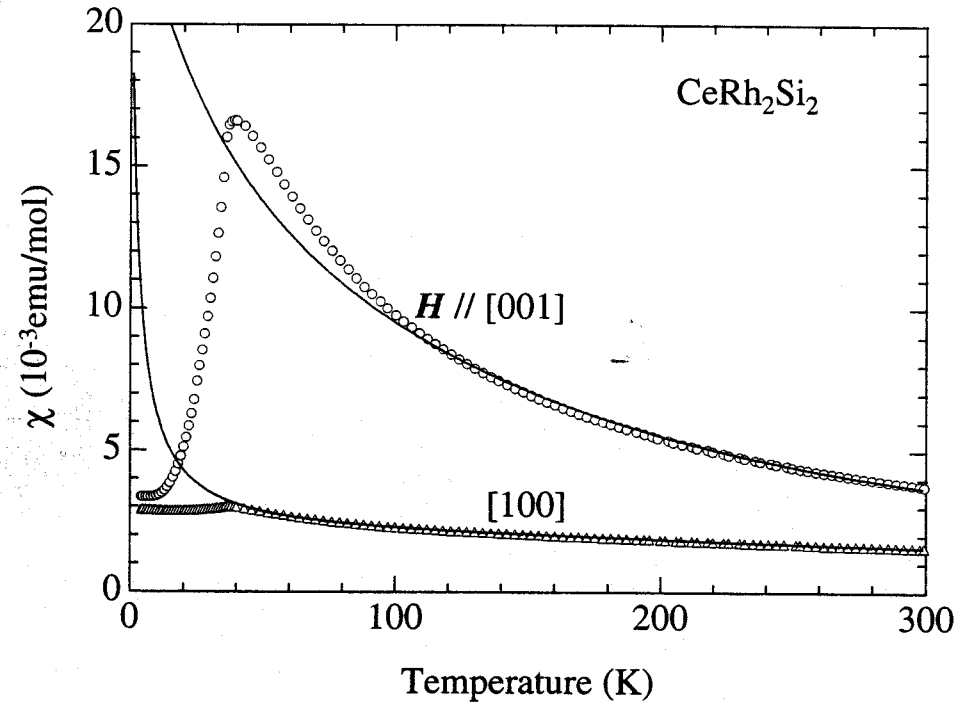

Fig. 4.8 Temperature dependence of the magnetic susceptibility in $CeRh_2Si_2$.

Table 4.I CEF parameters, energy level scheme and the corresponding wave functions.

CEF parameters						
B_2^0	B_4^0	B_4^4	λ			
−35 (K)	0.60 (K)	2.5 (K)	−40 (mol/emu)			
energy levels and wave functions						
E(K)	$\|+5/2\rangle$	$\|+3/2\rangle$	$\|+1/2\rangle$	$\|-1/2\rangle$	$\|-3/2\rangle$	$\|-5/2\rangle$
680	0	0	1	0	0	0
680	0	0	0	1	0	0
310	0	0.975	0	0	0	0.224
310	0.224	0	0	0	0.975	0
0	0	−0.224	0	0	0	0.975
0	−0.975	0	0	0	0.224	0

represent our calculations and are in approximately agreement with the experimental results, where the parameters are $B_2^0 = -35$ K, $B_4^0 = 0.60$ K, $B_4^4 = 2.5$ K and $\lambda = -40$ mol/emu. The six-fold degenerated $4f$-levels are split into three doublets. From this fitting, we determined that the excited doublets are separated by 310 K and 680 K from the ground state, respectively. Therefore, the susceptibility with effective Bohr magneton of $2.54\mu_B$/Ce is realized above 700 K. These parameters, including wave functions, are shown in Table 4.I.

under high pressure

The temperature dependence of the susceptibility χ of $CeRh_2Si_2$ under high pressure is shown in Fig. 4.9. A magnetic field of 1 T was applied along the [100] (a-) and [001] (c-) directions. The antiferromagnetic ordering temperature T_{N1} is obtained as an onset of rapid decrease of χ_c. As shown in Fig. 4.10, T_{N1} disappears above 1.1 GPa. It is characteristic that a broad maximum of χ_c appears above T_{N1} under pressure. T_{max} tends to shift to higher temperatures and the maximum value decreases rapidly with increasing pressure, which is explained to be due to the increase of the c-f hybridization. Namely it means that the Kondo temperature increases with increasing pressure. This behavior is similar to the case of $CeRu_2Si_2$ which shows a maximum of χ_c and metamagnetic magnetization process in the field parallel to the [001] direction. The χ_a also decreases slightly and also shows a broad maximum under high pressure. Application of pressure reduces the magnetic anisotropy: $\chi_c/\chi_a = 5.6$ at ambient pressure and 3.8 at $p_c \simeq 1$ GPa, which were estimated from the maximum values of χ_c and χ_a.

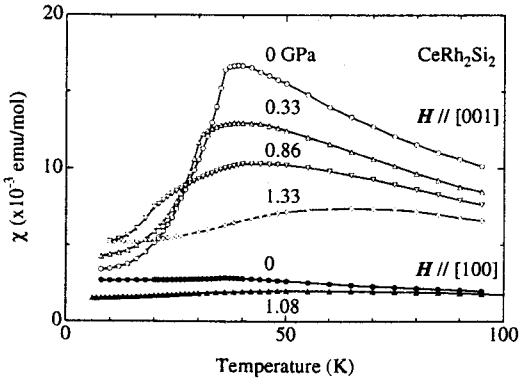

Fig. 4.9 Temperature dependence of the magnetic susceptibility along the [100] and [001] directions in $CeRh_2Si_2$ under high pressures.

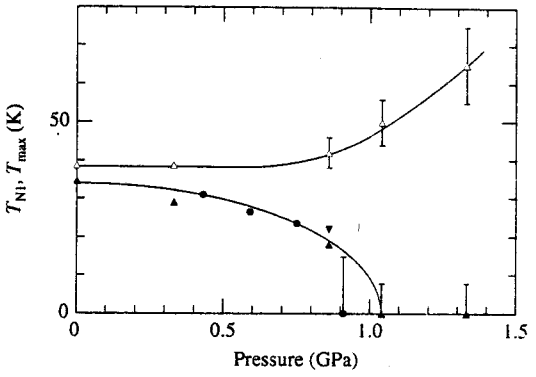

Fig. 4.10 Pressure dependence of T_{N1} (▲, ▼) single crystal; (•) polycrystal and T_{max} (△) where the χ_c shows the broad maximum.

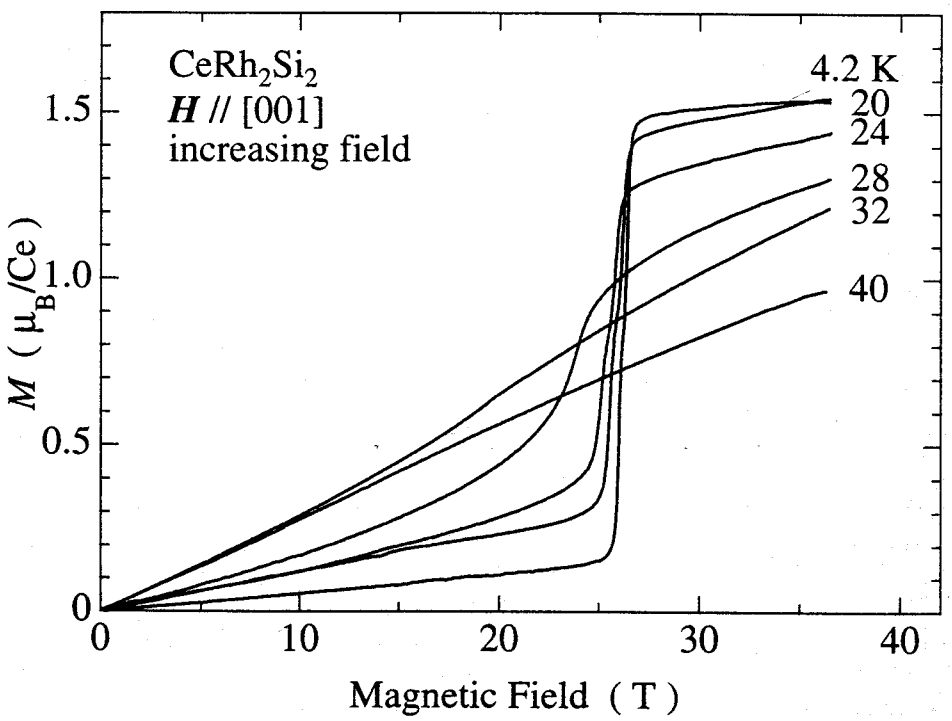

Fig. 4.11 Magnetization curve along the [001] direction at various temperatures in $CeRh_2Si_2$.

4.1.4 Magnetization

at ambient pressure

Figure 4.11 shows the magnetization curve along the [001] direction at various temperatures with an increasing magnetic field. The metamagnetic transition is observed below T_{N1}=36 K. For example, the transition field is about 26 T at 4.2 K. A saturated moment is 1.55μ_B/Ce. This value is smaller than the magnetic moment of 2.1μ_B/Ce, which is expected from the present CEF-level scheme. Similar metamagnetization has been reported in the recent magnetization experiment performed by Abe *et al.*[54] Here, the magnetic moment in the neutron experiment is estimated as 1.42μ_B/Ce and 1.34μ_B/Ce.[38]

The transition field of 26 T at 4.2 K does not change with increasing the temperature, but decreases steeply above 26 K. These features are clearly shown in an inset of Fig. 4.12

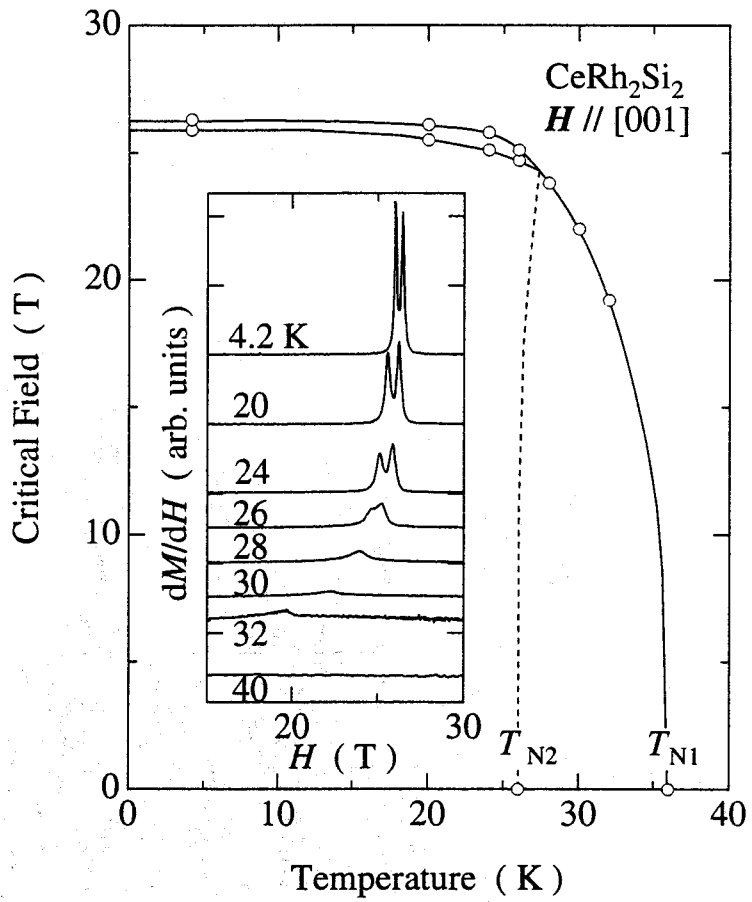

Fig. 4.12 Magnetic phase diagram in $CeRh_2Si_2$. An inset shows the differential magnetization curves.

by the differential magnetization curves, dM/dH. Here, we note that the vertical scales at 32 and 40 K are enlarged by five and ten times, respectively, compared to the other curves. The metamagnetic transition is not found in the paramagnetic phase, as shown in the dM/dH-curve at 40 K. It is interesting that the metamagnetic transition consists of two steps. One step corresponds to half of the saturated magnetic moment at 25.9 T and the other step occurs at 26.3 T in the magnetization curve at 4.2 K. The two-step structure disappears above 26 K and is changed into a one-step style in the temperature range of 28 to 36 K. We have performed the free energy calculations on the basis of the mean field model with Ising spin system as in URu_2Si_2 with the same tetragonal crystal structure.[55] The transition with the two-step structure has not been obtained in calculations.

under high pressure

Figure 4.13 shows the pressure dependence of the magnetization process of $CeRh_2Si_2$ for the field along the [001] direction at 6.0 K. The metamagnetic transition field H_M increases with increasing pressure and the the metamagnetic transition also observed in the paramagnetic state at 1.15 GPa. The magnitude of the saturation moment decreases with increasing pressure. Figure 4.14 shows the temperature dependence of a

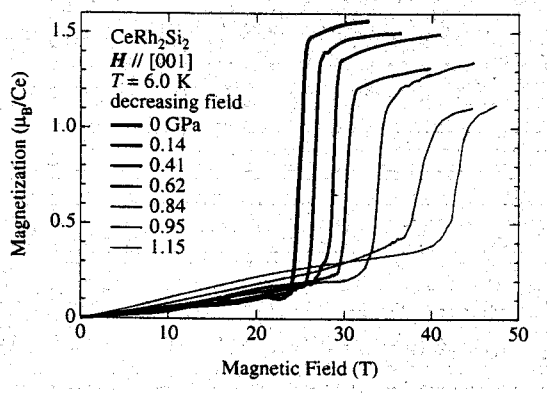

Fig. 4.13 High-field magnetization at various pressures in $CeRh_2Si_2$.

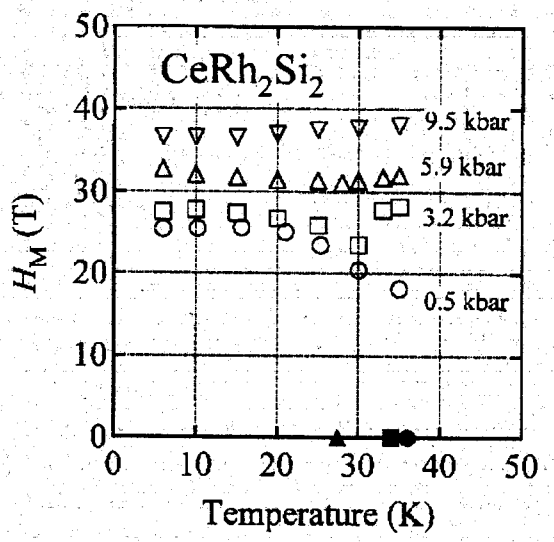

Fig. 4.14 Temperature dependence of H_M in $CeRh_2Si_2$ under several pressures. Filled circle, square and triangle indicate the T_{N1} at 0.5, 3.2 and 5.9 kbar, respectively.

metamagnetic transition field H_M under several pressures. H_M is found to decrease with increasing temperature below T_{N1} clearly at 0.32 GPa and slightly at 0.59 GPa but it begins to increase above T_{N1} for 0.59 GPa. This behaviour is observed in the heavy fermion antiferromagnetics of UPd_2Al_3[56] and URu_2Si_2[57] or the paramagnetic heavy fermion compound $CeRu_2Si_2$[58] at ambient pressure. At 0.95 GPa, H_M monotonically increases with increasing temperature as in a heavy fermion paramagnet of $CeRu_2Si_2$. The present metamagnetic transition is discussed from the view point that the itinerant-f electron system is changed into the localized-f electron system by the magnetic field. This might not be due to the phase transition but due to crossover based on the many-body Kondo effect.

4.1.5 Thermal expansion coefficient

We show in Fig. 4.15 the temperature dependence of the linear thermal expansion coefficient α in $CeRh_2Si_2$. Here, open circles and squares are those along the [001] and [100] directions, respectively. With decreasing the temperature, the thermal expansion coefficient along the [001] direction has a broad maximum around 170 K, while the one along the [100] direction decreases linearly with decreasing the temperature. The ther-

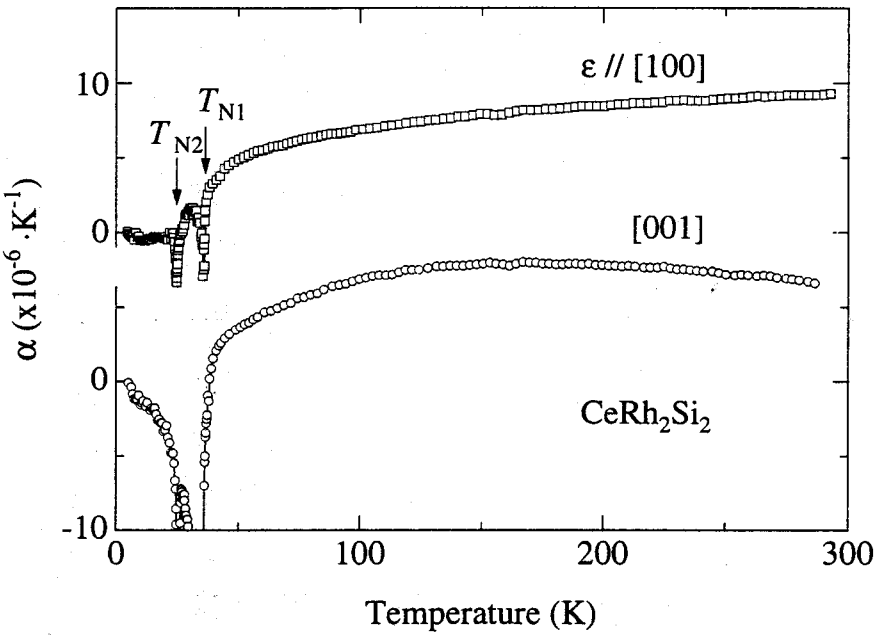

Fig. 4.15 Temperature dependence of the thermal expansion coefficient along the [100] and [001] directions in $CeRh_2Si_2$.

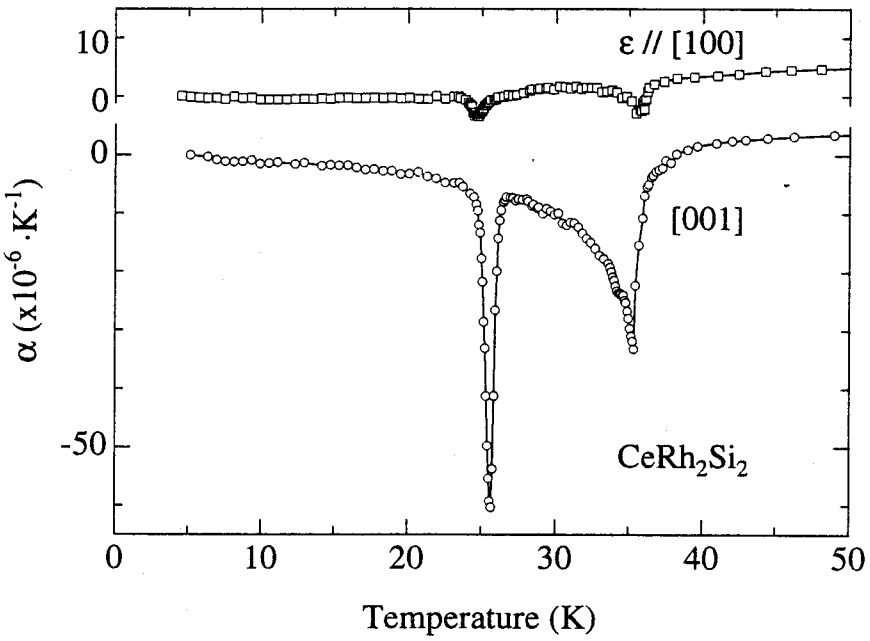

Fig. 4.16 Low temperature region of the thermal expansion coefficient along the [100] and [001] directions in $CeRh_2Si_2$.

mal expansion coefficient in $CeRh_2Si_2$ exhibits sharp anomalies at the magnetic ordering temperatures, T_{N1} and T_{N2}. The low temperature region is enlarged in scale, as shown in Fig. 4.16. The magnetic transitions are pronounced for the [001] direction, compared to the [100] direction. Figure 4.17 shows the temperature dependence of the thermal expansion coefficient in $LaRh_2Si_2$ along the [001] and [100] directions. The thermal expansion coefficient in $LaRh_2Si_2$ is positive at high temperatures and decreases with decreasing the temperature for both directions.

We have estimated the magnetic component of the thermal expansion coefficient α_{mag} in $CeRh_2Si_2$ by subtracting the one of $LaRh_2Si_2$ from $CeRh_2Si_2$: $\alpha_{mag} = \alpha(CeRh_2Si_2) - \alpha(LaRh_2Si_2)$. Figure 4.18 shows the temperature dependence of α_{mag}. Although α_{mag} along the [001] direction is positive and the one along the [100] direction is negative, both have a broad maximum or minimum around 170 K. This peak corresponds to the Schottky anomaly of the specific heat.

We have calculated the magnetic component of the thermal expansion coefficient on the basis of the CEF level scheme which is estimated from the magnetic susceptibility. The total Hamiltonian for the present case is written as follows:

$$\mathcal{H} = \mathcal{H}_{CEF} + \mathcal{H}_{me} + E_{el}. \tag{4.2}$$

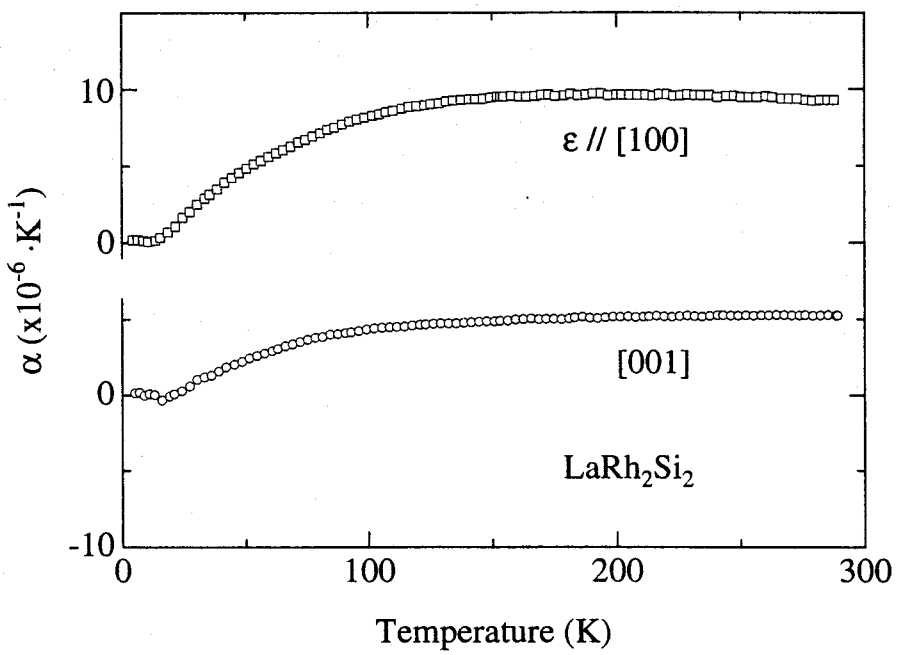

Fig. 4.17 Temperature dependence of the thermal expansion coefficient along the [100] and [001] directions in $LaRh_2Si_2$.

The first term is the CEF Hamiltonian as expressed in eq. (4.1). The second term is the one-ion magnetoelastic interaction which is defined as the coupling between the quadrupole moment and the strain:

$$\begin{aligned} \mathrm{H_{me}} = &-(G^{\alpha 1}\varepsilon^{\alpha 1} + G^{\alpha 2}\varepsilon^{\alpha 2})\boldsymbol{O}_2^0 - G^{\gamma}\varepsilon^{\gamma}\boldsymbol{O}_2^2 \\ &- G^{\delta}\varepsilon^{\delta}\boldsymbol{O}_{xy} - G^{\varepsilon}(\varepsilon_1^{\varepsilon}\boldsymbol{O}_{zx} + \varepsilon_2^{\varepsilon}\boldsymbol{O}_{yz}). \end{aligned} \tag{4.3}$$

Here, the G^{μ} and ε^{μ} are the coupling constant and the normal strain corresponding to the tetragonal symmetry, respectively. The elastic energy E_{el} is written as

$$\begin{aligned} E_{\mathrm{el}} = &\frac{1}{2}C_0^{\alpha 1}(\varepsilon^{\alpha 1})^2 + C_0^{\alpha 12}\varepsilon^{\alpha 1}\varepsilon^{\alpha 2} + \frac{1}{2}C_0^{\alpha 2}(\varepsilon^{\alpha 2})^2 \\ &+ \frac{1}{2}C_0^{\gamma}(\varepsilon^{\gamma})^2 + \frac{1}{2}C_0^{\delta}(\varepsilon^{\delta})^2 + \frac{1}{2}C_0^{\varepsilon}[(\varepsilon_1^{\varepsilon})^2 + (\varepsilon_2^{\varepsilon})^2], \end{aligned} \tag{4.4}$$

where C_{λ}^{μ} are the symmetrized elastic constants. The detailed formulae for the symmetrized strain and the elastic constants for the tetragonal symmetry were calculated by Morin *et al.*[59] The equilibrium formula for the symmetrized strain is obtained by

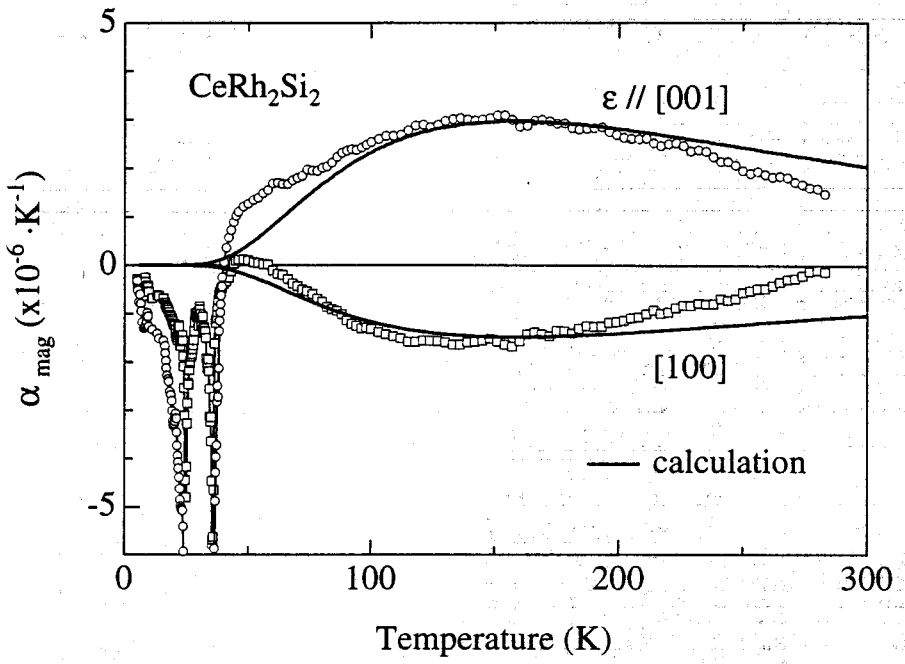

Fig. 4.18 Temperature dependence of the magnetic component of the thermal expansion coefficient along [100] and [001] in $CeRh_2Si_2$. Solid lines are the results of CEF calculations.

minimizing the free energy with respect to the strain as follows:

$$\varepsilon^{\alpha 1} = \frac{G^{\alpha 1}C_0^{\alpha 2} - G^{\alpha 2}C_0^{\alpha 12}}{C_0^{\alpha 1}C_0^{\alpha 2} - (C_0^{\alpha 12})^2}\langle \boldsymbol{O}_2^0 \rangle, \tag{4.5a}$$

$$\varepsilon^{\alpha 2} = \frac{G^{\alpha 2}C_0^{\alpha 1} - G^{\alpha 1}C_0^{\alpha 12}}{C_0^{\alpha 1}C_0^{\alpha 2} - (C_0^{\alpha 12})^2}\langle \boldsymbol{O}_2^0 \rangle, \tag{4.5b}$$

$$\varepsilon^{\gamma} = \frac{G^{\gamma}}{C_0^{\gamma}}\langle \boldsymbol{O}_2^2 \rangle, \tag{4.5c}$$

$$\varepsilon^{\delta} = \frac{G^{\delta}}{C_0^{\delta}}\langle \boldsymbol{O}_{xy} \rangle, \tag{4.5d}$$

$$\varepsilon_1^{\varepsilon} = \frac{G_1^{\varepsilon}}{C_0^{\varepsilon}}\langle \boldsymbol{O}_{yz} \rangle, \tag{4.5e}$$

$$\varepsilon_2^{\varepsilon} = \frac{G_2^{\varepsilon}}{C_0^{\varepsilon}}\langle \boldsymbol{O}_{zx} \rangle. \tag{4.5f}$$

(4.5g)

The linear strain ε_i is expresses by the combination of the above symmetrized strain as

$$\varepsilon_{[100]} = \frac{1}{\sqrt{3}}\varepsilon^{\alpha 1} + \frac{2}{\sqrt{6}}\varepsilon^{\alpha 2}, \tag{4.6a}$$

$$\varepsilon_{[001]} = \frac{1}{\sqrt{3}}\varepsilon^{\alpha 1} - \frac{1}{\sqrt{6}}\varepsilon^{\alpha 2}. \tag{4.6b}$$

From eqs. (4.5) and (4.6), the linear strain is simply written as

$$\varepsilon_i = g_i \langle \boldsymbol{O}_2^0 \rangle. \tag{4.7}$$

Here, the index i indicates the direction of the linear strain. The thermal expansion coefficient for the tetragonal crystal structure can be derived by differentiating the strain in eq. (4.7) by the temperature:

$$\alpha_i = g_i \frac{\langle E\boldsymbol{O}_2^0 \rangle - \langle E \rangle \langle \boldsymbol{O}_2^0 \rangle}{k_{\mathrm{B}} T^2}. \tag{4.8}$$

While the coefficient g_i in eqs. (4.7) and (4.8) is represented by the elastic constants C_μ^λ and the magnetoelastic coupling constants G^μ, it is determined by fitting to experimental results. The parameters $g_{[001]} = -1.56 \times 10^{-4}$ and $g_{[100]} = 7.8 \times 10^{-4}$ are determined so as to reproduce the experimental results in the paramagnetic region. The fitting results, which are shown by solid lines in Fig. 4.18, reproduce the experimental ones, exhibiting a maximum or minimum around 170 K, which is roughly half of the energy between the ground state and the first excited state.

4.1.6 dHvA effect

at ambient pressure

Figure 4.19 shows the typical dHvA oscillation for the field along the [100] direction at 29 mK and the corresponding fast Fourier transformation (FFT) spectrum. Branches κ, o, π, d (split into 4 branches) and f are fundamentals, while the others are higher harmonics. Branches denoted by Greek letters were detected in the previous experiment done by Abe *et al.*[60] (see Fig. 2.21), while two branches denoted by Latin Alphabet, d and f, are new ones. The dHvA frequency for these branches ranges from 855 to 6610 T. All the dHvA frequencies detected in the experiment are listed in Table 4.II.

Figure 4.20 shows the angular dependence of of the dHvA frequency in $CeRh_2Si_2$. Because $CeRh_2Si_2$ is an antiferromagnet with a large moment $\sim 1.6\mu_{\mathrm{B}}$, we can regard that the $4f$ electrons are localized. The topology of the Fermi surface in $CeRh_2Si_2$ is thus considered to be similar to that in $LaRh_2Si_2$. Figure 4.21–4.24 shows the calculated

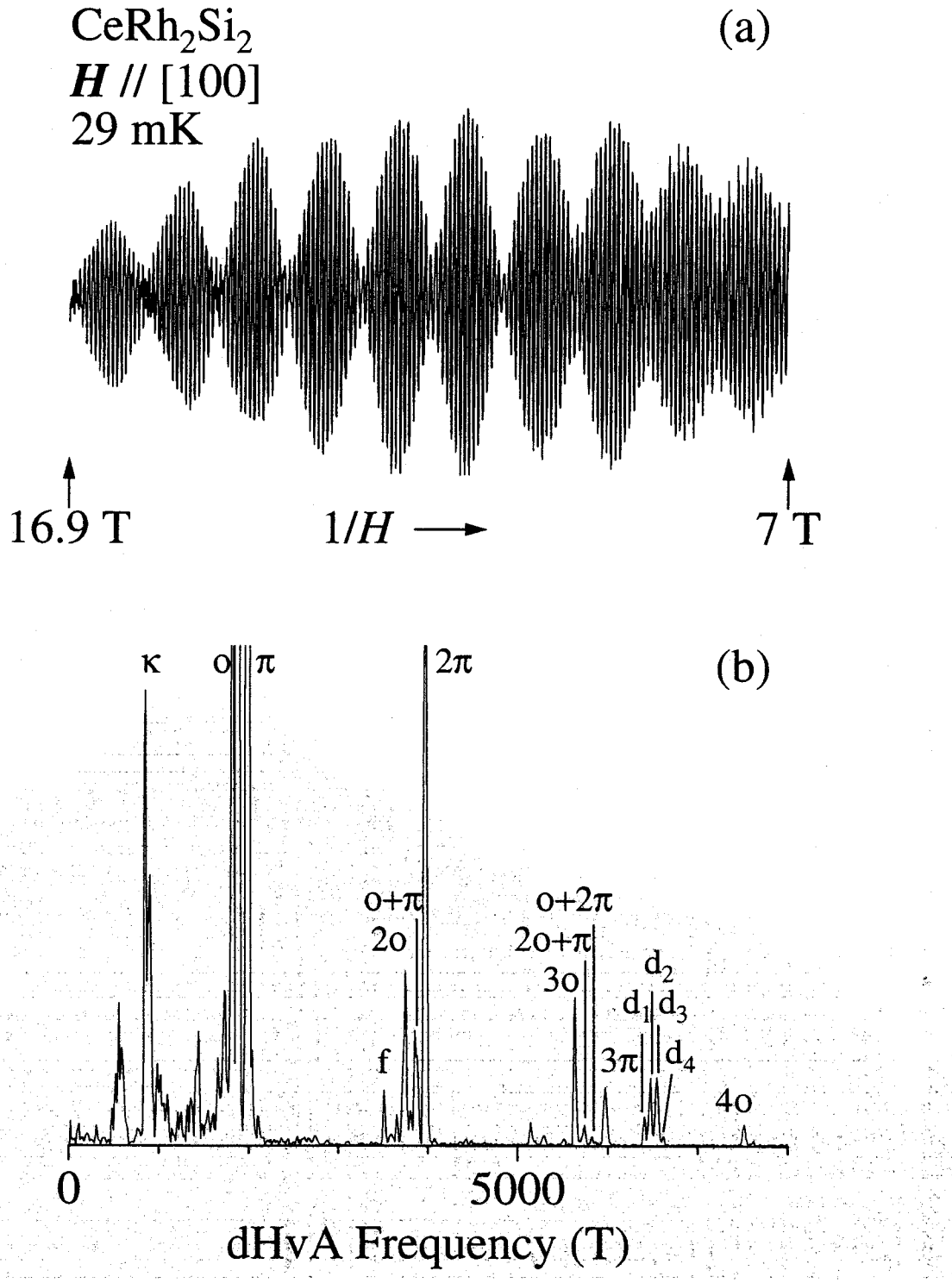

Fig. 4.19 Typical dHvA oscillation and its FFT spectrum for the field along the [100] direction in $CeRh_2Si_2$.

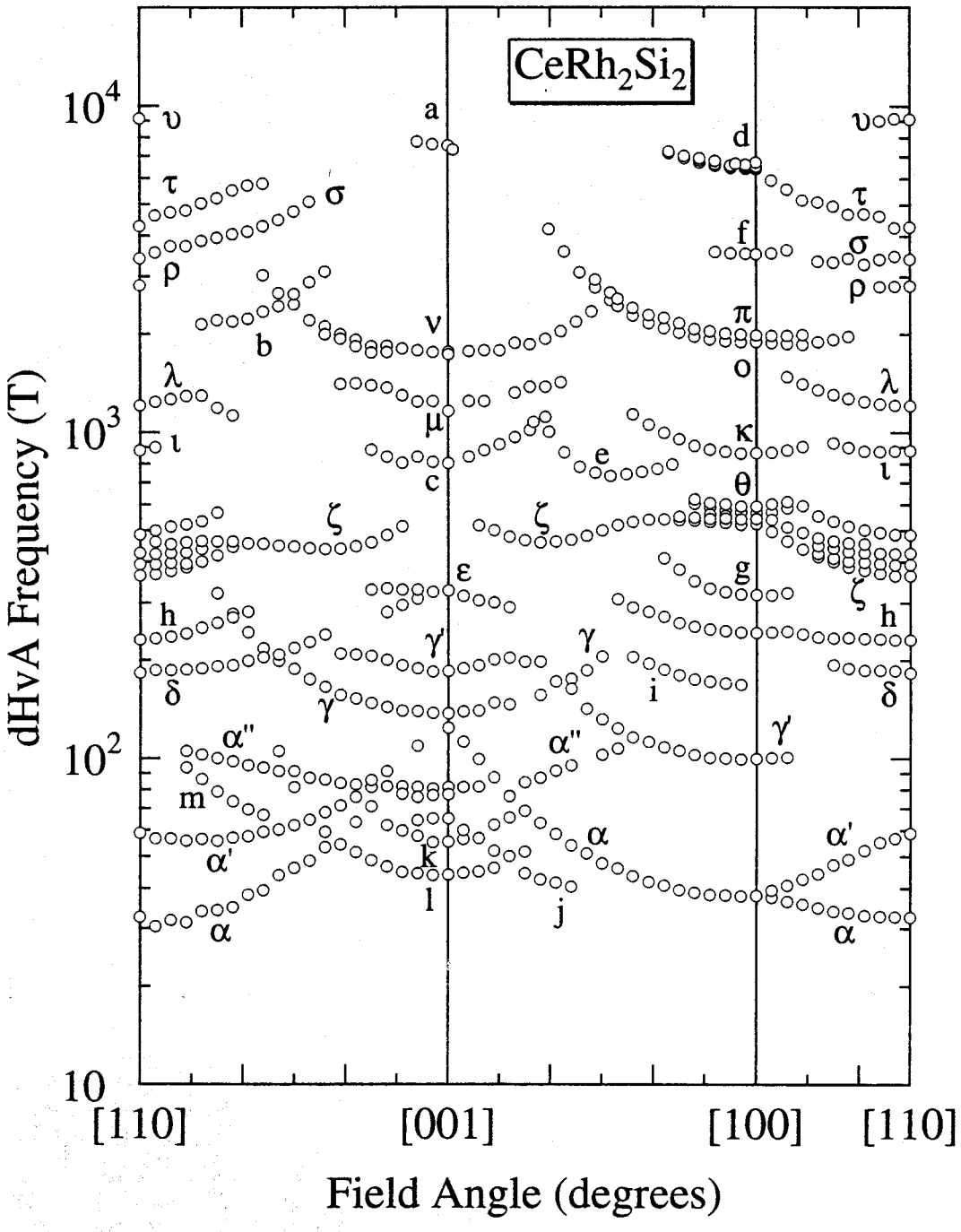

Fig. 4.20 Angular dependence of the dHvA frequency in $CeRh_2Si_2$.

Table 4.II dHvA frequency F, cyclotron mass m_c^*, Dingle temperature T_D and the mean free path ℓ in $CeRh_2Si_2$.

$H \parallel [110]$				$H \parallel [001]$				$H \parallel [100]$			
F (T)	m_c^* (m_0)	T_D (K)	ℓ (Å)	F (T)	m_c^* (m_0)	T_D (K)	ℓ (Å)	F (T)	m_c^* (m_0)	T_D (K)	ℓ (Å)
υ 9110	3.8	2.20	880	a 7560	6.4	0.78	1540	d_4 6610	6.6	—	—
τ 4250	4.7	0.64	1670	ν 1770	2.4	0.66	2050	d_3 6540	6.5	—	—
σ 3450	6.1	0.41	1820	ν' 1730	2.2	—	—	d_2 6470	6.1	—	—
ρ 2800	3.2	1.06	1210	μ 1160	3.7	0.39	1870	d_1 6400	5.7	—	—
λ 1200	1.4	—	—	c 804	4.9	—	—	f 3510	3.3	—	—
ι 879	4.8	0.31	1550	ε 327	1.9	0.42	1760	π 1990	3.6	—	—
ζ_6 482	0.90	—	—	γ' 184	1.4	0.42	1770	o 1890	3.1	—	—
ζ_5 425	1.6	—	—	γ 137	0.45	2.87	700	κ 855	3.9	0.29	2030
ζ_4 394	1.5	—	—	α'' 81	1.4	—	—	θ 595	2.1	—	—
ζ 362	0.76	—	—	77	0.26	—	—	θ' 571	2.0	—	—
h 231	—	—	—	j 66	0.39	—	—	ζ' 545	1.9	—	—
δ 183	—	—	—	k 56	0.41	—	—	ζ 524	1.7	—	—
α' 58	0.72	—	—	l 44	0.43	—	—	g 318	1.9	—	—
α 32	0.36	—	—					h 246	2.0	—	—
								γ' 100	2.1	—	—
								α 38	0.47	0.45	2200

angular dependence of the dHvA frequency in $LaRh_2Si_2$. The corresponding Fermi surface is shown in Figs. 4.25. The calculated dHvA frequency and the corresponding band mass are listed in Table. 4.III.

We will compare the experimental results with the calculated ones. The magnetic structure of the ground state is supposed to be a $4\boldsymbol{q}$-structure, as shown in Fig. 2.14, from the neutron diffraction measurement.[38] The magnetic unit cell is four times as large as that of a chemical one. Correspondingly, the Brillouin zone of $CeRh_2Si_2$ in an antiferromagnetic state is four times as small as that in a paramagnetic state. The Fermi surface of $LaRh_2Si_2$ is folded into a smaller one, and the topology of Fermi surface will change, particularly for the complicated band 25-hole Fermi surface. On the other hand, we supposed that the band 24-hole and band 26-electron Fermi surfaces are far from the magnetic Brillouin zone boundary. Therefore, it keeps the topology of the Fermi surface unchanged or slightly altered. The calculated dHvA frequency of band 24-hole Fermi surface is shown in Fig. 4.22. The band 24-hole Fermi surface corresponds to:

1) b $(1\bar{1}0)$ – π or o [100] branches in the range from 2000 to 4000 T.

2) λ [110] – κ [100] branches in the range from 800 to 1100 T.

3) k branch centered at the [001] axis.

The calculated dHvA frequency of band 26-electron Fermi surface is shown in Fig. 4.24. The band 26-electron Fermi surface corresponds to γ-branch centered at the [001] direction. This is one of the explanation on the result of the dHvA experiment in $CeRh_2Si_2$.

Table 4.III Theoretical dHvA frequency F and the corresponding band mass m_b in $LaRh_2Si_2$.

$H \parallel [110]$			$H \parallel [001]$			$H \parallel [100]$		
	F (T)	m_b (m_0)		F (T)	m_b (m_0)		F (T)	m_b (m_0)
25 (υ)	8930	1.9	25	16830	1.5	25 (d)	6980	2.2
25 (ρ)	4530	1.6	24	9720	1.6	24 (π)	3770	0.61
24 (λ)	2170	0.46	25 (a)	8240	3.0	24 (o)	3300	0.80
26	910	0.76	25	850	1.5	25	2050	2.1
			25	290	1.0	24 (κ)	1720	0.45
			26	290	0.35	25 (ζ)	1050	1.2
			26	260	0.38	26	900	0.75
			26 (γ)	220	0.41	25 (γ')	110	0.37
			24 (k)	86	0.14			

Another explanation is based on the magnetic break through effect. If an antiferromagnetic gap is small, the electrons can break through the gap and circulate the original Fermi surface in the paramagnetic state at high fields. These is a possibility that we observed the dHvA branches both in the paramagnetic and antiferromagnetic states. Another branches can be considered to be come from the band-folded Fermi surfaces.

By using eq. (3.27), we determined the cyclotron effective mass m_c^* as shown in Fig. 4.26, and summarized m_c^* in Table 4.II.

Next, we determined the Dingle temperature from the field dependence of the dHvA amplitude by using eq. (3.32) as shown in Fig. 4.27. The T_D are listed in Table 4.II.

under high pressure

When pressure is applied to the sample, the dHvA amplitude is reduced, as shown in Fig. 4.28. Note that the dHvA amplitudes in the FFT spectra at 0 and 0.3 GPa are reduced by half compared to that at 0.8 GPa, while those at 0.9, 1.0 and 1.2 GPa are enlarged twice in Fig. 4.28. The dHvA experiments were done at 138–160 mK under pressure. The dHvA frequencies of branches κ, o and π are unchanged up to 0.5–1.0 GPa. Their amplitudes are reduced gradually with increasing pressure, and become zero above 0.8 GPa for κ and o, and above 1.1 GPa for π. The dHvA frequency of 6500 T for branch d is also unchanged up to 1.0 GPa, but this branch splits into two branches in the pressure range from 0.8 to 1.0 GPa. It is strange that amplitudes of the two branches become large. There is a possibility that one of the two branches with a dHvA frequency of 6100 T at 0.9 and 1.0 GPa corresponds to a new Fermi surface. Moreover, at 1.2 GPa we observed a new branch named A, which is different from dHvA branches below 1.0 GPa. Branch A has a relatively large amplitude, whereas branches π and d disappear completely. It is

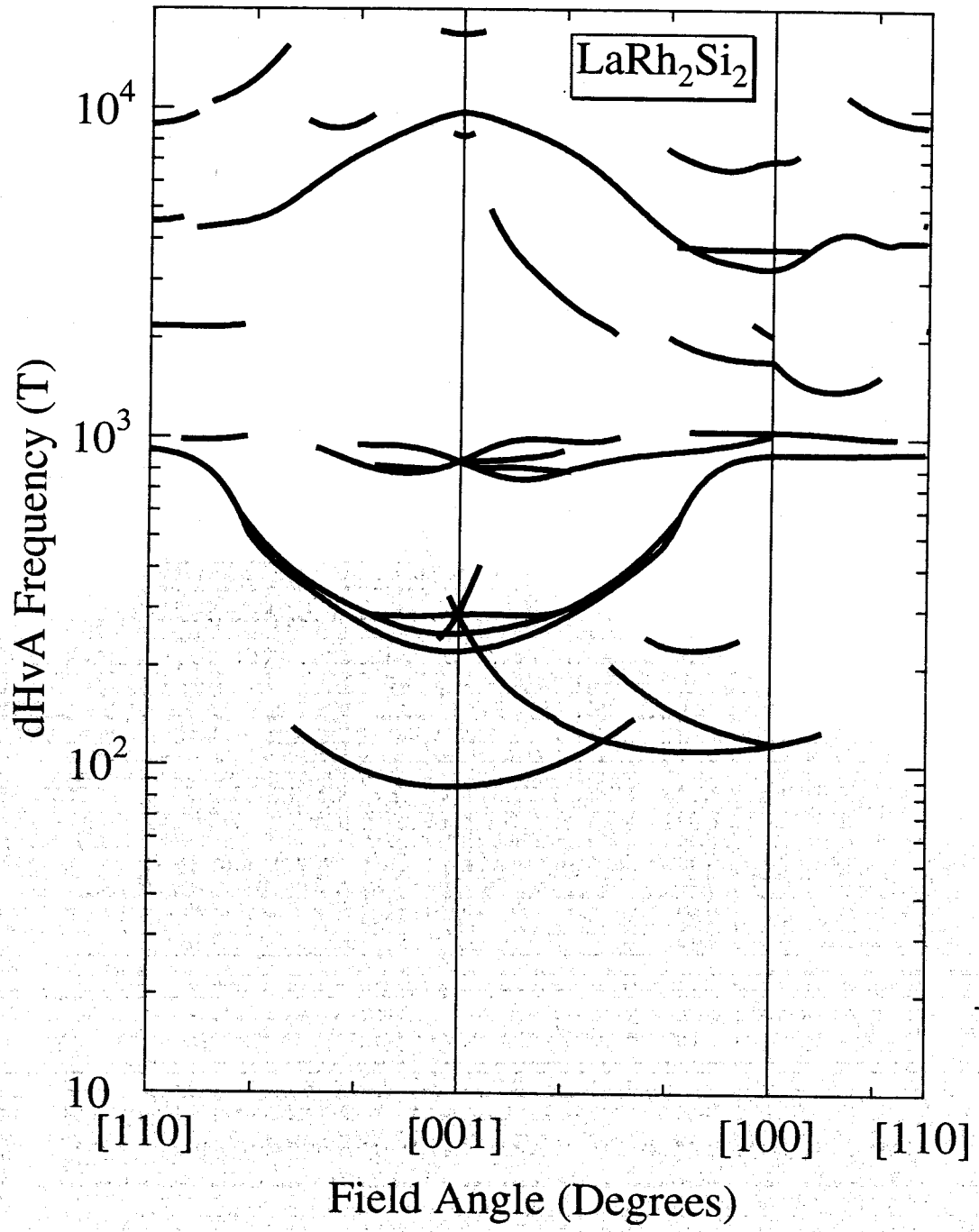

Fig. 4.21 Theoretical angular dependence of the dHvA frequency in $LaRh_2Si_2$.

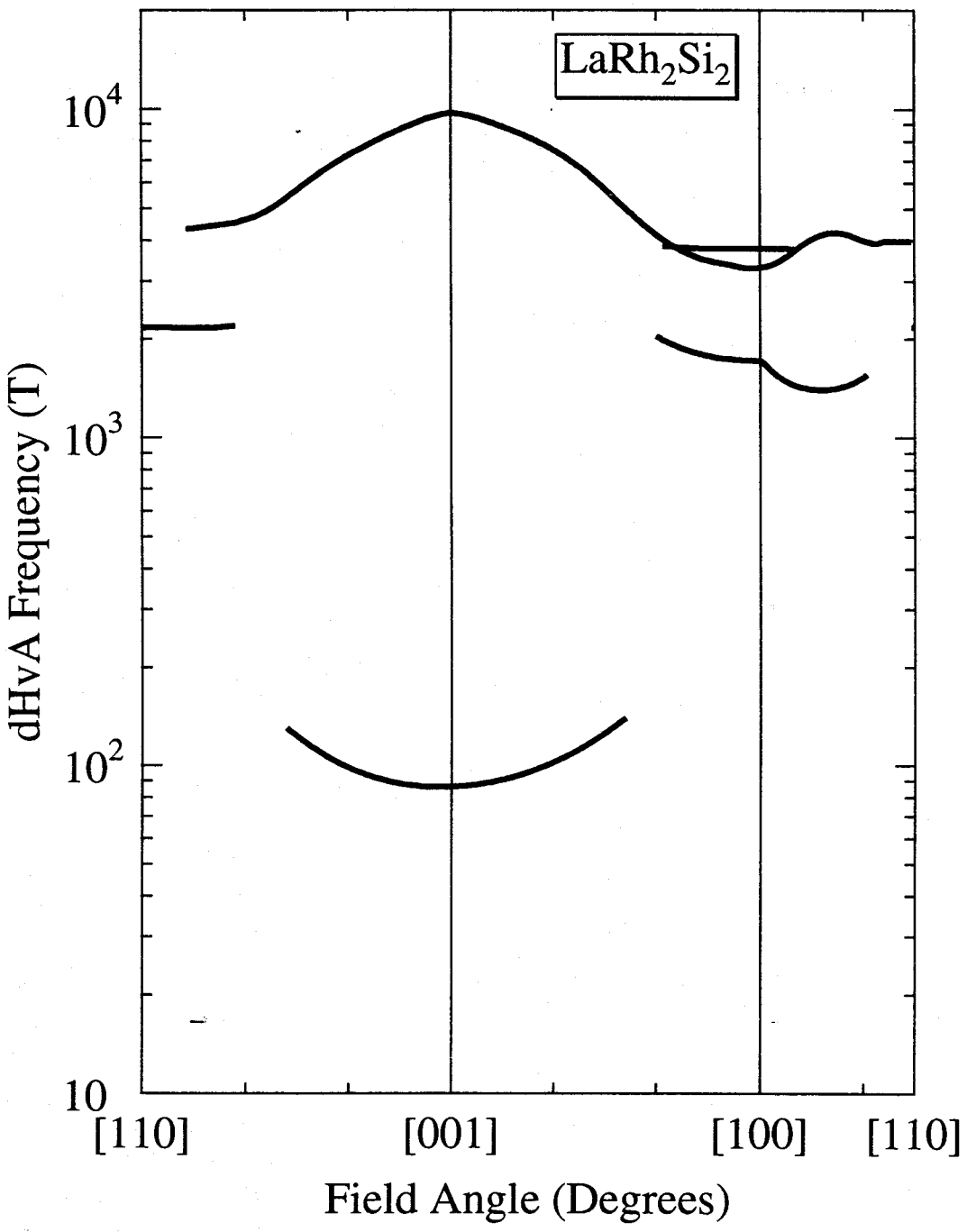

Fig. 4.22 Theoretical angular dependence of the dHvA frequency corresponding to band 24-hole Fermi surface in $LaRh_2Si_2$.

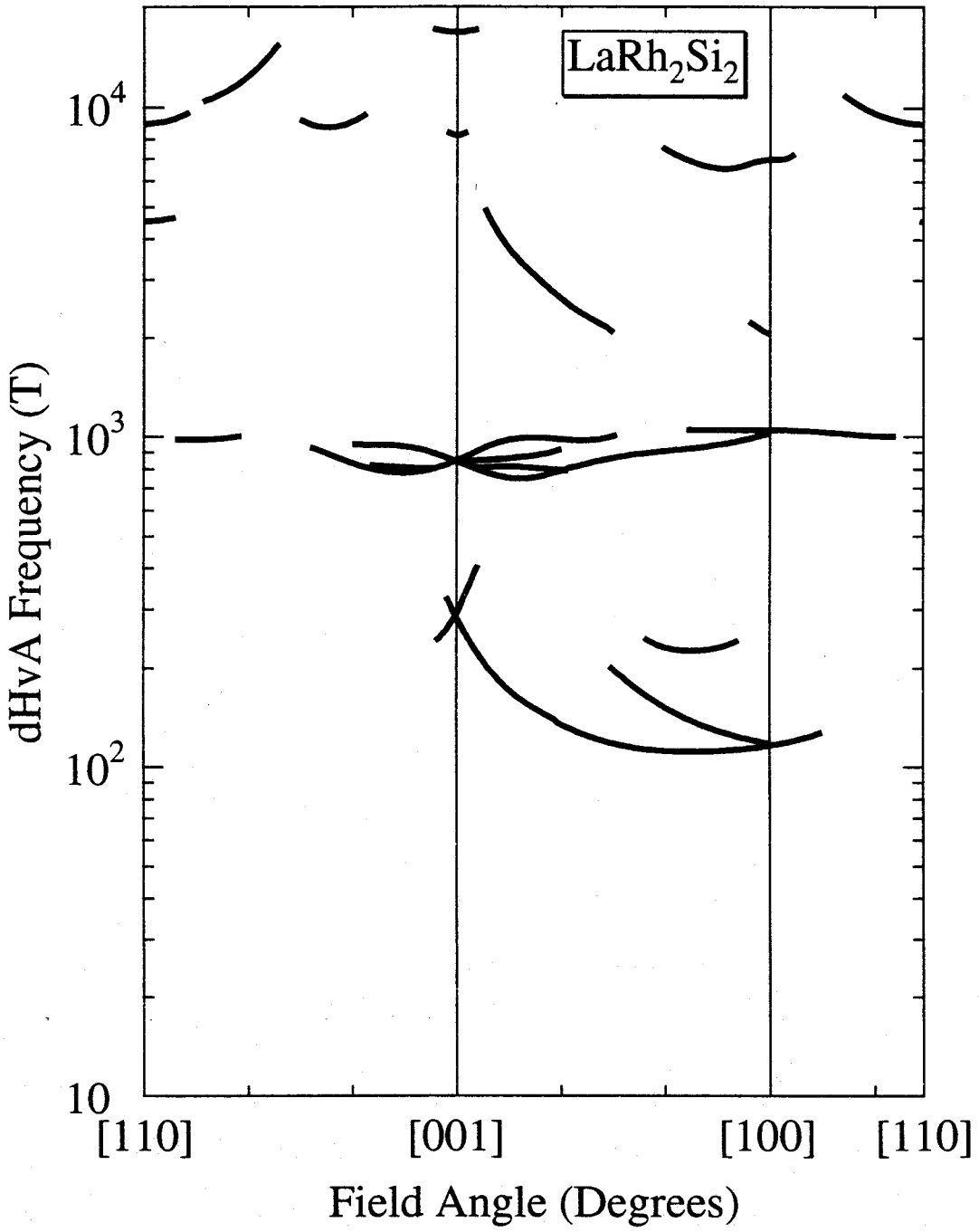

Fig. 4.23 Theoretical angular dependence of the dHvA frequency corresponding to band 25-hole Fermi surface in $LaRh_2Si_2$.

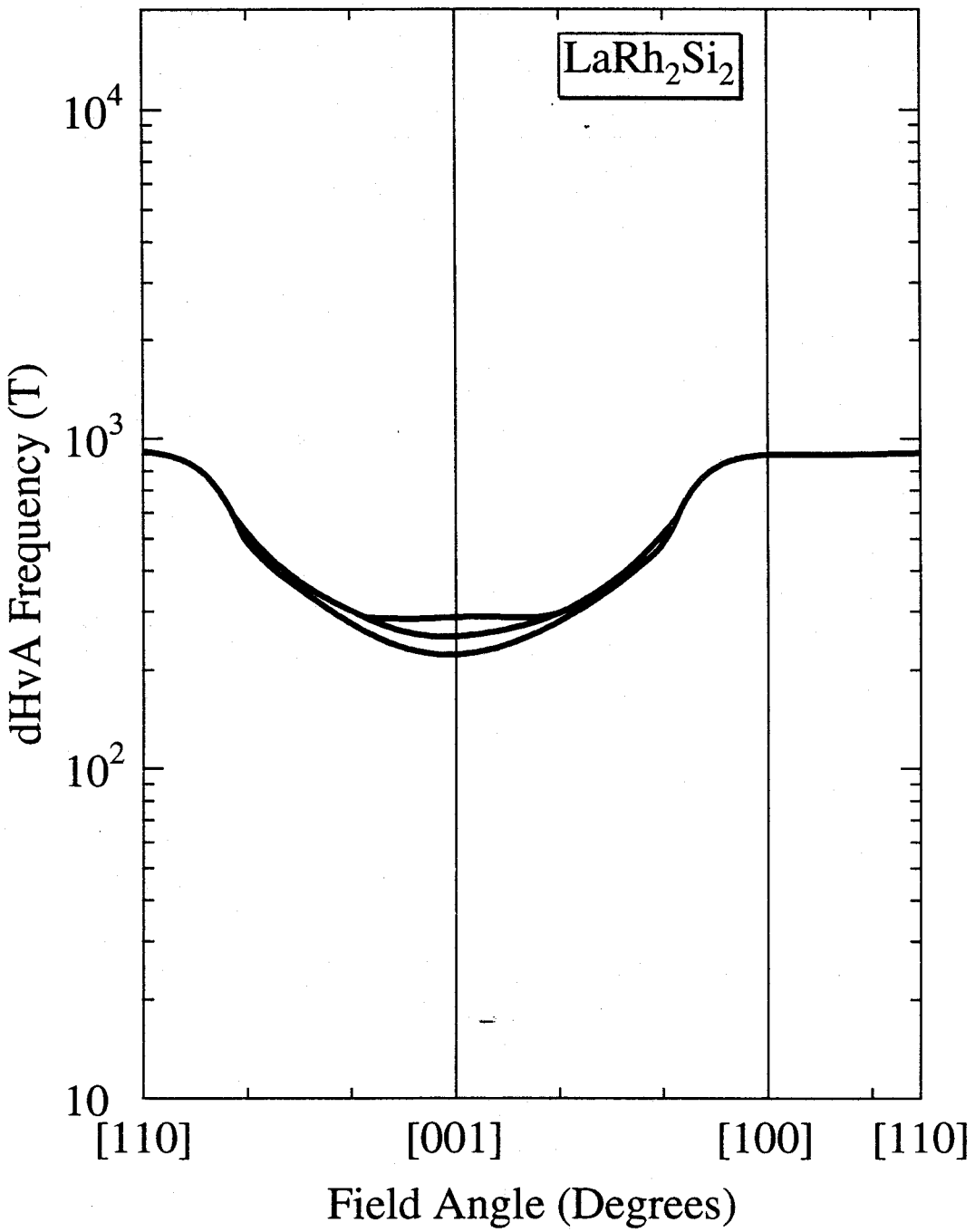

Fig. 4.24 Theoretical angular dependence of the dHvA frequency corresponding to band 26-electron Fermi surface in $LaRh_2Si_2$.

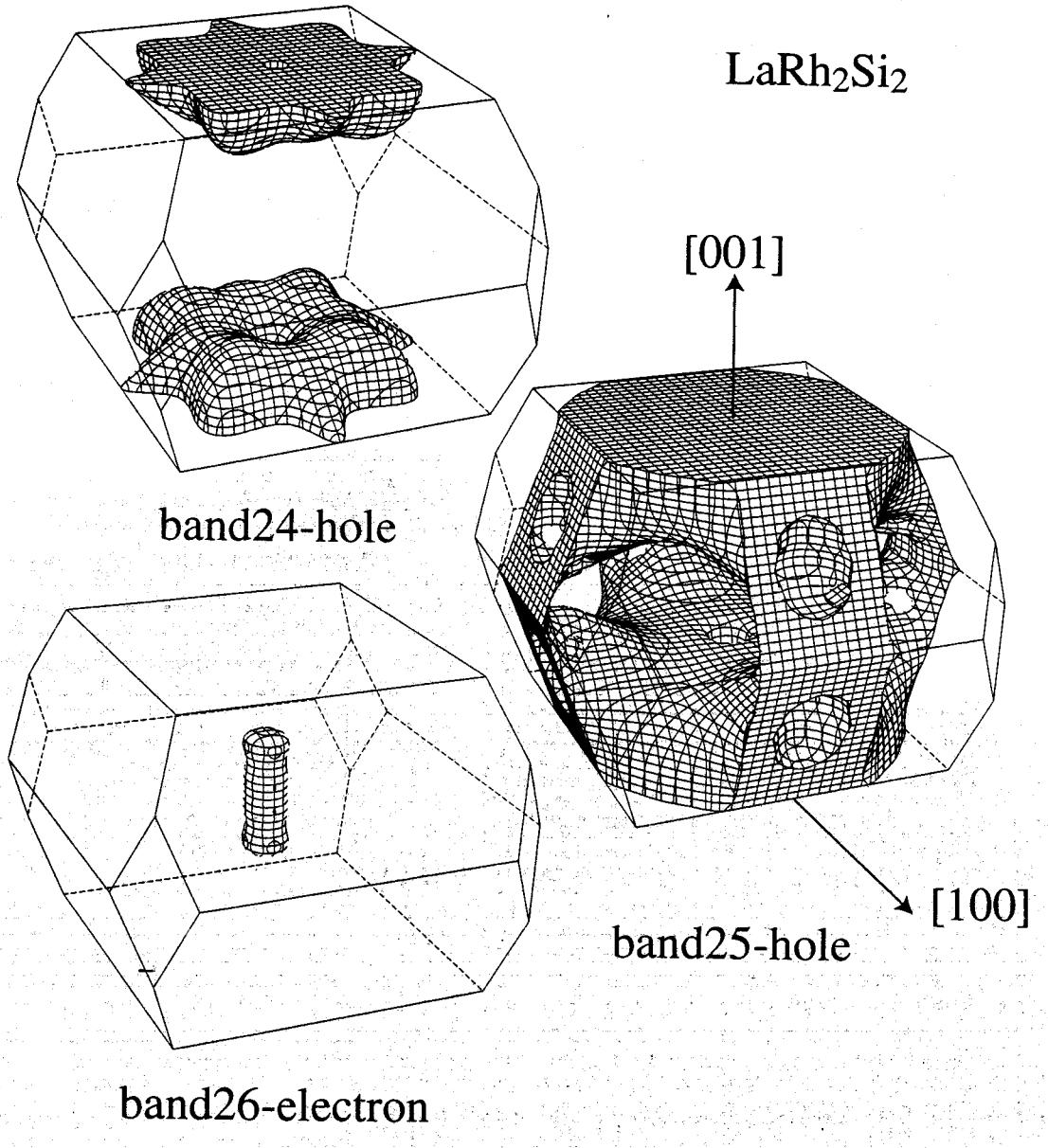

Fig. 4.25 Fermi surfaces of $LaRh_2Si_2$.

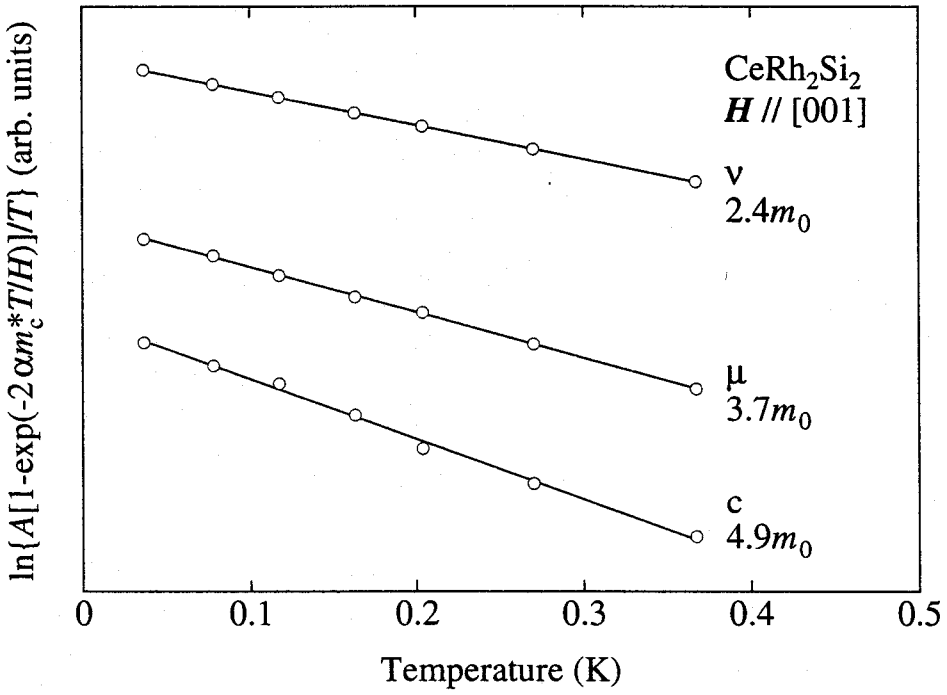

Fig. 4.26 Mass plot for $CeRh_2Si_2$.

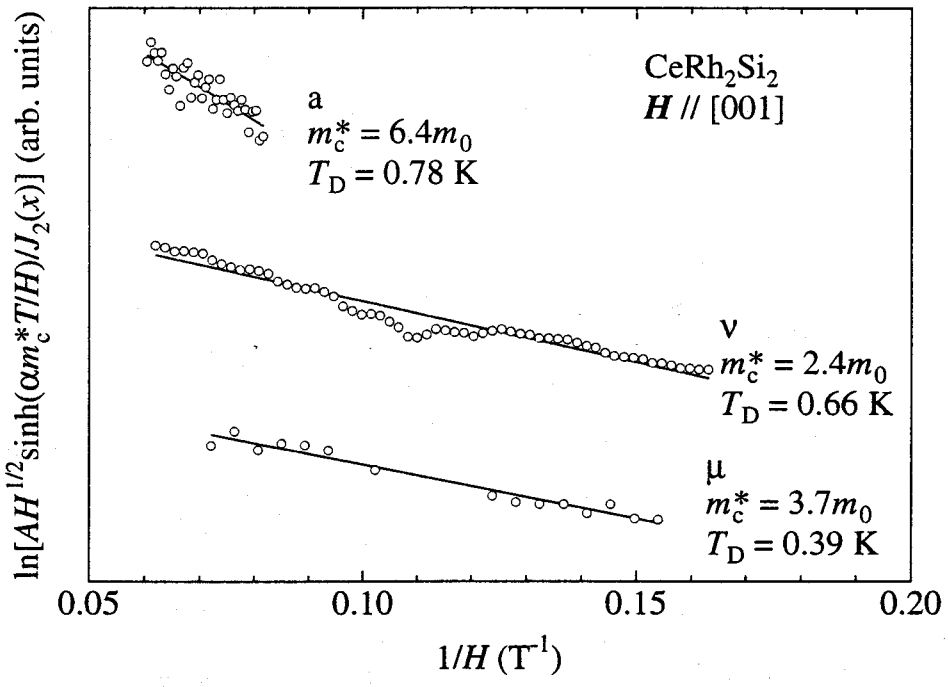

Fig. 4.27 Dingle plot for $CeRh_2Si_2$.

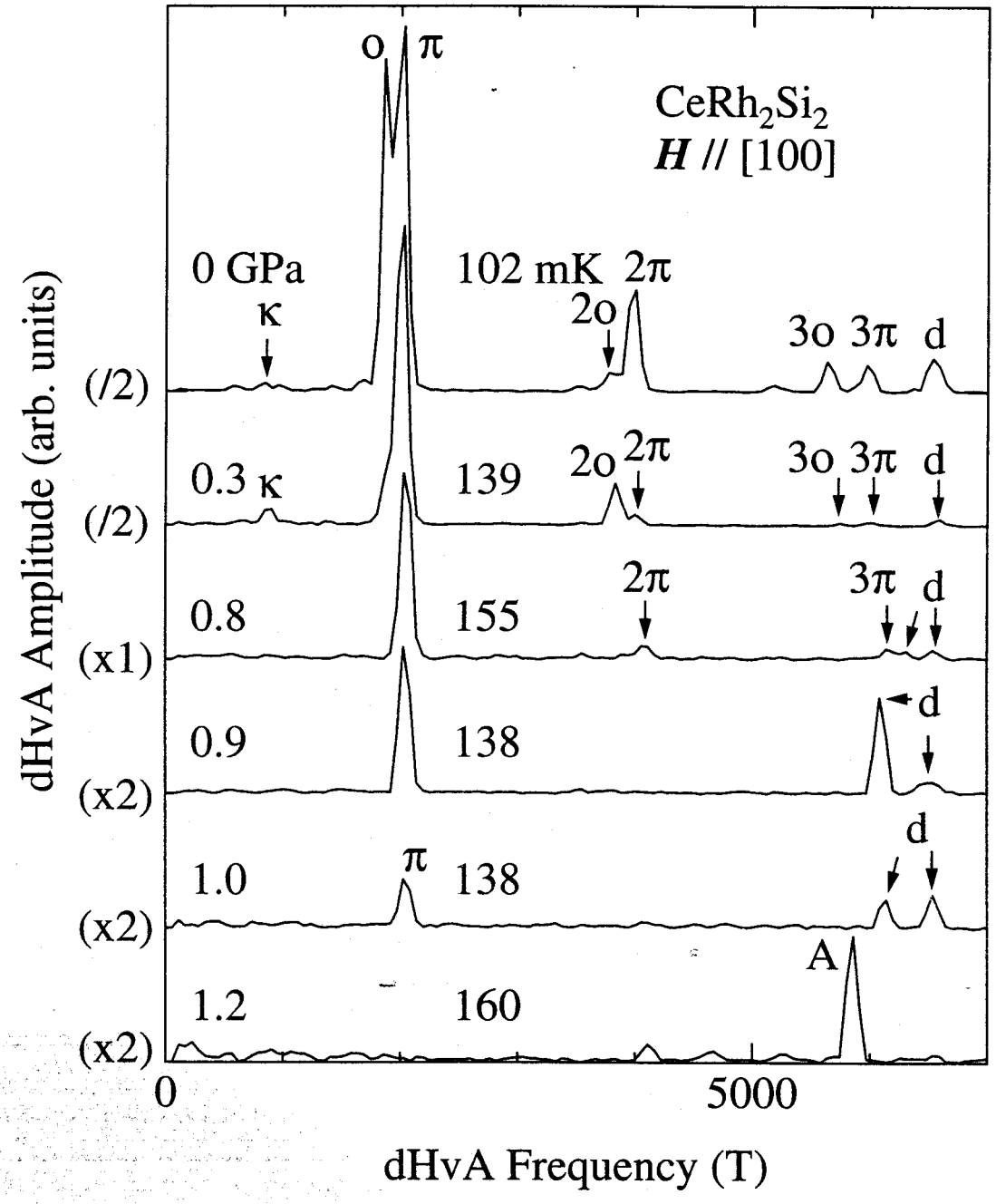

Fig. 4.28 FFT spectra under pressure in $CeRh_2Si_2$.

obvious that a new Fermi surface appears at 1.2 GPa.

Figure 4.29 shows the pressure dependence of the dHvA frequencies. The dHvA frequencies are found to be completely different above and below $p_c \simeq 1.0$–1.1 GPa. This indicates a change of the Fermi surface.

We also determined the cyclotron effective mass m_c^* from the temperature dependence of the dHvA amplitude. Figure 4.30 shows the pressure dependence of the cyclotron masses. They increase linearly with increasing pressure, although the mass of branch d increases steeply above 0.9 GPa, reaching about $18m_0$. The mass of branches A is also large: 22–$24m_0$. The mass of branch A has a maximum at p_c. Here, an error of the m_c^* value is $\pm 1.0m_0$ above 1.1 GPa, $\pm 0.5m_0$ at 1.0 GPa and less than $\pm 0.2m_0$ below 0.9 GPa. The present increase of the cyclotron mass is approximately consistent with an increase of the γ value from 23 to 80 mJ/K^2·mol as a function of pressure.[39)]

We will discuss the topology of the new Fermi surface and its cyclotron mass. We calculated the energy band structure of $CeRh_2Si_2$ in the scheme of the FLAPW method within the local density approximation. The $4f$ electrons in $CeRh_2Si_2$ are assumed to be itinerant. Above $p_c \simeq 1.0$–1.1 GPa, $CeRh_2Si_2$ indicates a non-magnetic ground state with a large γ value of about 80 mJ/K^2·mol. The $4f$-itinerant model might be applicable to the present non-magnetic heavy fermion state.

For the band structure calculation, the scalar relativistic effects were taken into account for all the electrons, and the spin-orbit interactions were also included self-consistently for all the valence electrons as in a second variational procedure. The LAPW basis functions were truncated at $|\boldsymbol{k} + \boldsymbol{G}_i| \leq 4.85 \times 2\pi/a$, corresponding to 577 LAPW functions at the Γ point. Both for the potential convergence and the final band structure, we used 369 k-points in the irreducible 1/16 th of the Brillouin zone.

The calculated Fermi surfaces are shown in Fig. 4.31. Figure 4.32 shows the corresponding angular dependence of the theoretical dHvA frequency. The theoretical dHvA frequency, the band mass and the curvature factor are listed in Table 4.IV. $CeRh_2Si_2$ is a compensated metal with equal volume of bands 26- and 27-electron Fermi surfaces and a band 25-hole Fermi surface. All the Fermi surfaces are closed. A theoretical specific heat coefficient γ_b is 18 mJ/K^2·mol, so that the ratio of the experimental γ to γ_b is $\gamma/\gamma_b = 4.5$.

Branch A, where its dHvA frequency and cyclotron mass are 5800 T and 22–$24m_0$, respectively, approximately corresponds to a maximum cross-section of the band 25-hole Fermi surface. The theoretical dHvA frequency and band mass are 4650 T and $5.3m_0$, respectively. The experimental dHvA frequency is very close to the calculated one. The cyclotron mass is 4.2–4.5 times larger than the corresponding band mass, which is consistent with the ratio $\gamma/\gamma_b = 4.5$.

When the field is directed along the [100] direction, the orbit named B in the band 25-

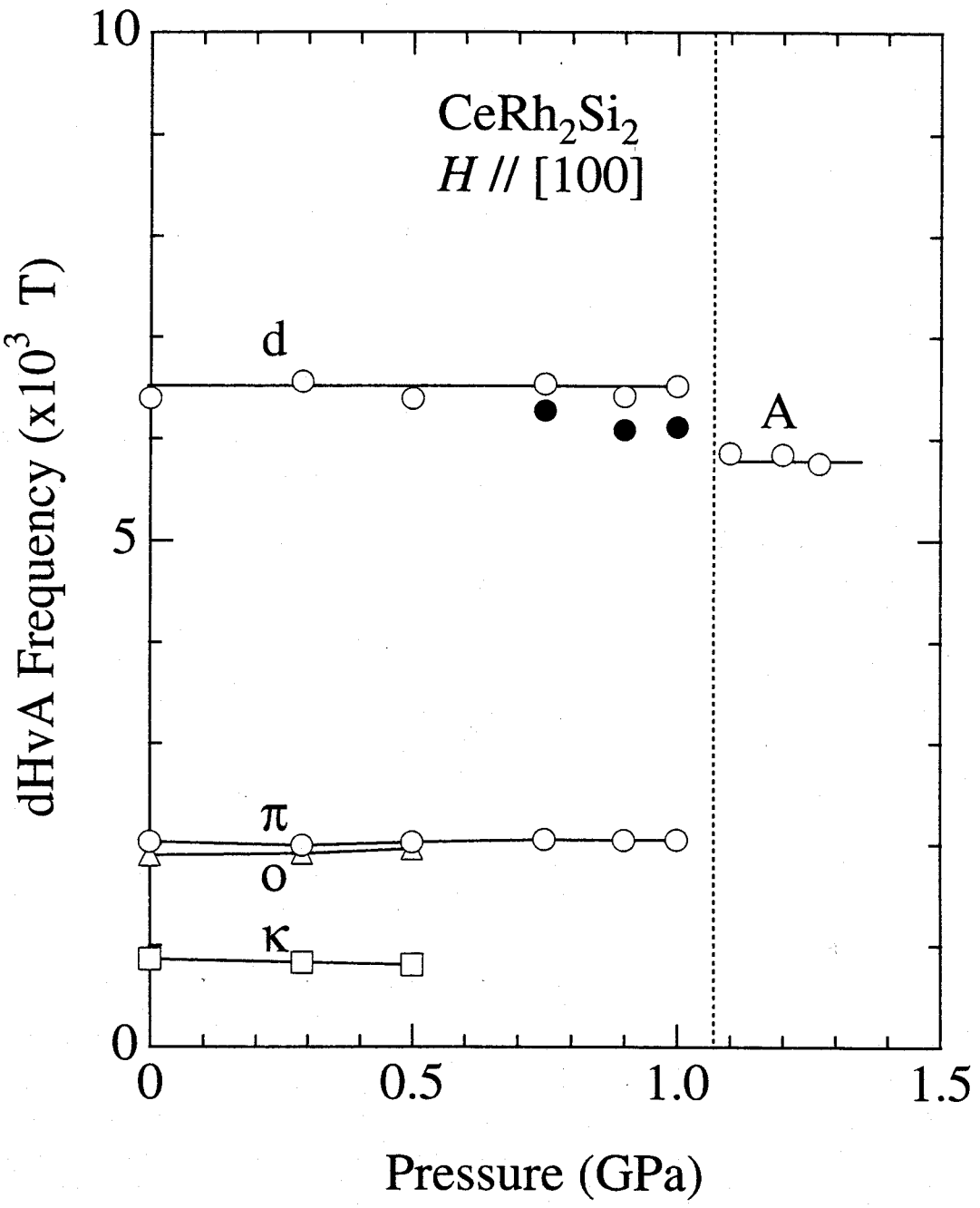

Fig. 4.29 Pressure dependence of the dHvA frequencies in $CeRh_2Si_2$.

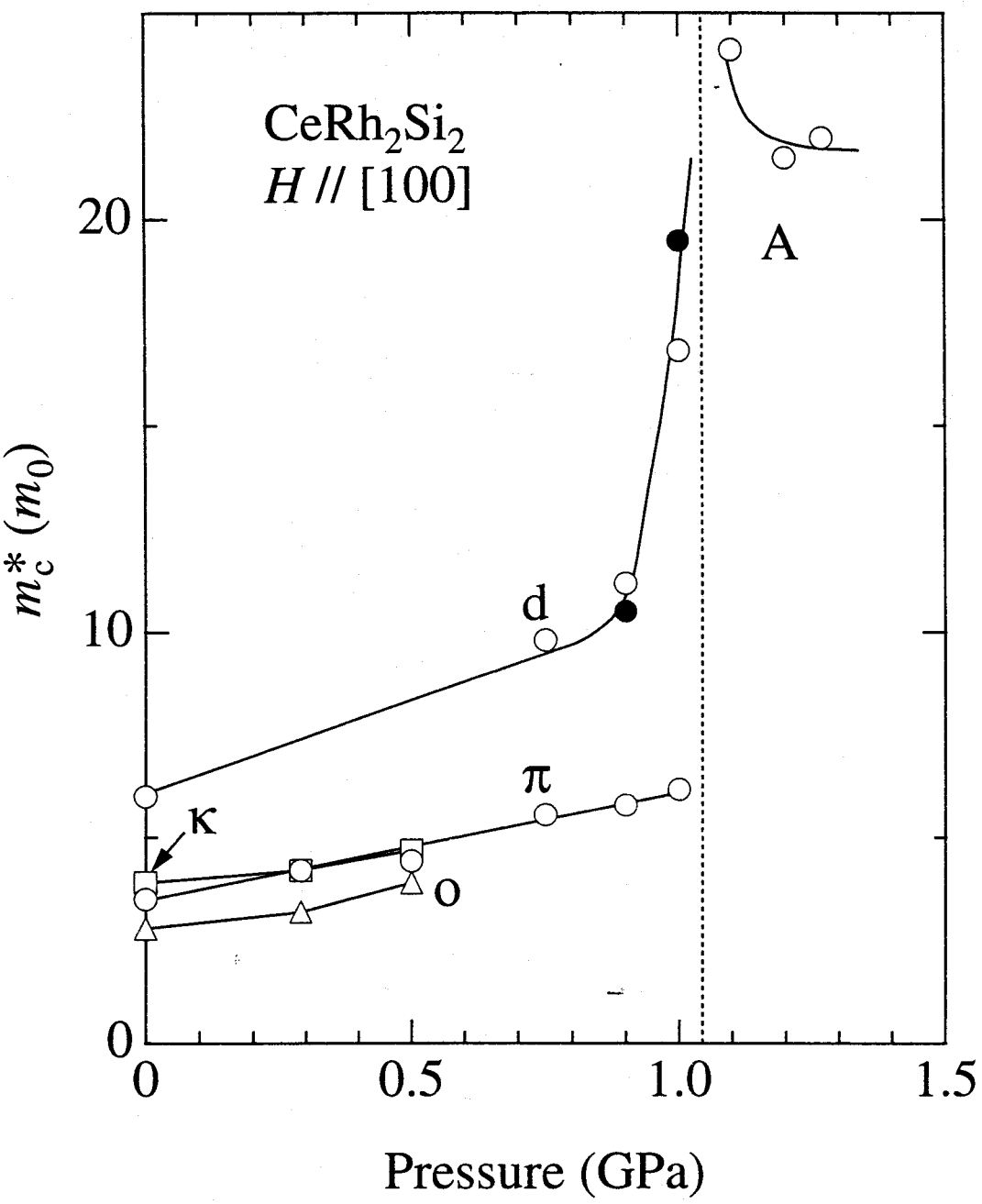

Fig. 4.30 Pressure dependence of the cyclotron masses in $CeRh_2Si_2$.

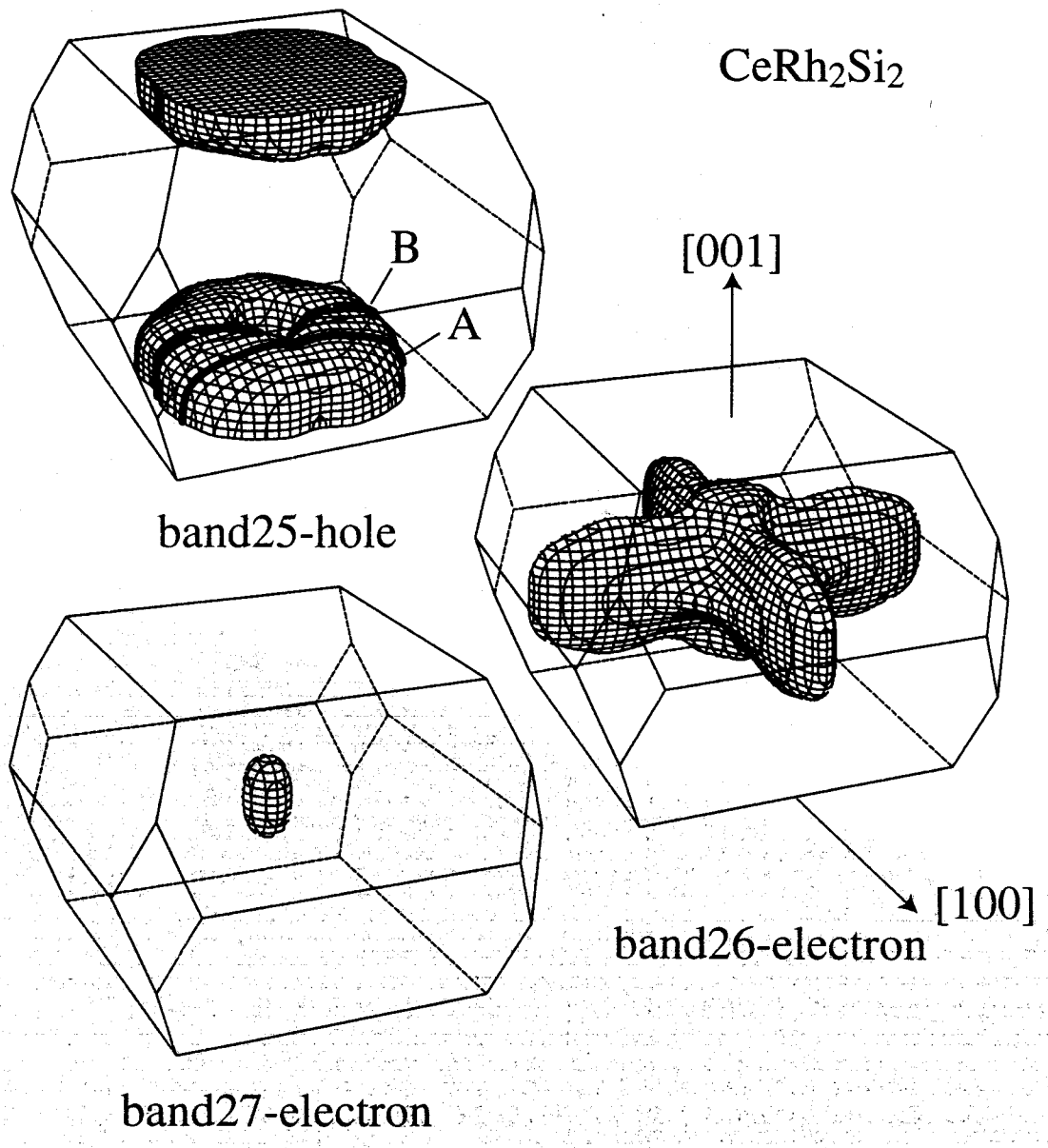

Fig. 4.31 Fermi surfaces of $CeRh_2Si_2$ based on the $4f$-itinerant band model.

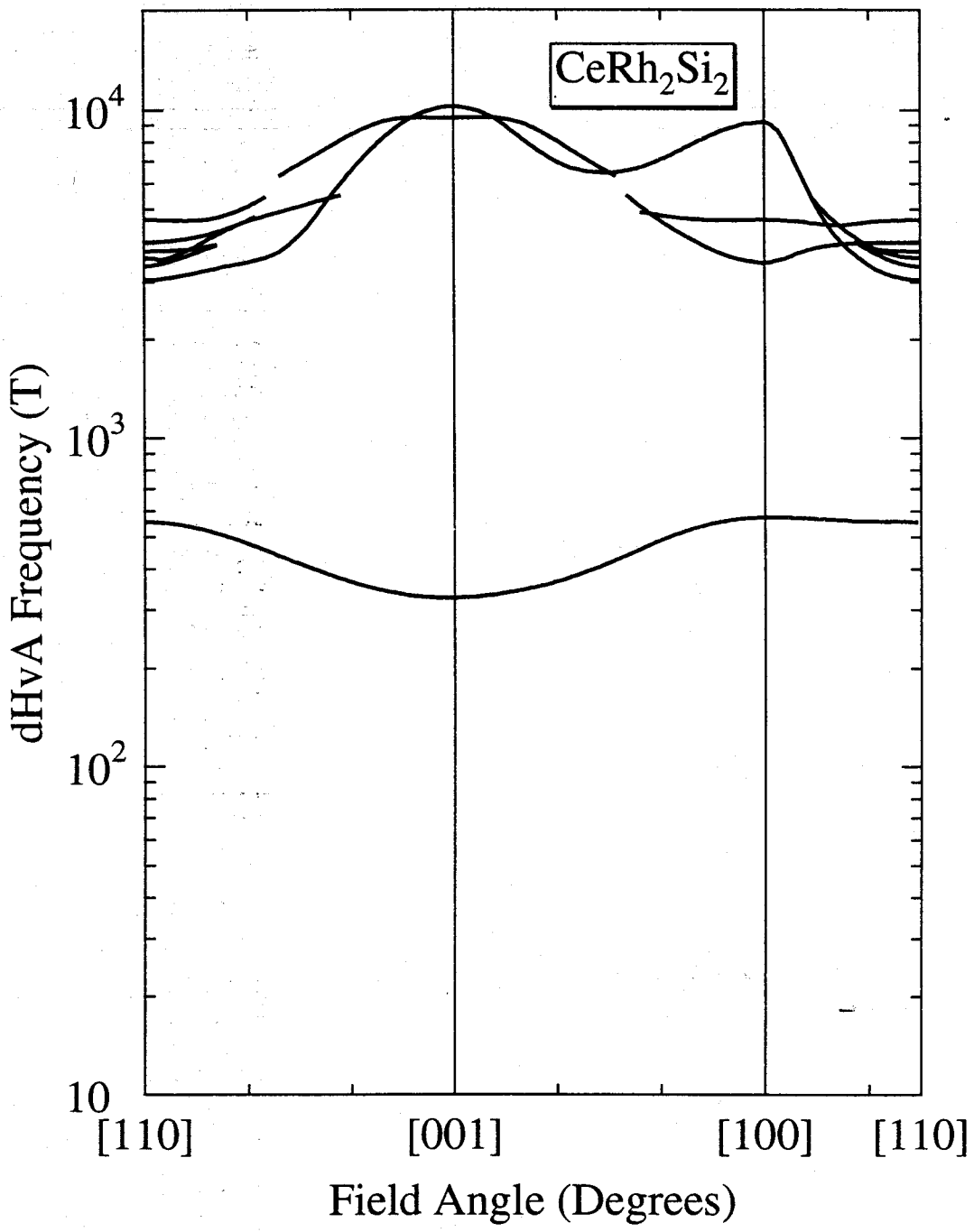

Fig. 4.32 Theoretical angular dependence of the dHvA frequency in $CeRh_2Si_2$.

Table 4.IV Theoretical dHvA frequency F, the band mass m_b and the curvature factor $\partial^2 S/\partial {k_H}^2 = S''$ in $CeRh_2Si_2$.

	$H \parallel [110]$				$H \parallel [001]$				$H \parallel [100]$			
	F (T)	m_b (m_0)	S''		F (T)	m_b (m_0)	S''		F (T)	m_b (m_0)	S''
25	4650	5.7	−2.4	26	10180	11.8	−8.0	26	9210	8.4	−12
25	3970	4.3	0.2	25	9440	5.8	−0.6	25 (A)	4650	5.3	−1.3
26	3730	6.4	−0.8					25 (B)	3430	8.0	4.1
26	3560	6.2	−2.7								
26	3360	7.9	2.0								
26	3050	4.2	0.7								
27	560	1.3	−0.6	27	330	0.65	−0.3	27	580	1.3	−2.1

hole Fermi surface and another orbit in the band 26-electron Fermi surface have minimum and maximum cross-sections, respectively. These orbits were not observed experimentally due to large curvature factors and large band masses of these Fermi surfaces. A band 27-electron Fermi surface was also not observed in the present experiment. This is most likely due to an extremely small Fermi surface. The detected branch A is thus well explained by the $4f$-itinerant band model.

Interesting is a mass enhancement mechanism in the pressure below $p_c \simeq 1.0-1.1$ GPa. The charge transfer of the $4f$ electrons to the conduction band is extremely small because the dHvA frequency is almost unchanged up to 1.0 GPa. Nevertheless, the cyclotron mass becomes large with increasing pressure. To clarify the present mass enhancement, it is useful to consider the mass enhancement in CeB_6 and $CeAl_2$ with the antiferromagnetic ordering, where their Fermi surfaces are almost the same as those of the corresponding lanthanum compounds. The ratio of the γ value is $\gamma(CeB_6)/\gamma(LaB_6)$=96 and $\gamma(CeAl_2)/\gamma(LaAl_2)$=13.[15,61] With increasing pressure, the ratio of $\gamma(CeRh_2Si_2)/\gamma(LaRh_2Si_2)$ increases from 2 at ambient pressure to 8 at 1 GPa.[39] The present $CeRh_2Si_2$ at 1 GPa is close to $CeAl_2$.

In conclusion, we discovered a drastic change of the Fermi surface and cyclotron mass under pressure for $CeRh_2Si_2$ in the dHvA experiment. These results give rise to a new aspect of the strongly correlated electron system.

4.2 CeNi

4.2.1 Electrical resistivity

Figure 4.33 shows the temperature dependence of the electrical resistivity in CeNi. The residual resistivity ρ_0 and the residual resistivity ratio ρ_{RT}/ρ_0 (=RRR) are 0.24 $\mu\Omega$·cm and 400 for the a-axis, 0.27 $\mu\Omega$·cm and 450 for the b-axis, and 0.23 $\mu\Omega$·cm and 330 for the c-axis, respectively. These values indicate the high-quality sample. The RRR values for the previous samples were 180, 180 and 160, respectively.[48)]

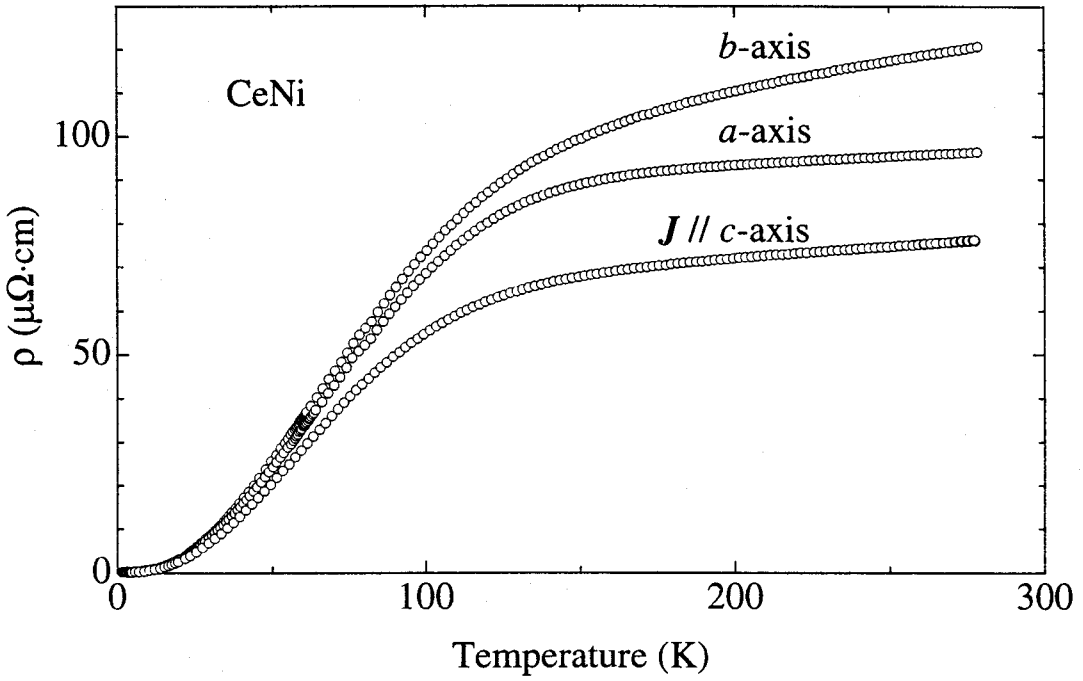

Fig. 4.33 Temperature dependence of the electrical resistivity in CeNi.

4.2.2 dHvA effect

at ambient pressure

Figures 4.34, 4.35 and 4.36 show the typical dHvA oscillations and the corresponding FFT spectra for the fields along the a-, c- and b-axes, respectively. We have observed so many dHvA branches in each field direction. For example, we have observed eleven kinds of dHvA branches in the range from 200 to 9000 T for the field along the a- and b-axes. These dHvA frequencies corresponds to small cross-sections in the Brillouin zone, which are occupied in the range from 0.84% to 35% for the field along the b-axis. On the

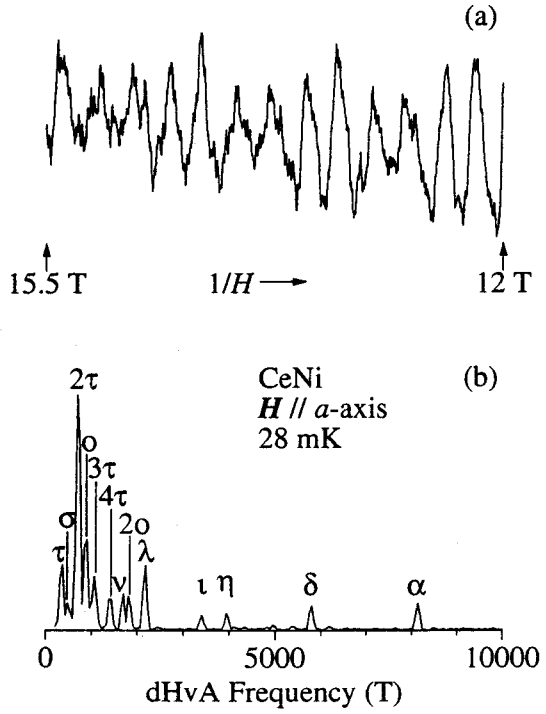

Fig. 4.34 (a) Typical dHvA oscillation and (b) the corresponding FFT spectrum for the field along the a-axis in CeNi.

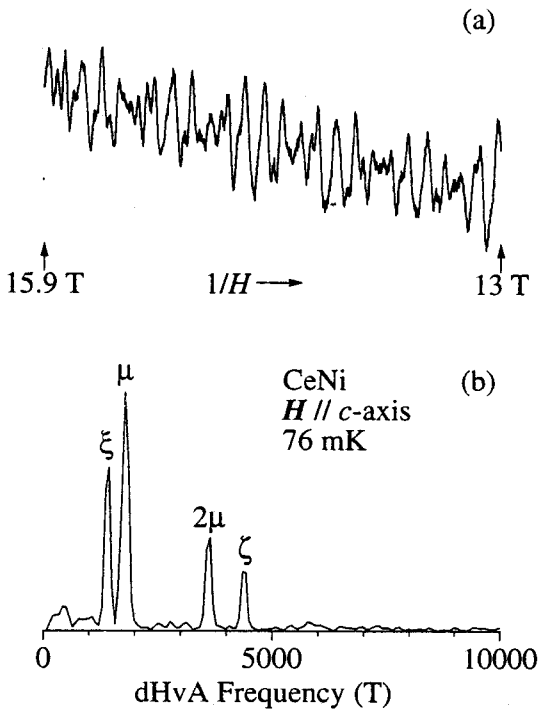

Fig. 4.35 (a) Typical dHvA oscillation and (b) the corresponding FFT spectrum for the field along the c-axis in CeNi.

other hand, only three branches are observed for the field along the c-axis, as shown in Fig. 4.35.

Figure 4.37 shows the angular dependence of the dHvA frequency. The harmonics and sums or differences of the fundamental dHvA frequencies are subtracted in Fig. 4.37. Most of the dHvA branches are observed in small angle regions, mainly centered at the symmetrical axes. These results indicate that Fermi surfaces are multiply-connected ones, most likely not existing closes Fermi surfaces.

We have also determined the cyclotron effective mass from the temperature dependence of the dHvA amplitude. Figure 4.38 shows the so-called mass plot for the field along the a-axis. A large mass of $27m_0$ is detected for branch α is five times larger than the corresponding band mass of $5.45m_0$ for an orbit a in Fig. 4.40. This mass enhancement is approximately consistent with $\gamma/\gamma_b = 3.8$ to 5.0. We list in Table 4.V the dHvA frequency and the corresponding cyclotron mass. The mass is in the range from 3.0 to $27m_0$.

The band structure and Fermi surfaces of CeNi were calculated by the all-electron relativistic LAPW (RLAPW) method with exchange and correlation potentials in a local

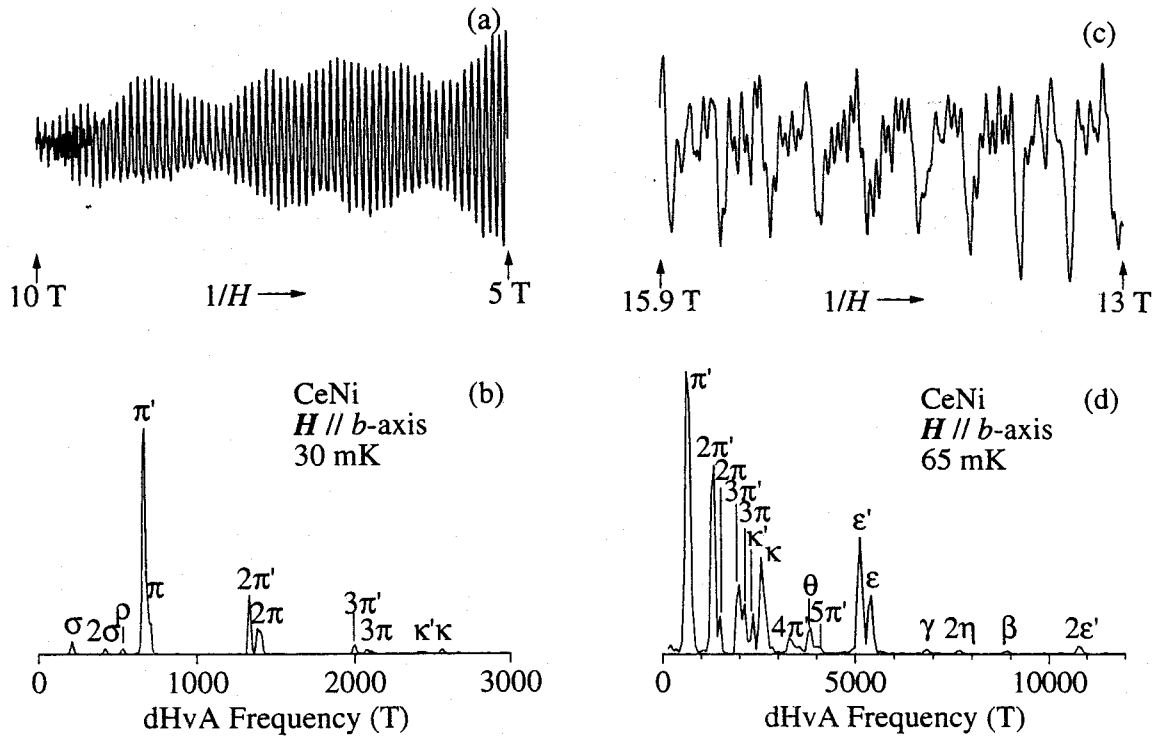

Fig. 4.36 Typical dHvA oscillation and the corresponding FFT spectrum for the field along the *b*-axis in the field ranges from 5 to 10 T, (a) and (b), and from 13 to 15.9 T, (c) and (d), in CeNi.

density approximation, which is referred as a restricted version of the spin-polarized relativistic LAPW method in the paramagnetic state. From calculations of the density of states at the Fermi level, the theoretical specific heat coefficient γ_b is estimated as 16.96 mJ/K^2·mol, so that the ratio of the experimental γ to γ_b is $\gamma/\gamma_b = 3.8$ or 5.0.

Each topology of the Fermi surface from the 19th to 22nd band is indicated by a perspective figure in Figs. 4.39(a)-(d). Figures 4.39(a) and 4.39(b) are hole sheets at the center of the (1/2, 1/2, 0) and Γ point, respectively. On the other hand, the electron sheets are shown in Figs. 4.39(c) and 4.39(d), which are plotted at the center of the (1/2, 0, 0) point. The band 19- and 20-hole sheets contain totally 0.34 holes/cell, while the band 21- and 22-electron sheets retain the compensating number of electrons.

If Figures. 4.39(b) and 4.39(c) are compared to the previous Fermi surfaces in Figs. 4 and 5 in ref. [62], we can find out some differences. In Fig. 4.39(b), there are no open orbits along the *b*-axis through the Y point, while the Fermi surface of Fig. 4.39(c) is connected with the neighbor zones along the *b*-axis. Therefore, some new dHvA branches appear in the present calculations, but no changes are given with regard to the previous

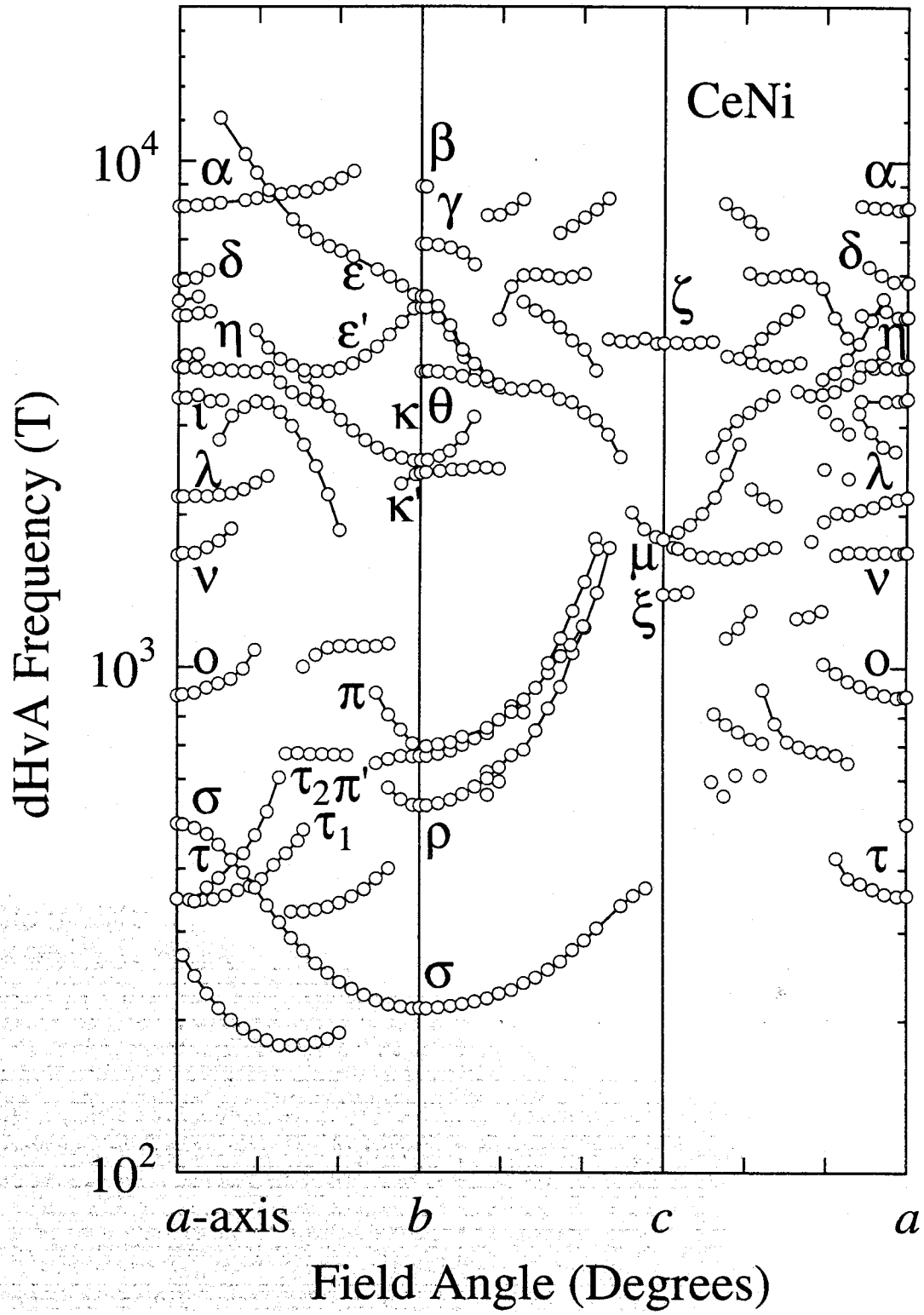

Fig. 4.37 Angular dependence of the dHvA frequency in CeNi.

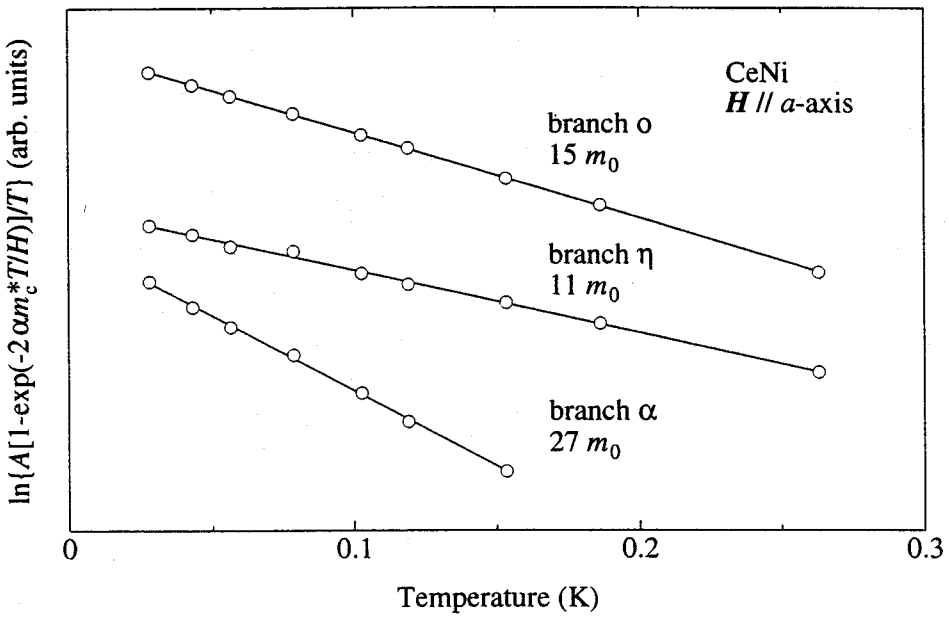

Fig. 4.38 Typical mass-plot for the field along the a-axis in CeNi.

Table 4.V Experimental dHvA frequency F and the corresponding cyclotron mass m_c^* in CeNi.

	$H \parallel a$			$H \parallel b$			$H \parallel c$	
	F (T)	m_c^* (m_0)		F (T)	m_c^* (m_0)		F (T)	m_c^* (m_0)
α	8100	27	β	8890				
δ	5770	20	γ	6840	9.5			
	5300	9.6	ε	5400	11			
	4850	13	ε'	5150	12	ζ	4380	12
η	3940	11	θ	3830	9.5			
ι	3380	17	κ	2570	8.2			
λ	2170	27	κ'	2360	10	μ	1800	16
ν	1690	5.7	π	690	4.0	ξ	1400	14
o	877	15	π'	665	4.0			
σ	483	5.4	ρ	534	3.0			
τ	355	3.7	σ	211	3.0			

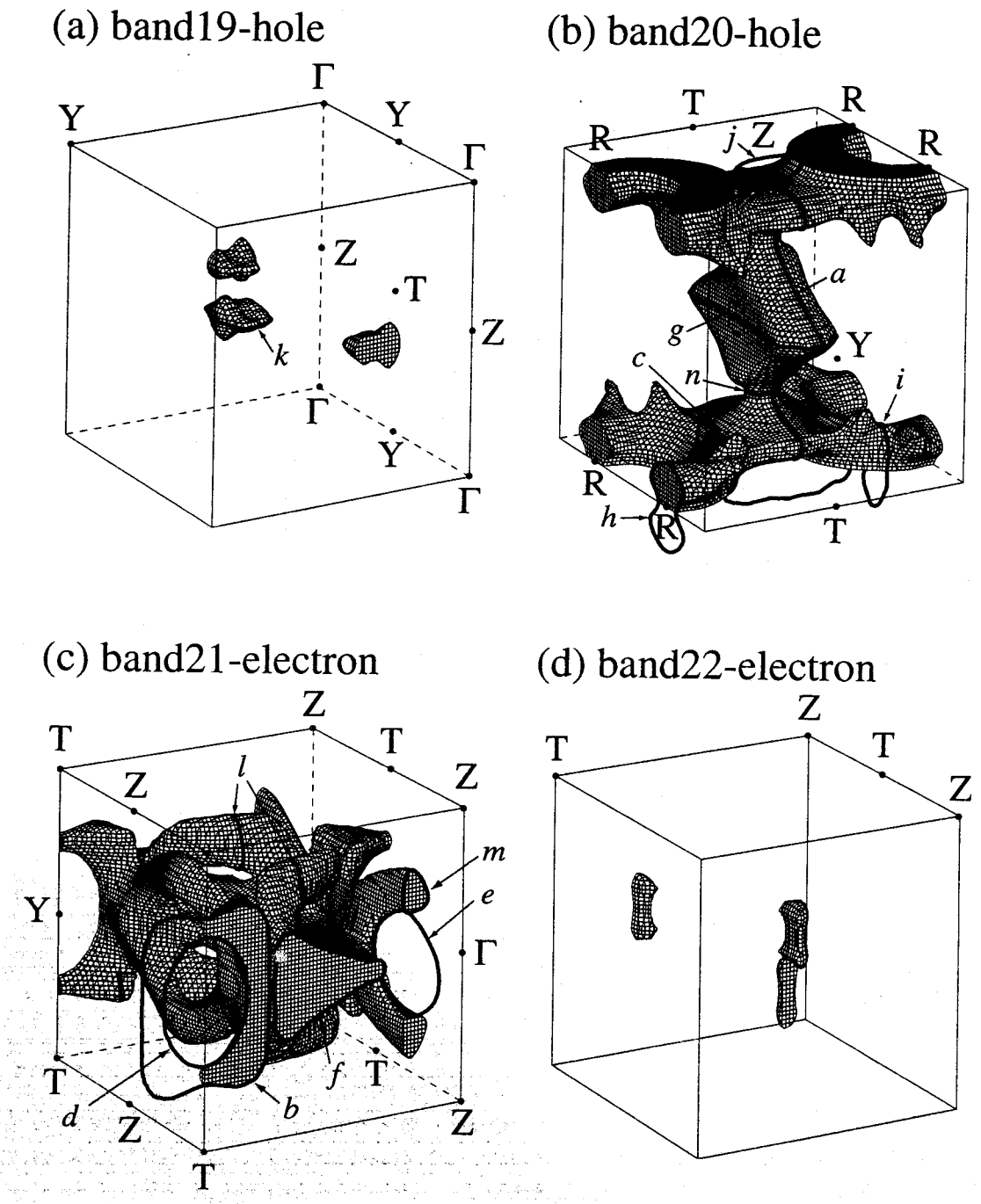

Fig. 4.39 (a) Band 19-hole, (b) band 20-hole, (c) band 21-electron and (d) band 22-electron Fermi surfaces in CeNi.

Table 4.VI Theoretical dHvA frequency F and the corresponding band mass m_b in CeNi.

	$H \parallel a$			$H \parallel b$			$H \parallel c$	
	F (T)	m_b (m_0)		F (T)	m_b (m_0)		F (T)	m_b (m_0)
a	10260	5.45	b	6990	2.37			
e	2640	3.46	d	2750	2.27			
h	910	1.59	f	2170	2.71	g	3170	3.84
			j	490	1.14			
k	330	1.64	k	440	1.33	k	800	2.65
l	310	0.76	l	870	0.97			
			m	270	0.89	n	230	1.61

findings of the transverse magnetoresistance measurements.

Finally we will compare the present dHvA data to the theoretical results of energy band calculations. Figure 4.40 shows the corresponding angular dependence of the theoretical dHvA frequency. Orbits in the Fermi surfaces named a, b, ... and n in Fig. 4.39 are shown in Fig. 4.40. The corresponding dHvA frequency and the band mass along the a-, b- and c-axes are listed in Table 4.VI. The bands 19-hole and 22-electron Fermi surfaces are closed ones, while main Fermi surfaces of bands 20-hole and 21-electron are multiply-connected ones, as mentioned above. As the cross-sectional area of the band 22-electron Fermi surface is small, the theoretical dHvA frequency is not shown in Fig. 4.40. Among the detected dHvA branches, branch σ is observed in a relatively wide angle region. The shape of the branch σ is, however, different from the shape of the theoretical orbit k in the 19-hole Fermi surface, although the magnitude of the dHvA frequency is similar to branch k.

The other theoretical branches are found around the a-, b- and c-axes. We find both similarity and difference when we compare the experimental results to the results of energy band calculations. The similarity is as follows:

1) For the field along the a-axis, branch a in Fig. 4.40 corresponds to α in Fig. 4.37. Branches e and h correspond to λ and o, respectively. Branches l_2 and l_1 correspond to τ_2 and τ_1, which are connected to l_3 and l_4, centered at the b-axis. If this speculation is right, branch τ_1 is connected to branch π'.

2) For the field along the b-axis, branches b, d, f and j correspond to branches γ, κ, κ' and ρ, respectively.

3) For the field along the c-axis, branches g and n correspond to branches ζ and μ, respectively, although the magnitude of the dHvA frequency is different between

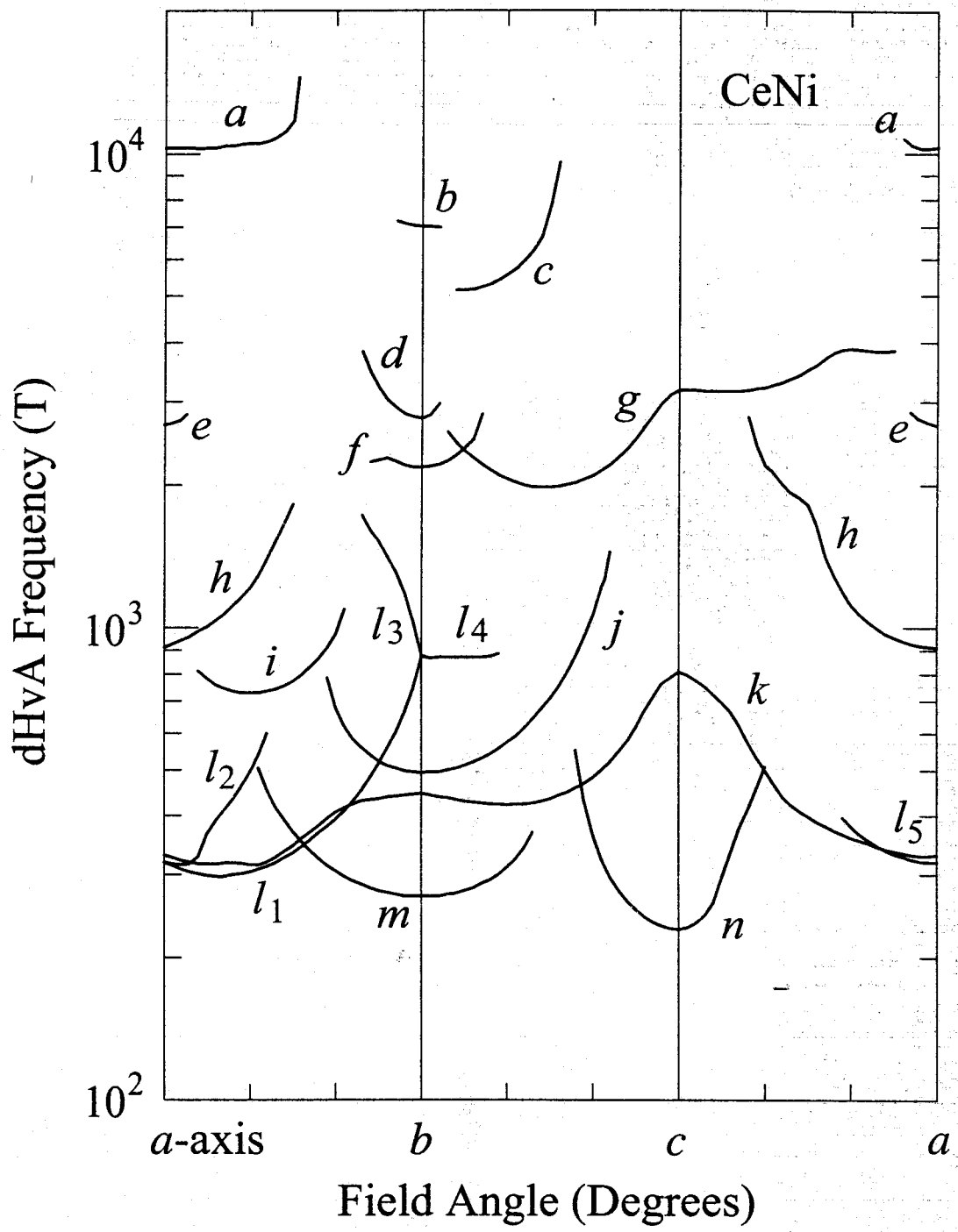

Fig. 4.40 Angular dependence of the theoretical dHvA frequency in CeNi.

them.

Most of the theoretical branches correspond to the experimental ones, although the detected branches are so many in number, compared to the theoretical ones. For example, branches ε and ε' are not found theoretically.

In the previous dHvA results of $CeSn_3$ with the cubic structure, all the data were well explained by the $4f$-itinerant band model.[27,28] If we consider low symmetry of the orthorhombic structure in CeNi, it might be concluded that the present dHvA results are approximately consistent with the $4f$-itinerant band model.

The freedom of charge transfer of the $4f$-electrons thus appears in the form of the $4f$-itinerant band, but the freedom of spin fluctuations of the same $4f$-electrons enhances the effective mass via the many body Kondo effect. The cyclotron mass of the branch α is, for example, five times larger than the corresponding band mass.

under high pressure

Figures 4.41 and 4.42 show the typical dHvA oscillation and the corresponding FFT spectrum for the field along the a- and b-axis at 0.36–0.37 GPa. In this field range, we observed two dHvA branches τ and σ for the field along the a-axis and also two branches π and ε for the field along the b-axis, while we cannot observe, any dHvA oscillation for the field along the c-axis.

We show in Figs. 4.43 and 4.45 the pressure dependence of the dHvA frequency for the field along a- and b-axes, respectively. The dHvA frequency F increases slightly with increasing pressure. This is reasonable because a smaller volume due to pressure corresponds to a larger Brillouin zone than that under ambient pressure, bringing about a larger Fermi surface. Here, the first-order transition occurs above a critical pressure $p_c =$ 0.2–0.4 GPa: 0.2–0.3 GPa for the field along a-axis and 0.3–0.4 GPa for the field along b-axis. The amplitude of dHvA oscillation was reduced significantly, when pressure was applied. This is mainly due to a first-order phase transition with a hysteresis, which brings about a crystal distortion, namely crystal defects. We carried out dHvA experiment under pressure only once for one sample to acquire a better amplitude. Therefore, discrepancy of p_c may be due to the used sample quality. The dHvA branches observed above p_c are σ and τ for the field along a-axis and ε, π and σ for the b-axis. Most of the dHvA frequency was still increases monotonously with increasing pressure without any anomaly around p_c. The dHvA frequency of σ branch for the field along a-axis was reduced discontinuity at p_c. We note that no new branches was observed.

Next we studied the pressure dependence of the corresponding cyclotron mass, as shown in Fig. 4.44 and 4.46. The mass of branch τ (a-axis) and branch π (b-axis) were

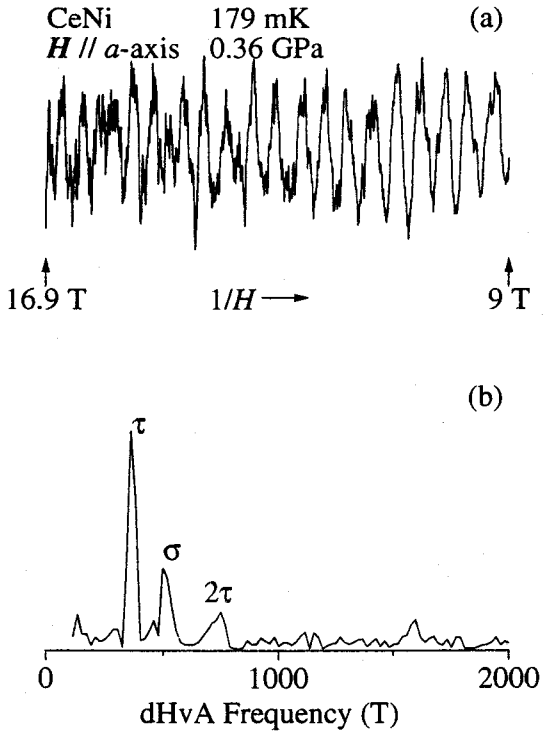

Fig. 4.41 Typical dHvA oscillation and the corresponding FFT spectrum for the field along a-axis at 0.36 GPa in CeNi.

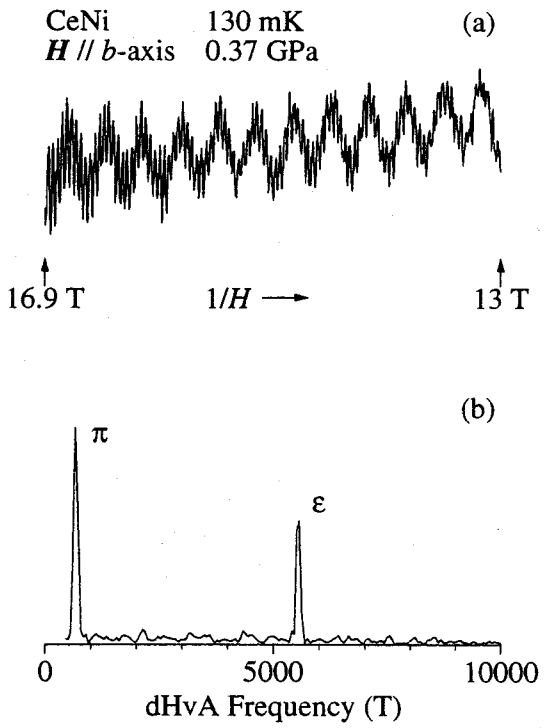

Fig. 4.42 Typical dHvA oscillation and the corresponding FFT spectrum for the field along b-axis at 0.37 GPa in CeNi.

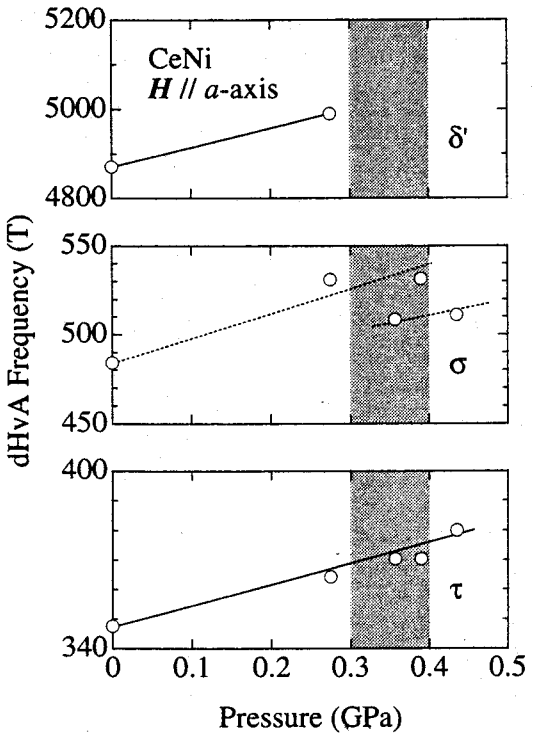

Fig. 4.43 Pressure dependence of the dHvA frequency for the field along the a-axis in CeNi.

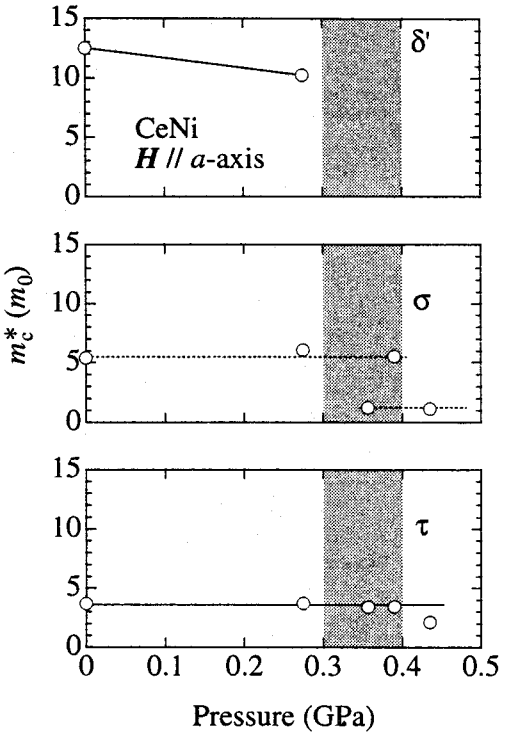

Fig. 4.44 Pressure dependence of the cyclotron mass for the field along the a-axis in CeNi.

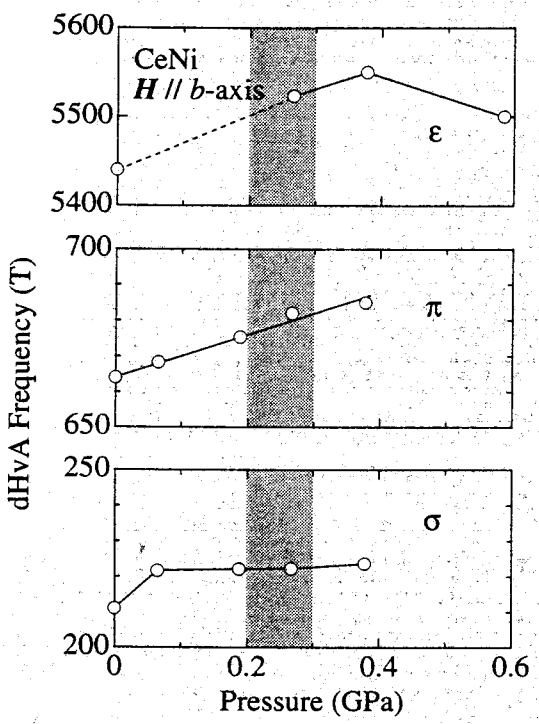

Fig. 4.45 Pressure dependence of the dHvA frequency for the field along the *b*-axis in CeNi.

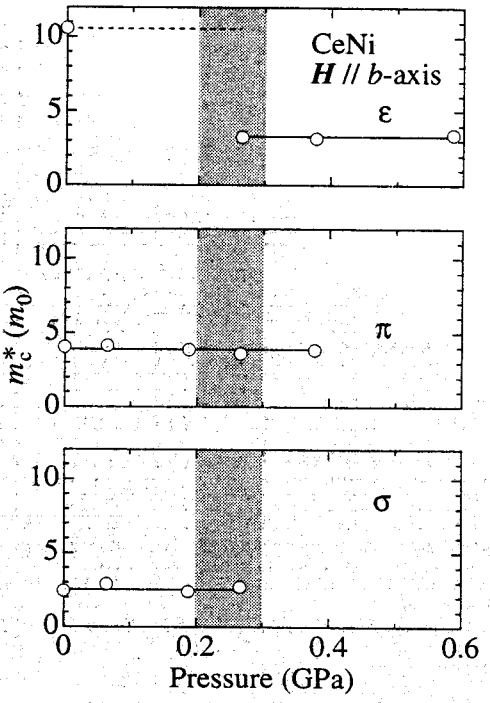

Fig. 4.46 Pressure dependence of the cyclotron mass for the field along the *b*-axis in CeNi.

Table 4.VII DHvA frequencies and the cyclotron masses at 0 GPa and at 0.37 GPa.

	$H \parallel a$-axis					$H \parallel b$-axis			
	F (T)		m_c^* (m_0)			F (T)		m_c^* (m_0)	
P (GPa)	0	0.37	0	0.36		0	0.37	0	0.37
					ε	5440	5550	11	3.2
σ	484	508	5.4	1.2	π	665	685	4.0	3.9
τ	347	380	3.7	3.4	σ	211	223	2.5	–

almost pressure independent. On the other hand, the mass of branch σ (a-axis) and branch ε (b-axis) were reduced at p_c, reflecting a change of the susceptibility mentioned in Sec. 2.3. From these results we might conclude that Fermi surfaces are unchanged in topology but a larger mass is reduced after the phase transition.

4.2.3 Specific heat

under high pressure

Figure 4.47 shows the temperature dependence of the specific heat C under constant pressure. A value of the specific heat decreases with increasing pressure. Zero pressure data, which were measured without a pressure cell, is approximately the same result reported by Gignoux *et al.*,[43] namely $\gamma = 65$ mJ/K^2·mol. In Fig. 4.48, the values of C/T are plotted as a function of T^2 below 4 K. The weak upturn behavior was observed below about 1 K. We used the specific heat data above 2 K, which are fitted by the from:

$$C/T = \gamma + \beta T^2, \tag{4.9}$$

when the β term usually comes from the contribution of the Debye phonons. The values of the Debye temperature, obtained under pressure, scatter around 125 ($\pm$10) K.

By a linear extrapolation of C/T to 0 K, we obtain the γ value, which is proportional to the density of state at Fermi level $D(E_F)$. Figure 4.49 indicates a pressure dependence of the γ value. It shows a rather flat initial slope below 0.3 GPa. Above 0.3 GPa, the γ value decreases steeply with increasing pressure. This result corresponds to the transition under pressure mentioned in Sec. 2.3. The ratio of the γ value at ambient pressure to the value at 0.5 GPa is 0.7, which is larger than the ratio of 0.4–0.5 in the susceptibility measurement.

We will discuss the present transition from a non-magnetic state with a moderately large γ value of 65 mJ/K^2·mol to another non-magnetic state with about half of the γ value under pressure of 0.5–0.7 GPa. The local moments of the $4f$ electrons play an

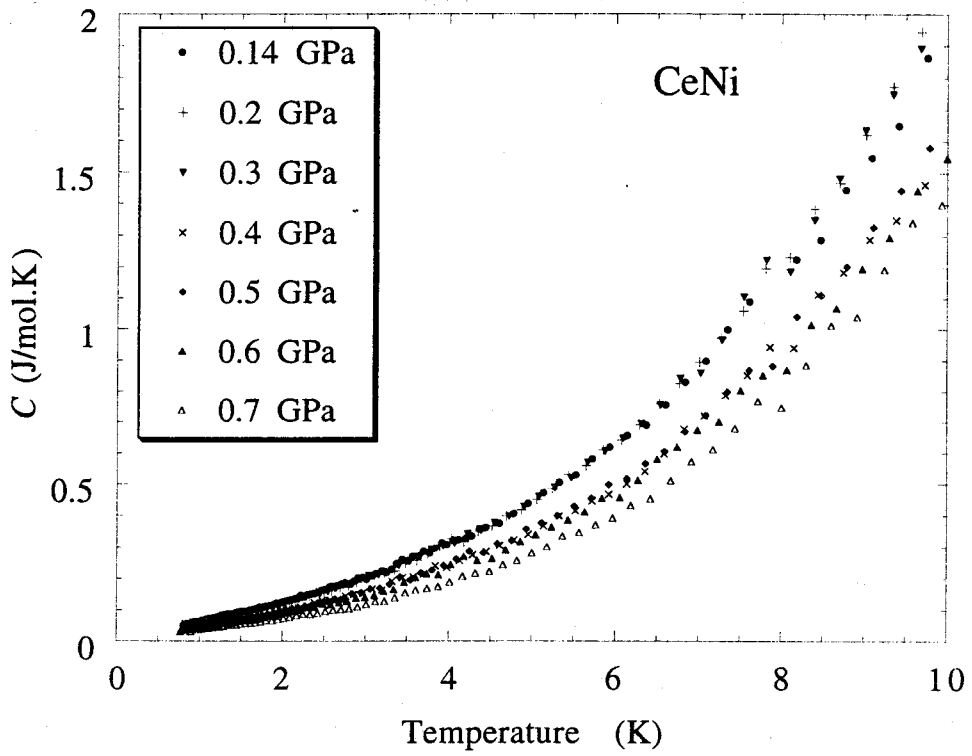

Fig. 4.47 Temperature dependence of the specific heat in CeNi as a function of the pressure.

essential role of the Kondo scattering at each Ce-site above T_K. In this temperature, the $4f$ levels in the crystalline electric field (CEF) are generally split into three doublets in non-cubic symmetry. On the other hand, below T_K the local moments are well known to form an f-derived band with a rather flat dispersion. In CeNi, the γ value is estimated roughly from the relation as expressed in eq. 2.7. The topology of the Fermi surface of CeNi is approximately consistent with $4f$-itinerant band model. Fitting is, however, not excellent compared to that of $CeSn_3$ because of the non-cubic (orthorhombic) crystal structure. The γ value is about four times larger than the theoretical value based on the $4f$-itinerant band model. This is because that the mass enhancement based on the many-body Kondo effect is not included in the conventional band calculations. We suppose that the non-magnetic state with half of the γ value under pressure of 0.5–0.7 GPa is the $4f$-itinerant electronic state with a smaller degree of correlations. Namely, the topology of the Fermi surface is unchanged but a degree of correlations is different between two electronic states. In fact from the dHvA experiment it is found that a main Fermi surface is unchanged under pressure, but the cyclotron mass is reduced after the transition. A question is why this transition is of a first-order type. A change of the electronic state

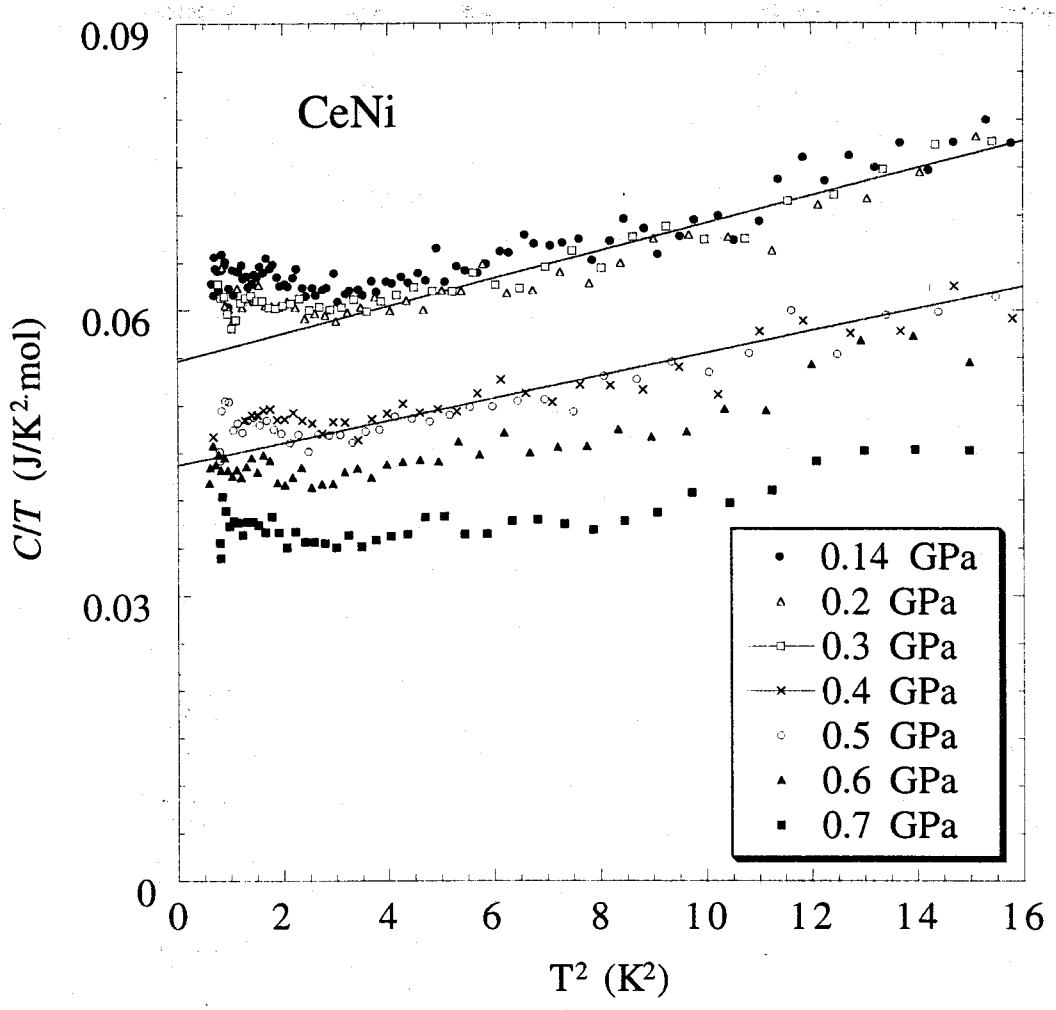

Fig. 4.48 Low temperature part of the specific heat of CeNi in the form of C/T versus T^2 as a function of pressure.

of $4f$ electrons from localized to itinerant with decreasing temperature in CeNi is not a transition but a so-called crossover effect. This remains as the question, together with a problem of the γ-α transition.

In conclusion, we have studied the pressure dependence on the specific heat in a CeNi single crystal using a clamp-type pressure-cell up to 0.8 GPa. The pressure dependence of the electronic specific heat coefficient exhibits a sharp drop between 0.3 and 0.4 GPa with increasing pressure. The results suggest that an instability of the intermediate valence state occurs at a critical pressure of 0.35 GPa at $T = 0$ K.

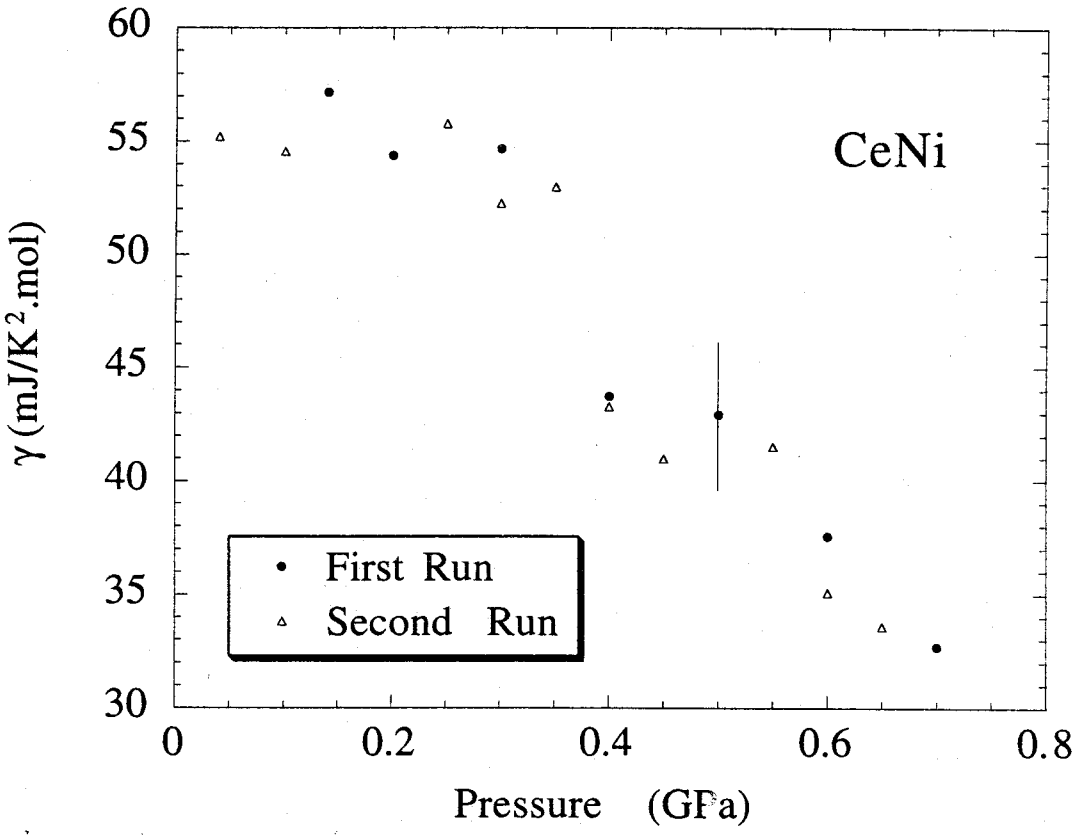

Fig. 4.49 Pressure dependencies of γ values.

5 Conclusion

In the present study we constructed a dHvA measuring system under pressure up to 1.4 GPa. We also grew high-quality single crystals of $CeRh_2Si_2$ and CeNi and studied the Fermi surface, magnetic and transport properties, mainly focusing on a change of the electronic state under pressure. The present experimental results are summarized as follows:

$CeRh_2Si_2$

1) The specific heat coefficient γ is 23 mJ/K^2·mol in $CeRh_2Si_2$ and 11 mJ/K^2·mol in $LaRh_2Si_2$. This result indicates that $CeRh_2Si_2$ is a usual $4f$-localized compound.

2) Reflecting the tetragonal crystal structure, the magnetic susceptibility and thermal expansion coefficient are highly anisotropic, which are well explained by the $4f$-CEF scheme with three doublets separated by 310 and 680 K.

3) Two antiferromagnetic transitions at $T_{N1} = 36$ K and $T_{N2} = 25$ K were observed in the specific heat and thermal expansion coefficient.

4) We observed a two-step metamagnetic transition below T_{N2} for the field along the [001] direction. The transition field is about 26 T at 4.2 K. A saturated moment of $1.55\mu_B$/Ce is consistent with the result of neutron scattering measurement. The two-step metamagnetic transition changes to a single-step one in the temperature range from T_{N2} to T_{N1}.

5) The metamagnetic transition was also observed under high pressure. At 0.95 GPa, the transition field is 37 T. This transition is not due to the phase transition but is related to crossover from the itinerant-$4f$ electron system to the localized-$4f$ electron system.

6) Some dHvA branches observed at ambient pressure are explained by the $4f$-localized electron model, namely by the result of band calculations for a non-$4f$ reference compound $LaRh_2Si_2$. The cyclotron effective mass is not large, ranging from 0.31 to $6.6m_0$.

7) We carried out the dHvA experiment under pressure. The dHvA frequency is approximately unchanged up to $p_c \simeq 1.0$–1.1 GPa. Here, p_c corresponds to the quantum critical pressure where T_N becomes zero at $p \to p_c$. This means that the topology of the Fermi surface is unchanged. On the other hand, the cyclotron mass

increases linearly with increasing pressure. Interesting is that the cyclotron mass of a main branch increases steeply above 0.9 GPa, reaching about $18m_0$.

8) All the branches, which were observed below p_c, disappear above p_c and a new branch with a large mass of 22–$24m_0$ appears. This branch corresponds to an orbit of the band 25-hole Fermi surface in the $4f$-itinerant band model. This is the first dHvA experiment showing a change of the $4f$-electronic state from localized to itinerant, namely indicating a drastic change of the Fermi surface and cyclotron mass under pressure.

9) We observed superconductivity under pressure of 1.1 GPa for the single crystal, and determined the upper critical field.

CeNi

1) We observed so many dHvA branches. The cyclotron effective mass is relatively large, ranging from 3.0 to $27m_0$. Most of the dHvA branches was explained by the $4f$-itinerant band model.

2) We confirmed the first-order phase transition from the dHvA and specific heat experiments under pressure. The dHvA frequencies are unchanged at the transition, indicating that the topology of the Fermi surface is unchanged. The cyclotron effective mass of some branches was reduced about quarter. Correspondingly, the specific heat coefficient $\gamma = 56$ mJ/K^2·mol at ambient pressure decreases steeply below 0.4 GPa, reaching 32 mJ/K^2·mol at 0.7 GPa. These results indicate an instability of the intermediate valence state with a critical pressure of 0.2–0.4 GPa.

Acknowledgments

I would like to express my appreciation to Professor Yoshichika Ōnuki for valuable advice and great encouragement throughout this work. I would like to express thanks to Professor Rikio Settai for helpful discussion and technical advice. I also would like to express thanks to Professor Kiyohiro Sugiyama and Dr. Yoshihiko Inada for stimulating suggestion and technical advice.

I am grateful to Professor Tatsuo C. Kobayashi and Dr. Takaki Muramatsu for technical advice for high-pressure technique and the measurements of the magnetic susceptibility and the electrical resistivity under high pressures.

The measurements of the thermal expansion coefficient were performed at Low Temperature Center. For this investigation, I am grateful to Dr. Tetsuya Takeuchi for technical advice for the capacitance method and the measurements.

I am grateful to Professor Hisatomo Harima and Professor Hiroshi Yamagami for helpful discussion and performing band calculations.

The measurements of the magnetization under pressure were performed at Research Center for Materials Science at Extreme Conditions. I am grateful to Dr. Terufumi Hamamoto and Professor Koichi Kindo for the measurements.

I am also grateful to Professor Shigeru Takayanagi for the measurements of the specific heat under pressure.

I also thanks to Mr. Ryoichi Koki, Dr. Yoshiyuki Yoshida, Dr. Dai Aoki, Mr. Hitoshi Ohkuni, Dr. Masato Hedo, Dr. Noriaki Kimura and other friends in Ōnuki group in Osaka University for their helpful assistance and discussion.

I acknowledge the financial support from the Japan Society for the Promotion of Science in frames of the Research Fellowships for Young Scientists.

References

[1] M. A. Ruderman and C. Kittel, Phys. Rev. **96**, 99 (1954).

[2] T. Kasuya, Prog. Theor. Phys. **16**, 45 (1956).

[3] K. Yosida, Phys. Rev. **106**, 893 (1957).

[4] J. Kondo, Prog. Theor. Phys. **32**, 37 (1964).

[5] S. Doniach, in *Valence Instabilities and Related Narrow-Band Phenomena*, edited by R. D. Parks (Plenum, New York, 1977), p. 169.

[6] N. B. Brandt and V. V. Moshchalkov, Adv. Phys. **33**, 373 (1984).

[7] K. Satoh, T. Fujita, Y. Maeno, Y. Ōnuki, and T. Komatsubara, J. Phys. Soc. Jpn. **58**, 1012 (1989).

[8] Y. Ōnuki and A. Hasegawa, in *Handbook on the Physics and Chemistry of Rare Earths*, edited by J. K. A. Gschneidner and L. Eyring (North-Holland, Amsterdam, 1995), vol. 20, p. 1.

[9] K. H. J. Buschow, H. J. van Daal, F. E. Maranzana, and P. B. van Aken, Phys. Rev. B **3**, 1662 (1971).

[10] A. Sumiyama, Y. Oda, H. Nagano, Y. Ōnuki, K. Shibutani, and T. Komatsubara, J. Phys. Soc. Jpn. **55**, 1294 (1986).

[11] K. Yamada, K. Yosida, and K. Hanzawa, Prog. Theor. Phys. **71**, 450 (1984).

[12] K. Yamada and K. Yosida, Prog. Theor. Phys. **76**, 621 (1986).

[13] H. Aoki, S. Uji, A. K. Albessard, and Y. Ōnuki, J. Phys. Soc. Jpn. **61**, 3457 (1992).

[14] H. Aoki, S. Uji, A. K. Albessard, and Y. Ōnuki, Phys. Rev. Lett. **71**, 2110 (1993).

[15] C. D. Bredl, J. Magn. Magn. Mater. **63-64**, 355 (1987).

[16] J. Etourneau, J.-P. Mercurio, R. Naslain, and P. Hagenmuller, J. Solid State Chem. **2**, 332 (1970).

[17] P. A. Lee, T. M. Rice, J. W. Serene, L. J. Sham, and J. W. Wilkins, Comments Condens. Matter Phys. **12**, 99 (1986).

[18] K. Miyake, T. Matsuura, and C. M. Varma, Solid State Commun. **71**, 1149 (1989).

[19] G. R. Stewart, Rev. Mod. Phys. **56**, 755 (1984).

[20] K. Kadowaki and S. B. Woods, Solid State Commun. **58**, 507 (1986).

[21] J. Rossat-Mignod, L. P. Regnault, J. L. Jacoud, C. Vettier, R. Lejay, J. Flouquet, E. Walker, D. Jaccard, and A. Amato, J. Magn. Magn. Mater. **76-77**, 376 (1988).

[22] A. Schröder, H. G. Schlager, and H. v. Löhneysen, J. Magn. Magn. Mater. **108**, 47 (1992).

[23] P. Haen, J. Flouquet, F. Lapierre, P. Lejay, and G. Remenyi, J. Low Temp. Phys. **67**, 391 (1987).

[24] G. G. Lonzarich, J. Magn. Magn. Mater. **76-77**, 1 (1988).

[25] Y. Ōnuki, I. Umehara, A. K. Albessard, T. Ebihara, and K. Satoh, J. Phys. Soc. Jpn. **61**, 960 (1992).

[26] H. Yamagami and A. Hasegawa, J. Phys. Soc. Jpn. **62**, 592 (1993).

[27] I. Umehara, Y. Kurosawa, N. Nagai, M. Kikuchi, K. Satoh, and Y. Ōnuki, J. Phys. Soc. Jpn. **59**, 2848 (1990).

[28] A. Hasegawa, H. Yamagami, and H. Johbettoh, J. Phys. Soc. Jpn. **59**, 2457 (1990).

[29] F. Steglich, J. Aarts, C. D. Bredl, W. Lieke, D. Meschede, and W. Franz, Phys. Rev. Lett. **43**, 1892 (1979).

[30] N. D. Mathur, F. M. Grosche, S. R. Julian, I. R. Walker, D. M. Freye, R. K. W. Haselwimmer, and G. G. Lonzarich, Nature (London) **394**, 39 (1998).

[31] D. Jaccard, K. Behnia, and J. Sierro, Phys. Lett. **A163**, 475 (1992).

[32] R. Movshovich, T. Graf, D. Mandrus, M. F. Hundley, J. D. Thompson, R. A. Fisher, N. E. Phillips, and J. L. Smith, Physica B **223-224**, 126 (1996).

[33] R. Movshovich, T. Graf, D. Mandrus, J. D. Thompson, J. L. Smith, and Z. Fisk, Phys. Rev. B **53**, 8241 (1996).

[34] H. Hegger, C. Petrovic, E. G. Moshopoulou, M. F. Hundley, J. L. Sarrao, Z. Fisk, and J. D. Thompson, Phys. Rev. Lett. **84**, 4986 (2000).

[35] S. S. Saxena, P. Agarwal, K. Ahllan, F. M. Grosche, R. K. W. Haselwimmer, M. J. Steiner, E. Pugh, I. R. Walker, S. R. Julian, P. Monthoux, G. G. Lonzarich, A. Huxley, *et al.*, Nature (London) **406**, 587 (2000).

[36] C. Godart, L. C. Gupta, and M. F. Ravet-Krill, J. Less-Common Met. **94**, 187 (1983).

[37] B. H. Grier, J. M. Lawrence, V. Murgai, and R. D. Parks, Phys. Rev. B **29**, 2664 (1984).

[38] S. Kawarazaki, M. Sato, Y. Miyako, N. Chigusa, K. Watanabe, N. Metoki, Y. Koike, and M. Nishi, Phys. Rev. B **61**, 4167 (2000).

[39] T. Graf, J. D. Thompson, M. F. Hundley, R. Movshovich, Z. Fisk, D. Mandrus, R. A. Fisher, and N. E. Phillips, Phys. Rev. Lett. **78**, 3769 (1997).

[40] A. Severing, E. Holland-Moritz, and B. Frick, Phys. Rev. B **39**, 4164 (1989).

[41] H. Abe, H. Kitazawa, H. Suzuki, G. Kido, and T. Matsumoto, Physica B **246-247**, 141 (1998).

[42] J. J. Finney and A. Rosenzweig, Acta Crystallogr. **14**, 69 (1961).

[43] D. Gignoux, F. Givord, R. Lemaire, and F. Tasset, J. Less-Common Met. **94**, 165 (1983).

[44] D. Gignoux and J. Voiron, Phys. Rev. B **32**, 4822 (1985).

[45] D. C. Koskenmaki and J. Karl A. Gschneidner, in *Handbook on the Physics and Chemistry of Rare Earths*, edited by J. K. A. Gschneidner and L. Eyring (North-Holland, Amsterdam, 1978), vol. 1, p. 337.

[46] Y. Isikawa, K. Mori, T. Mizushima, A. Fujii, H. Takeda, and K. Sato, J. Magn. Magn. Mater. **70**, 385 (1987).

[47] Y. Uwatoko, G. Oomi, and J. Sakurai, Physica B **186-188**, 560 (1993).

[48] Y. Ōnuki, Y. Kurosawa, K. Maezawa, I. Umehara, Y. Isikawa, and K. Sato, J. Phys. Soc. Jpn. **58**, 3705 (1989).

[49] A. V. Morozkin, Y. D. Seropegin, A. V. Gribanov, and J. M. Barakatova, J. Alloy. Compd. **256**, 175 (1997).

[50] Y. Ōnuki, T. Goto, and T. Kasuya, in *Materials Science and Technology*, edited by K. H. J. Buschow (VCH, Weinheim, 1992), vol. 3A, p. 545.

[51] M. Takashita, Ph.D. thesis, University of Tsukuba (1998), (in Japanese).

[52] L. D. Jennings and C. A. Swenson, Phys. Rev. **112**, 31 (1958).

[53] M. T. Hutchings, Solid State Phys. **16**, 227 (1965).

[54] H. Abe, H. Suzuki, H. Kitazawa, T. Matsumoto, and G. Kido, J. Phys. Soc. Jpn. **66**, 2525 (1997).

[55] K. Sugiyama, H. Fuke, K. Kindo, K. Shimohata, A. A. Menovsky, J. A. Mydosh, and M. Date, J. Phys. Soc. Jpn. **59**, 3331 (1990).

[56] K. Oda, K. Sugiyama, N. K. Sato, T. Komatsubara, K. Kindo, and Y. Ōnuki, J. Phys. Soc. Jpn. **68**, 3115 (1999).

[57] K. Sugiyama, M. Nakashima, H. Ohkuni, K. Kindo, Y. Haga, T. Honma, E. Yamamoto, and Y. Ōnuki, J. Phys. Soc. Jpn. **68**, 3394 (1999).

[58] T. Sakakibara, T. Tayama, K. Matsuhira, H. Mitamura, H. Amitsuka, K. Maezawa, and Y. Ōnuki, Phys. Rev. B **51**, 12030 (1995).

[59] P. Morin, J. Rouchy, and D. Schmitt, Phys. Rev. B **37**, 5401 (1988).

[60] H. Abe, H. Kitazawa, and H. Aoki, J. Phys. Soc. Jpn. **67**, 1852 (1998).

[61] C. D. Bredl, F. Steglich, and K. D. Schotte, Z. Phys. B **29**, 327 (1978).

[62] H. Yamagami and A. Hasegawa, J. Phys. Soc. Jpn. **60**, 1011 (1991).

Publication List

1) **S. Araki**, R. Settai, T. C. Kobayashi, H. Harima, and Y. Ōnuki,
Fermi Surface Instability in $CeRh_2Si_2$ Under Pressure,
(submitted).

2) S. Takayanagi, **S. Araki**, R. Settai, Y. Ōnuki, and N. Mōri,
Pressure effect on the specific heat of CeNi single crystal,
J. Phys. Soc. Jpn. (printed).

3) **S. Araki**, R. Settai, T. C. Kobayashi, and Y. Ōnuki,
High-quality single crystal growth and a change of the electronic states under pressure in $CeRh_2Si_2$,
J. Magn. Magn. Mater. (printed).

4) K. Sugiyama, A. Yamaguchi, M. Futoh, R. Settai, **S. Araki**, K. Miyake, T. Takeuchi, K. Kindo, Y. Ōnuki, and Z. Kletowski,
Magnetic properties of a dense Kondo compound $PrSn_3$,
J. Magn. Magn. Mater. (printed).

5) **S. Araki**, R. Settai, Y. Inada, and Y. Ōnuki,
De Haas-van Alphen effect in CeNi under pressure,
Physica B **281-282**, 736 (2000).

6) T. C. Kobayashi, T. Muramatsu, M. Takimoto, K. Hanazono, K. Shimizu, K. Amaya, **S. Araki**, R. Settai, and Y. Ōnuki,
Pressure-dependence of superconducting behavior in $CeRh_2Si_2$,
Physica B **281-282**, 7 (2000).

7) T. Hamamoto, K. Kindo, T. C. Kobayashi, Y. Uwatoko, **S. Araki**, R. Settai, and Y. Ōnuki,
Metamagnetic transition of $CeRh_2Si_2$ under high fields and high pressures at various temperatures,
Physica B **281-282**, 64 (2000).

8) T. Honma, Y. Inada, R. Settai, **S. Araki**, Y. Tokiwa, T. Takeuchi, H. Sugawara, H. Sato, K. Kuwahara, M. Yokoyama, H. Amitsuka, T. Sakakibara, E. Yamamoto, Y. Haga, A. Nakamura, H. Harima, H. Yamagami, and Y. Ōnuki,
Magnetic and Fermi surface properties of the ferromagnetic compound UGa_2,
J. Phys. Soc. Jpn. **69**, 2647 (2000).

9) T. Honma, E. Yamamoto, Y. Haga, R. Settai, **S. Araki**, Y. Inada, T. Takeuchi, K. Kuwahara, H. Amitsuka, T. Sakakibara, H. Sugawara, H. Sato, A. Nakamura, and Y. Ōnuki,
Magnetic, elastic, transport and Fermi surface properties of a ferromagnetic compound UGa_2,
Physica B **281-282**, 195 (2000).

10) H. Yamagami, T. Honma, E. Yamamoto, Y. Haga, **S. Araki**, D. Aoki, Y. Inada, and Y. Ōnuki,
Orbital polarization effect on electronic structure and Fermi surface in ferromagnetic UGa_2,
Physica B **281-282**, 771 (2000).

11) H. Tsujii, E. Tanaka, Y. Ode, T. Katoh, T. Mamiya, **S. Araki**, R. Settai, and Y. Ōnuki,
Magnetic order in the heavy fermion compound $CeCu_6$ at mK temperatures,
Phys. Rev. Lett. **84**, 5407 (2000).

12) H. Tsujii, E. Tanaka, T. Mamiya, **S. Araki**, R. Settai, and Y. Ōnuki,
AC susceptibility measurements on heavy fermion compounds $CeCu_6$ and CeNi down to submilikelvin temperatures,
Physica B **284-288**, 1265 (2000).

13) R. Settai, K. Sugiyama, A. Yamaguchi, **S. Araki**, K. Miyake, T. Takeuchi, K. Kindo, Y. Ōnuki, and Z. Kletowski,
Magnetic and electrical properties in a dense Kondo compound $PrSn_3$,
J. Phys. Soc. Jpn. **69**, 3983 (2000).

14) A. Yamaguchi, **S. Araki**, K. Miyake, K. Sugiyama, R. Settai, Y. Ōnuki, and Z. Kletowski,
Heavy electron mass and the Kondo effect in $PrSn_3$,
Physica B **281-282**, 126 (2000).

15) **S. Araki**, R. Settai, Y. Inada, Y. Ōnuki, and H. Yamagami,
de Haas-van Alphen effect and RLAPW-energy band calculations in CeNi,
J. Phys. Soc. Jpn. **68**, 3334 (1999).

16) T. Muramatsu, S. Eda, T. C. Kobayashi, M. I. Eremets, K. Amaya, **S. Araki**, R. Settai, and Y. Ōnuki,

Magnetic and transport properties of $CeRh_2Si_2$ under high pressures,
Physica B **259-261**, 61 (1999).

17) R. Settai, K. Sugiyama, **S. Araki**, Y. Yoshida, P. Ahmet, M. Abliz, K Kindo, and Y. Ōnuki,
Field-Induced ferroquadrupoler ordering in RCu_2,
in *Physics of Strongly Correlated Electron Systems*, edited by T. Komatsubara, H. Fujii, Y. Ōnuki, and H. Shiba (JJAP, Tokyo, 1999), JJAP Series 11, p. 194.

18) Y. Haga, E. Yamamoto, T. Honma, A. Nakamura, M. Hedo, **S. Araki**, H. Ohkuni, and Y. Ōnuki,
Anisotropic magnetoresistance in UBe_{13},
Physica B **259-261**, 627 (1999).

19) **S. Araki**, A. Misawa, R. Settai, T. Takeuchi, and Y. Ōnuki,
Thermal expansion and de Haas-van Alphen effect of $CeRh_2Si_2$,
J. Phys. Soc. Jpn. **67**, 2915 (1998).

20) T. Hamamoto, K. Kindo, T. Muramatsu, T. C. Kobayashi, Y. Uwatoko, **S. Araki**, R. Settai,and Y. Ōnuki,
Magnetization measurements in pulsed magnetic fields up to 50 T with a Be-Cu pressure cell,
in *Proceedings of the Physical Phenomena at High Magnetic Fields-III*, edited by Z. Fisk, L. Gor'kov, and R. Schrieffer (World Scientific, Singapore, 1998), p. 549.

21) R. Settai, **S. Araki**, P. Ahmet, M. Abliz, K. Sugiyama, Y. Ōnuki, T. Goto, H. Mitamura, T. Goto, and S. Takayanagi,
Anisotropic cooperative Jahn-Teller effect and metamagnetism in $PrCu_2$,
J. Phys. Soc. Jpn. **67**, 636 (1998).

22) R. Settai, **S. Araki**, P. Ahmet, M. Abliz, K. Sugiyama, and Y. Ōnuki,
Anisotropic ferroquadrupoler phase in magnetic fields for $PrCu_2$,
J. Magn. Magn. Mater. **177-181**, 357 (1998).

23) K. Sugiyama, M. Nakashima, A. Koyanagi, **S. Araki**, K. Kindo, T. Hata, R. Settai, and Y. Ōnuki,
High-field magnetization of $PrCu_6$ and $PrNi_5$ with the singlet ground state,
J. Phys. Soc. Jpn. **67**, 2553 (1998).

24) R. Settai, A. Misawa, **S. Araki**, M. Kosaki, K. Sugiyama, T. Takeuchi, K. Kindo, Y. Haga, E. Yamamoto, and Y. Ōnuki,
Single crystal growth and magnetic properties of $CeRh_2Si_2$,
J. Phys. Soc. Jpn. **66**, 2260 (1997).

25) R. Settai, P. Ahmet, **S. Araki**, M. Abliz, K. Sugiyama, and Y. Ōnuki,
Metamagnetism in $PrCu_2$ based on the quadrupole moment,
Physica B **230-232**, 766 (1997).